NASA CONTRACTOR REPORT

NASA CR-1769
C.1

NASA CR-

ANALYTICAL INVESTIGATION OF THE EFFECTS OF BLADE FLEXIBILITY, UNSTEADY AERODYNAMICS, AND VARIABLE INFLOW ON HELICOPTER ROTOR STALL CHARACTERISTICS

by E. D. Bellinger

Prepared by
UNITED AIRCRAFT CORPORATION
UNITED AIRCRAFT RESEARCH LABORATORIES
East Hartford, Conn. 06108
for Langley Research Center

NATIONAL AERONAUTICS AND SPACE ADMINISTRATION • WASHINGTON, D. C. • SEPTEMBER 1971

1. Report No. NASA CR-1769	2. Government Accession No.	3. Recipient's Catalog No.
4. Title and Subtitle ANALYTICAL INVESTIGATION OF THE EFFECTS OF BLADE FLEXIBILITY, UNSTEADY AERODYNAMICS, AND VARIABLE INFLOW ON HELICOPTER ROTOR STALL CHARACTERISTICS		5. Report Date September 1971
		6. Performing Organization Code
7. Author(s) E. D. Bellinger		8. Performing Organization Report No.
		10. Work Unit No.
9. Performing Organization Name and Address ·United Aircraft Corporation United Aircraft Research Laboratories East Hartford, Connecticut 06108		11. Contract or Grant No. NAS1-8350
		13. Type of Report and Period Covered Contractor Report
12. Sponsoring Agency Name and Address National Aeronautics and Space Administration Washington, D.C. 20546		
		14. Sponsoring Agency Code

15. Supplementary Notes

16. Abstract

An analytical study was conducted to investigate systematically the relative importance of blade flexibility, unsteady aerodynamics, and variable inflow (with and without wake distortions) in determining predicted helicopter rotor stall characteristics. The theoretical results of this study were compared with a corresponding full scale wind tunnel results for the H-34 rotor system. The classical theory (rigid blades, steady aerodynamics, and constant inflow) produced good correlation at nominally unstalled operating conditions. However, rotor lifts significantly lower than the test values were predicted at high blade angles of attack. The use of unsteady airfoil data provided the most significant improvement in correlation by allowing higher section lift coefficients to be reached due to the "stall delay" phenomenon associated with unsteady operating conditions. The primary effect of blade flexibility was due to blade torsional deflections, which, as with blade pitch changes, had a direct effect on performance. Variable inflow, although producing significant changes in the angle-of-attack distribution over the disc, did not appreciably affect rotor performance.

17. Key Words (Suggested by Author(s)) Helicopter rotor performance Rotor stall Rotor unsteady aerodynamics Rotor variable inflow	18. Distribution Statement Unclassified - Unlimited		
19. Security Classif. (of this report) Unclassified	20. Security Classif. (of this page) Unclassified	21. No. of Pages 114	22. Price* $3.00

*For sale by the National Technical Information Service, Springfield, Virginia 22151

ANALYTICAL INVESTIGATION OF THE EFFECTS OF
BLADE FLEXIBILITY, UNSTEADY AERODYNAMICS, AND VARIABLE INFLOW
ON HELICOPTER ROTOR STALL CHARACTERISTICS

E. D. Bellinger

United Aircraft Corporation Research Laboratories

SUMMARY

An analytical study was conducted to investigate systematically the relative importance of blade flexibility, unsteady aerodynamics, and variable inflow (with and without wake distortions) in determining predicted helicopter rotor stall characteristics. The theoretical results of this study were compared with corresponding full scale wind tunnel results for the H-34 rotor system. Various levels of rotor stall were investigated at forward speeds of 117 knots and 194 knots. The classical theory (rigid blades, steady aerodynamics, and constant inflow) produced good correlation at nominally unstalled operating conditions. However, rotor lifts significantly lower than the test values were predicted at high blade angles of attack. The use of unsteady airfoil data provided the most significant improvement in correlation by allowing higher section lift coefficients to be reached due to the "stall delay" phenomenon associated with unsteady operating conditions.

The primary effect of blade flexibility was due to blade torsional deflections, which, as with blade pitch changes, had a direct effect on performance. It was found that the deflections, and therefore performance, were sensitive to the chordwise location of the mass axis, indicating the need for accurately defining this parameter. Variable inflow, although producing significant changes in the angle of attack distribution over the disc, did not appreciably affect rotor performance.

INTRODUCTION

Until recently, the prediction of helicopter rotor performance characteristics had generally employed methods which assume rigid blades, two-dimensional steady airfoil aerodynamics, and constant inflow (Ref. 1). Under moderate flight conditions these methods have demonstrated their reliability and ease of application; however, under conditions where rotor blade section angles of attack are predicted to exceed steady-state values, the theories

have invariably predicted conservative stall characteristics (i.e., the pre-
dicted lift and propulsive force for a given power are significantly less
than measured values). This phenomenon has been observed by many investigators
(see, for example, Refs. 2 through 6) and is illustrated in Fig. 1 where
predicted lift and torque are compared with those obtained in full-scale wind
tunnel tests (Ref. 7). The fall-off in theoretical lift is characteristic of
fixed wing stall, where the lift departs from linearity and is accompanied by
a sharp increase in drag or, in this case, torque. The experimental lift data
appear unstalled and while the torque does exhibit some evidence of stall, the
stall appears to be less severe than predicted. It is these discrepancies
between test and theory that have prompted the investigation reported herein.
The purpose of the study was to examine systematically certain assumptions in
the classical theories to determine their effects on the observed discrepancies.
The assumptions that were considered most serious and which could be evaluated
with our current analyses were nonflexible blades, steady aerodynamics, and
constant inflow.

It is recognized that even the most sophisticated version of the analysis
employed in this study still contains assumptions which may eventually prove
critical to the prediction of rotor stall characteristics. For example, span-
wise flow effects due to centrifugal forces, spanwise pressure gradients, or
blade sweep have been neglected. In addition, the blades are represented by
lifting lines rather than by lifting surfaces. Work in these areas is pro-
ceeding (see, for example, Refs. 8 through 11) but is generally only in its
initial development stage. In contrast, significant progress has been made
recently in the development of variable inflow (including wake distortions)
and flexible blade analytical techniques (e.g., Refs. 12 through 15). Also,
considerable data on the unsteady aerodynamic characteristics of airfoils
oscillating sinusoidally into stall have been acquired (Refs. 16 and 17),
although there remain significant questions on how best to apply such data in
a rotor blade environment. In view of the progress made in the latter areas,
it appeared timely to conduct a systematic study to evaluate the relative
importance of these analytical refinements and to provide guidance for future
research efforts.

2

a   lift-curve slope

A   angular velocity parameter $\frac{c\dot{\alpha}}{2U}$

$\bar{A},\bar{B},\bar{C},\bar{D}$ scaling dimensions as defined in Fig. 7

a_{1_h} longitudinal flapping coefficient for the $-\cos\psi$ term in Fourier series expansion of blade flap angle with respect to the rotor shaft at the flapping hinge, deg

A_{1_s} longitudinal cyclic pitch coefficient for the $-\cos\psi$ term in Fourier series expansion of the rotor blade cyclic pitch, deg

A'_{1_s} experimental longitudinal cyclic pitch required to trim to zero first harmonic of flapping given in Ref. 7, deg

ΔA_{1_s} experimental longitudinal cyclic pitch required to trim to zero first harmonic of flapping for zero collective pitch, twist and shaft angle given in Ref. 7, deg

A',B',D' scaling dimensions as defined in Fig. 6

A'',B'',D'' scaling dimensions as defined in Fig. 6

b   number of blades

B   angular acceleration parameter $\left(\frac{c}{2U}\right)^2\ddot{\alpha}$

b_{1_h} lateral flapping coefficient, coefficient of $-\sin\psi$ term in Fourier series expansion of blade flap angle with respect to the shaft at the flapping hinge, deg

B_{1_s} longitudinal cyclic pitch coefficient for the $-\sin\psi$ term in Fourier series expansion of the rotor blade cyclic pitch, deg

B'_{1_s} experimental lateral cyclic pitch required to trim to zero first harmonic of flapping given in Ref. 7, deg

ΔB_{1_s} experimental lateral cyclic pitch required to trim to zero first harmonic of flapping for zero collective pitch, twist, and shaft angle in Ref. 7, deg

c	blade chord, ft
c_d	local section drag coefficient, section drag force$/\left(\frac{1}{2}\rho U^2 c\right)$
$c_{d_{NS}}$	section drag coefficient -- no stall
$c_{d_{SS}}$	steady-state section drag coefficient
c_ℓ	section lift coefficient, section lift force$/(\frac{1}{2}\rho U^2 c)$
c_n	section normal force coefficient, section normal force$/(\frac{1}{2}\rho U^2 c)$
$c_{m_c}/4$	section pitching moment coefficient, section pitching moment$/(\frac{1}{2}\rho U^2 c^2)$
C_L/σ	rotor lift coefficient to solidity ratio, rotor lift$/\rho\pi R^2 (\Omega R)^2 \sigma$
C_{PF}/σ	rotor propulsive force coefficient to solidity ratio, rotor propulsive force$/\rho\pi R^2 (\Omega R)^2 \sigma$
C_Q/σ	rotor torque coefficient to solidity ratio, rotor torque$/\rho\pi R^3 (\Omega R)^2 \sigma$
e	flapping hinge offset from the hub center, ft
g	acceleration of gravity, ft/sec^2
ℓ	local distributed loading, lb/in.
L	rotor lift force, vertical component of rotor resultant force (normal to flight velocity), lb
M	Mach number
M_1, M_2	limit mach numbers to which scaled unsteady aerodynamic data are used for α's above and below steady-state stall (see Fig. 4)
$M_{1,90}$	advancing tip Mach number
R	rotor radius, ft
U	resultant blade section velocity, ft/sec
U_p	component of U normal to both U_T and the local span axis of blade, upflow is positive, ft/sec

U_T	component of U parallel to plane of rotation and normal to local span axis of blade, ft/sec
V	free-stream velocity, knots
$\bar{x}$	blade radial station measured from the hub center divided by R
x	longitudinal nonrotating hub coordinate parallel to the tip path plane, ft
y	lateral nonrotating hub coordinate parallel to the tip path plane, ft
z	vertical hub coordinate perpendicular to the tip path plane, ft
α	section angle of attack, deg
α_c	rotor control angle of attack, deg
$\alpha_{max,L}$	angle of attack where the section lift is a maximum, deg
$\alpha_{max,u}$	maximum unsteady angle of attack, deg
α_{OL}	section angle of attack for zero lift, deg
α_s, α_s'	rotor shaft angle from plane perpendicular to the free-stream velocity, positive when shaft tilts downstream, prime denotes wind tunnel measurement, deg
$\Delta\alpha_s$	wind tunnel shaft angle correction increment due to wind tunnel wall interference, deg
α_{sm}	steady-state stall angle for pitching moment coefficient, deg (see Fig. 4)
α_{sn}	steady-state stall angle for normal force coefficient, deg (see Fig. 4)
α_{st}	angle at which steady-state drag coefficient initially equals $c_n \sin\alpha$, deg (see Fig. 7)
α_{TTP}	$\alpha_s + a_{1_h}$, deg
β	local blade flap angle including contributions due to bending, deg

δ_3	pitch-flap coupling
θ_e	local blade elastic twist angle about the elastic axis, positive nose up, deg
θ_1	linear built-in twist rate, positive when tip pitch greater than root pitch, deg
θ_{75}	blade collective pitch as measured at the 0.75 R spanwise station, deg
μ	advanced ratio, $V\cos\alpha_s/\Omega R$
ρ	air density, slugs/ft^3
σ	rotor solidity, $bc/\pi R$
ϕ	local inflow angle, $\tan^{-1} U_P/U_T$, deg
ψ	rotor azimuth angle measured from downwind position in direction of rotation, deg
ω	frequency, rad/sec
$\bar{\omega}_{w_1}$	frequency of first flapwise bending mode divided by Ω
$\bar{\omega}_{v_1}$	frequency of first edgewise bending mode divided by Ω
$\bar{\omega}_{\theta_1}$	frequency of first torsional mode divided by Ω
Ω	rotor angular velocity, rad/sec
$(\dot{\ })$	first derivative with respect to time
$(\ddot{\ })$	second derivative with respect to time

ROTOR CHARACTERISTICS AND WIND TUNNEL DATA

H-34 Rotor Data

The experimental results used in this investigation were obtained from wind tunnel tests of a H-34 helicopter rotor. This is a fully articulated, 4-bladed rotor producing a thrust of approximately 13,000 lb at design gross weight. The blade dimensional and structural data were obtained from Ref. 19 and a summary of the pertinent information is presented below.

H-34 Rotor Characteristics

Rotor radius, R, ft	28
Blade chord, c, ft	1.367
Cutout radius	0.16 R
Rotor solidity, $bc/\pi R$	0.062
Reference area, bcR, ft^2	153.1
Blade moment of inertia about flapping hinge, $ft-lb-sec^2$	1264
Blade weight moment about flapping hinge, lb-ft	2265
Flapping hinge offset	0.036 R
Number of blades, b	4
Airfoil section	NACA 0012
Blade taper ratio	1.0
Lag damper, ft-lb/rad/sec	2730
Pitch-flap coupling, δ_3	0
Nondimensional frequency of first flapwise bending mode, $\bar{\omega}_{w_1}$	2.68
Nondimensional frequency of first edgewise bending mode, $\bar{\omega}_{v_1}$	3.33

Nondimensional frequency of first torsional mode, $\bar{\omega}_{\theta_1}$	7.29
Blade chordwise center of gravity location	$0.238c$
Blade chordwise elastic axis location	$0.238c$

Wind Tunnel Test Conditions

The wind tunnel test conditions were selected so that various levels of rotor stall could be analyzed as well as unstalled conditions. In addition, it was desirable to select conditions which would provide variations in blade twist and rotor advance ratio. Increased blade twist is predicted by classical theory to delay stall onset while it was expected that unsteady aerodynamic effects would increase significantly with advance ratio. A summary of the nominal test conditions investigated is given below:

Wind Tunnel Test Conditions

Forward Velocity (knots)	Advance Ratio	Blade Twist (deg)	Collective Pitch (deg)	Shaft Angle (deg)	Air Density (slugs/ft^3)
117	0.3	-8	8	-5, 0, 5, 10	0.002203
116	0.3	0	8	-5, 0, 5, 10	0.002213
194	0.5	0	8	-5, -3, 2, 5	0.002036

Wind Tunnel Corrections

Two tunnel interference corrections are applicable to the experimental data presented in Ref. 7. The first is a small correction to rotor angle of attack to account for the restraining effect of the tunnel walls on the average rotor inflow. The second is a cyclic pitch correction to account for the unsymmetrical flow produced by the rotor support module.

The formula used for the angle of attack correction is given below and was determined from Ref. 20, assuming the rotor behaves as a circular fixed wing.

$$\alpha_s = \alpha_s' + \Delta\alpha_s$$

8

where
$$\Delta\alpha_S = 0.54\, C_L / \sigma\mu^2$$

The coefficient 0.54 is a function of the ratio of the disc area to the tunnel cross-sectional area and of the shape and type of the test section. The maximum correction angle for the conditions investigated was calculated to be 0.7 deg. A further check on the general validity of this correction for the most extreme condition considered was made by computing $\Delta\alpha_S$ according to the theory of Ref. 21. A comparison of the results indicated that the difference between the fixed wing theory of Ref. 20 and the theory of Ref. 21 was negligible. The theory of Ref. 21 also predicts the existence of a forward velocity correction factor at high values of $C_L/\sigma\mu^2$; however, for the conditions considered this velocity correction proved negligible.

Cyclic pitch correction angles were included to account for the unsymmetrical flow conditions by the hub and support module interference. This dissymmetry in the flow was evidenced by the nonzero cyclic pitch inputs required during the test to eliminate the first harmonic of blade flapping under conditions of zero lift (i.e., zero blade twist, zero shaft angle, and zero collective pitch). If the rotor were operating in undisturbed air, no such inputs would be required. The corrections were applied according to the following formulas:

$$A_{1_S} = A'_{1_S} - \Delta A_{1_S}$$
$$B_{1_S} = B'_{1_S} - \Delta B_{1_S}$$

where the prime quantities are the recorded input cyclic pitch angles at each test condition. The delta values were obtained from the zero lift conditions measured for the zero twist rotor at various tunnel speeds. These quantities are presented in Ref. 7 and are summarized on Fig. 2. Average correction angles for the two forward speed conditions investigated are given by the solid curves in Fig. 2. Table I contains a summary of the corrected control angles for use in the Blade Response Program as well as the corresponding experimental rotor performance data. In the experimental data, the shaft angles, α_S, of Table I are equivalent to the recorded tip path plane angles, α_{TPP}, since at each test point the first harmonic of blade flapping was reduced to zero through cyclic pitch inputs.

9

Additional flow interference may be caused by the interaction between the rotor induced velocity and the flow around the hub and fuselage during lifting conditions. An attempt has been made to account for such inteference by presenting the results in terms of rotor tip path plane angle rather than shaft angle of attack. The former should be a measure of the mean angle of attack of the rotor while the latter is a rather arbitrary quantity which in no way reflects the amount of interference that may be present. This procedure is equivalent to assuming that the incremental flapping due to aerodynamic interference could be predicted given an accurate model of such interference. Table II contains the shaft angles, blade flapping angles, and rotor tip path plane angles of attack obtained from the computer output for all conditions investigated. Differences in the input shaft angles of Table I and the output shaft angles of Table II are due to a finite convergence tolerance used in the calculations. The tip path plane angle was computed by the following equation

$$\alpha_{TPP} = \alpha_s + a_{1_h}$$

Here, to be consistent with the test results, a_{1_h} is the longitudinal flapping coefficient measured at the flapping hinge.

ANALYTICAL METHODS

The problem of predicting rotor aerodynamics in forward flight is not a simple task. Even if the flow field induced by the rotor wake's vortex system is assumed to be known, one is still faced with predicting the characteristics of lifting elements operating in compressible flow and executing complex unsteady motions into stall. Unsteady effects arise not only from angle of attack variations but also from variations in blade sweep angle and local velocity. No closed form solution is currently possible and any analysis must involve assumptions which strike a reasonable balance between accuracy and practicality. The UAC Rotor Analysis used in this study and shown in block diagram from in Fig. 3 is no exception in this regard. The analysis is under continual development with recent emphasis being placed on the modeling of unsteady aerodynamic and rotor wake distortion effects. It is beyond the scope of this report to provide a complete documentation of all facets of the analysis. Such documentation is, however, available in the general literature (Refs. 12 through 14, and 18). New features of the analysis used in this study are fully documented herein. Also, to provide some framework in which to evaluate the results presented, a summary of the basic assumptions of the analysis is given below and is followed by a limited discussion of some of the more important technical features of the analysis.

Assumptions

1. The rotor rotational velocity is constant.

2. Two-dimensional unsteady normal force and pitching moment data obtained for an airfoil executing forced constant amplitude sinusoidal pitch oscillations under constant velocity conditions can be applied under rotor blade operating conditions involving velocity variations and multi-harmonic angle of attack variations. It is assumed that this application can be accomplished by generalizing the basic data to functions of section angle of attack, angular velocity, and angular acceleration.

3. The effects of compressibility on unsteady airfoil characteristics can be approximated by scaling the generalized incompressible unsteady data using scaling procedures which generally predict the effect of compressibility on steady-state airfoil characteristics.

4. Quasi-steady, two-dimensional aerodynamic theory is applicable for those blade sections operating at conditions of high Mach number and high angle of attack or in reversed flow.

5. Unsteady drag coefficients can be synthesized from steady-state values using corrections proportional to the differences between steady, unsteady, and potential flow lift characteristics (see text for further discussion).

6. The velocities induced at the rotor by the vortex system representing the rotor wake can be computed using a lifting-line type of analysis. The position of vortex filaments trailed from the blade sections inboard of the tip are assumed to be nondistorted (i.e., vortex elements are convected at a velocity equal to the vector sum of the local free stream velocity and the momentum inflow velocity). The vortex at the blade tip on the other hand is allowed to distort (i.e., is free to convect at a velocity equal to the vector sum of the local free stream velocity and the velocity induced by the various elements of the tip vortices.

7. The blade has an elastic axis so that blade deflections can be considered as the superposition of two orthogonal translations of this axis and a rotation about it.

8. Principal blade flexibility effects can be accounted for by considering only one torsional, three flapwise, and two edgewise vibratory modes.

9.   Blade flap and lag hinges are coincident for articulated rotors.

10.   The local center of gravity is assumed to lie on the major principal axis of the section.

11.   The following quantities can be assumed to be small in comparison to unity:

a.   Flap and lead angles (in radians) and their derivatives

b.   Ratios of elastic deflections to rotor radius and their derivatives

c.   Ratios of chordwise distances (i.e., chord, center-of-gravity offset, etc.) to rotor radius

d.   Built-in twist (in radians)

e.   Ratio of flap-lag hinge radial distance from center of rotation to rotor radius

f.   Froude number $(g / \Omega^2 R)$

g.   Ratios of blade thickness dimensions to chord

12.   On the basis of Assumption 11, the following types of terms in the equations noted can be neglected as higher order:

a.   Flapwise and edgewise bending equations:

(1)   Second order procducts involving elastic coordinates, distance between blade elastic axis and center of gravity axis

(2)   Third order products involving elastic coordinates, chordwise distances, flap angle, lead angle, built-in twist, and flap-lag hinge offset

b.   Torsional equation:

(1)   Third order products involving elastic coordinates, and distance between blade elastic axis and center of gravity

(2)   Fourth order products involving elastic coordinates, chordwise distances, flap angle, lead angle, built-in twist, and flap-lag hinge offset

12

c. Flap angle and lead angle equations -- second order terms involving products of elastic coordinates, chordwise distances, and built-in twist.

d. Section velocity equations:

(1) Second order products of elastic coordinates

(2) Third order products involving the elastic coordinates, chordwise distances, flap angle, lead angle, built-in twist twist, and flap-lag hinge offset as factors

e. All equations -- the spanwise component of acceleration due to gravity.

Blade Response Program

This program determines the fully-coupled response of a flexible rotating blade, given the distribution of induced velocities over the disc and the rotor control angles. The blade deflection is expanded in terms of its uncoupled natural vibratory modes (normal modes). The normal mode technique is widely used to solve aeroelastic problems (see, for example, Ref. 22, p. 125) and facilitates the numerical integration of the blade equations of motion through elimination of dynamic coupling terms. In this investigation, the blade response is assumed to be composed of a rigid body flapping mode, three elastic flapwise modes, a rigid body lagging mode, two elastic edgewise modes, and one elastic torsional mode. The basic differential equations of motion governing the response of each of the blade modes are given in Ref. 12.

The aerodynamic model described in the analysis of Ref. 12 was based on the use of steady-state, two-dimensional airfoil data. In accordance with quasi-steady theory (Ref. 22, p. 279), (1) the local section angle of attack was defined by the velocity components at its three-quarter chord point and (2) the theoretical damping moment in pitch was included. In defining the local angle of attack for conditions with variable inflow, the inflow at the rotor induced by the vortex system representing the rotor wake was computed using an analysis similar to that of Ref. 14. Wake distortion effects are also included as described in Ref. 13. Recent modifications to the aerodynamic model have been made (Ref. 18) in an attempt to incorporate a better representation of the effects of the shed wake vorticity (wake vorticity arising from time-wise variation of blade bound vorticity) at all angles of attack and, in particular, those above steady-state stall. To accomplish

13

this, steady-state airfoil data has been replaced, where possible, by unsteady data. The latter were derived from available data for a two-dimensional airfoil executing forced, pure sinusoidal pitching motion. Typical rotor blade operating conditions involve variations in the local reduced frequency $c\omega/2U_T$ with time as well as the presence of several harmonics in the local angle of attack variations. A rigorous method for applying sinusoidal data in such circumstances has not yet been established. In this investigation, it has been hypothesized that the sinusoidal data could be generalized, through cross plots, to functions of section instantaneous angle of attack (α), angular velocity (A), angular acceleration (B), and Mach number (M). Given the local values of these parameters for each section, its unsteady lift and moment can be computed.

As envisioned, unsteady normal force and moment data from Refs. 16 and 17 for the NACA 0012 airfoil were to be generalized to functions of the parameters noted above, with the Mach number range covered extending up to 0.6. However, because of the limited scope of the data from Ref. 17, it was not possible to recast that data (through cross plots) in the form desired. Therefore, an attempt was made to scale the incompressible data of Ref. 16 to account approximately for compressibility effects. A scaling procedure based on the steady-state stall angle was postulated. The steady-state normal force and pitching moment characteristics of the NACA 0012 airfoil, normalized in terms of stall angle, were used to evolve separate scaling laws for normal force and moment. These steady-state scaling laws were then assumed to apply to the unsteady blade characteristics as well. Details of the techniques are described in Ref. 18. Conventional, steady-state lift and moment data for the NACA 0012 airfoil section were used for those combinations of angle of attack, α, and Mach number, M, for which either unsteady data were not available or the scaling procedures were believed suspect. Figure 4, obtained from Ref. 18, indicates the α, M regions where steady and unsteady data were used as well as transition regions where normal force and pitching moment coefficients were obtained by interpolating between the steady and unsteady data.

A sample plot showing the form of the generalized unsteady data is given in Fig. 5. Normal force and pitching moment coefficients are presented for one Mach number and angular acceleration parameter for both positive and negative angular velocities. The results indicate that significant departures from steady-state values can occur depending on the operating environment (α, M, A, B) of the airfoil. A complete tabulation of the generalized data is given in Ref. 18.

As noted above, unsteady experimental results were available only for normal force and pitching moment. Unsteady drag characteristics were approximated from consideration of the occurrence and severity of stall as indicated by departures of the lift force from potential flow values. The unsteady drag coefficient was computed by taking the steady-state value and adding to it an increment based on a scaling ratio determined from the steady, unsteady, and potential flow lift data. The ratio used depends on whether the particular operating condition (α, M, A, and B) produces a lift force which lies in a region bounded by the potential flow and steady-state lift curves or in a region bounded by the steady-state and so-called fully-stalled lift curves. The airfoil is defined as being fully-stalled when the drag coefficient is given by $c_n \sin\alpha$. The fully-stalled values of c_n were taken as being proportional to the steady state c_n values in stall. The constant of porportionality used was 0.5 and was estimated by surveying the unsteady c_n tables of Ref. 18 and noting that values of c_n as low as approximately 50 percent of the steady values could result under adverse combinations of angular velocity and angular acceleration. The equations used to estimate the drag coefficient for the two regions of operation are given below and a typical unsteady drag hysteresis loop computed by this procedure, showing the various proportioning quantities, is given in Fig. 6

$$c_d = \begin{cases} c_{d_{ss}} - \dfrac{A'}{B'}D' & for \ A' \geq 0 \\[2ex] c_{d_{ss}} + \dfrac{A''}{B''}D'' & for \ A'' \geq 0 \end{cases}$$

where the prime and double prime quantities are defined in Fig. 6. The steady state loops shown in Fig. 6 reflect the changes in section characteristics due to Mach number variations around the azimuth. The type of approach involved is illustrated by the following simple example in which the drag for steady-state operation is computed. Referring to Fig. 7 the unsteady drag for the unstalled airfoil is approximated by the steady value while that for the fully-scaled airfoil is simply given by the component of the normal force in the streamwise direction (i.e., $c_{d_{full-stall}} = c_n \sin\alpha$). For the partially-stalled airfoil, the drag is assumed to be linearly related to the departures of the actual normal force values from potential flow values. The formula for drag coefficient in this transition region is given in Fig. 7. Figure 8 presents a comparison of measured steady-state drag results with those computed by this approach for an NACA 0012 airfoil at three Mach numbers and good agreement is indicated.

While no guarantee can be made as to the accuracy of the unsteady drag
generated by this procedure, it should be noted that the procedure, as evolved,
yields what would appear to be qualitatively correct drag results for the
limiting cases of very high and very low frequency oscillations where the lift
force approaches potential flow and steady-state values, respectively.

Circulation Program

The function of this program is to compute the circulation distribution
over the rotor, given the distributions of section angle of attack, α, angular
velocity parameter, A, and angular acceleration parameter, B, over the blade
as well as a specified geometry of the rotor wake. Initially, the wake is
approximated by the classical skewed helicoid defined where the vortex elements
generated by the blade are convected downstream relative to the blade at a
resultant velocity equal to the vector sum of the blade rotational velocity,
rotor forward velocity, and average momentum velocity through the disc. Once
the circulation distribution is known, the inflow velocities induced at the
blade by the bound and wake vorticity of the rotor can be computed. An
iteration between the Circulation and Blade Response Programs is then used to
assure compatibility of the inflow velocities and the blade aerodynamic and
dynamic boundary conditions. The iteration procedure is further outlined
following the Distorted Wake Geometry Program section.

The technical approach used in the Circulation Program is basically
similar to that described in Ref. 14 and generally represents a rotary-wing
equivalent of the classical lifting-line approach used successfully for fixed
wings. There are, however, some differences between the UAC Circulation
Program and that described in Ref. 14. These are discussed below.

The first of these differences is the elimination of all shed vorticity
elements (elements arising from variations of blade bound vorticity with time)
in the wake model -- a modification which contributed substantially to
reducing computing time without significantly altering computed circulations
and associated inflow velocities. Thus, the only vortex elements retained in
the wake are trailing elements; i.e., those arising from spanwise variations
in bound circulation. As in Ref. 14, the strength of the trailing elements is
permitted to vary from point to point in the wake to reflect the variation
in bound circulation that occurs as the blade rotates. It is believed that a
more accurate representation of shed vorticity effects is obtained by the
previously mentioned use of unsteady airfoil data in the Blade Response Program.
The use of two-dimensional, unsteady data basically implies that the primary
effects of the shed vorticity in a helical rotor wake are due to the wake
region near the blade and thus can be approximated by those in a fixed-wing

16

type of wake as indicated schematically in Fig. 9. Miller (Ref. 15) shows that this approximation is reasonable at the rotor advance ratios of interest to this study. It should also be mentioned that this type of approach greatly facilitates the inclusion of nonlinear unsteady aerodynamic effects due to stall.

Another significant difference between the UAC Circulation Program and that of Ref. 14 lies in the treatment of unsteady effects on lift curve slope, a, angle for zero lift, α_{OL}, and stall angle, $\alpha_{max,L}$. In Ref. 14, steady-state values were used for these quantities. In the present study, a, α_{OL}, $\alpha_{max,L}$ were considered to be functions of the section angular velocity and angular acceleration parameters as well as Mach number. As in Ref. 14, the local bound circulation is assumed proportional to section angle of attack (measured from the zero lift angle) until $\alpha_{max,L}$ is reaches, following which no further increase in circulation is permitted. The functional relationships involved and the scaling procedures to simulate compressibility effects are given in Ref. 18.

Distorted Wake Geometry Program

As mentioned previously, the Circulation Program required that the rotor wake geometry be specified in order for circulation and induced velocities to be determined. In lieu of more precise information, the assumption has usually been made that the wake is a classical nondistorted helicoid defined from momentum considerations. Initial evaluation studies conducted at the Research Laboratories indicated that this assumption could compromise the quantitative accuracy of any induced velocity analysis. To eliminate the necessity for assuming the wake geometry, an analytical method (Distorted Wake Geometry Program) for computing more realistic wake geometries has been developed by the Research Laboratories. The basic approach used is straightforward and involves the following: First, additional wake geometry is assumed along with the distribution of circulation strengths of the various vortex elements comprising the wake. The classical Biot-Savart Law is then applied to determine the velocities induced by each vortex wake element at numerous points in the wake. These distorting velocities are then numerically integrated over a small time increment to obtain new wake element positions. The process of alternately computing new velocities and positions is continued until a converged, periodic distorted wake geometry is reached. By dividing the wake into near and far wake elements, an approximate analysis which eliminates the potentially massive computing cost requirements has been developed, without significantly compromising the accuracy of the technical results. In applying the program to this investigation, only the tip vortices were allowed to distort. The inboard filaments assumed a classical

17

nondistorted geometry based on momentum velocity. In view of the secondary role of the inboard vortex filaments, computation times required to compute their distortions were considered to be prohibitive, especially when one considers that the circulation strengths of the individual inboard vortex filaments are an order of magnitude less than that of the tip vortex. Further details of the procedures used to compute wake geometries are given in Ref. 13.

Iteration Procedure

The procedure used in iterating between the various programs of the UAC Rotor Analysis is depicted schematically in the block diagram of Fig. 3. Briefly the following steps are taken:

1. Using a constant induced velocity distribution, the specified flight condition control angles and the desired airfoil data, the Blade Response Program is used to compute the blade response compatible with the section operating conditions, α, A, B, and M. The calculations were performed using 15 blade radial segments and an azimuth integration increment sufficiently small to insure convergence of the blade motions (generally 2.5 to 5.0 deg).

2. If variable inflow is not desired, pertinent blade response and performance information is provided and no further calculations are performed.

3. If variable inflow is desired, the section operating conditions are used as input to the Circulation Program as well as the distributions of a, α_{OL}, $\alpha_{max,L}$. In addition, a nondistorted classical wake geometry is assumed using nine blade radial stations and 30 deg azimuthal increments to develop the blade trailing and bound wake patterns.

4. If wake distortions are not desired, the variable induced velocities obtained from the Circulation Program are substituted for the constant induced velocities and entered in the Blade Response Program. The section operating conditions are recomputed, passed into the Circulation Program and the procedure repeated until convergence is achieved.

5. If wake distortions are desired, the circulations obtained from the Circulation Program are used as input to the Distorted Wake Program to determine the new wake geometry.

6. The new wake geometry characteristics are then used in the Circulation Program to recompute induced velocities.

7. The induced velocities are returned to the Blade Response Program and the procedure repeated until convergence is achieved.

Normally, one cycle through the three programs is sufficient. For this investigation the accuracy of a single iteration was verified by completing two cycles for one flight condition and comparing the rotor performance results after each cycle. The procedure was performed for the -8 deg twist rotor at an advance ratio of 0.3 and a shaft angle of -5 deg. Flexible blades and steady aerodynamics were assumed and the performance differences between the two cycles amounted to less than 1 percent in lift and torque and less than 2 percent in propulsive force.

PRESENTATION OF RESULTS

The UAC Rotor Analysis, as diagramed in Fig. 3, was employed to compute blade responses and the lift, torque, and propulsive force of the rotor. Calculations were initially made assuming rigid blades (i.e., flap and lag motions only), steady aerodynamics, and constant inflow. Such results are termed Classical Theory Results and are equivalent to the results of Ref. 1 with the exception of small effects due to rigid blade lag motion which was not included in the computer program used in Ref. 1. Additional calculations were then performed in which the effects of blade flexibility, unsteady aerodynamics, and variable inflow (with and without wake distortion) were systematically added. All results are presented in Figs. 10 through 25 in terms of rotor lift, propulsive force, and torque as functions of rotor tip path plane angle of attack. Computed flapping motions and rotor shaft angles are given in Table II. As noted previously, the range of conditions considered encompasses both stalled and unstalled operation and extends significantly beyond the lower blade stall limit as defined in Ref. 1 (see Fig. 1). This has allowed a comparison to be made between theory and experiment at various levels of blade stall. Correlations of theoretical and experimental results at different advance ratios (0.3 and 0.5) were made to demonstrate the magnitude of unsteady aerodynamic effects, since these are expected to increase significantly with advance ratio. Additionally, two blade twist values (0 deg and -8 deg) were considered to provide an indication of the accuracy of the analysis when applied to rotor configurations having different angle of attack distributions at stall.

The results are presented in four general groupings to allow a thorough assessment of the individual effects under investigation. The groupings are: (a) the effects of blade flexibility, Figs. 10 through 13, (b) the effects of unsteady aerodynamics, Figs. 14 through 17, (c) the effects of variable inflow without wake distortions, Figs. 18 and 19, and (d) the effects of variable inflow with wake distortions, Figs. 20 through 25. Each figure shows results

19

for three combinations of rotor advance ratio and blade twist: (a) 0.3 advance ratio and -8 deg twist, (b) 0.3 advance ratio and 0 deg twist, and (c) 0.5 advance ratio and 0 deg twist. The individual effects of each refinement (flexibility, unsteady aerodynamics, etc.) have been evaluated starting with various base or reference conditions to determine the influence of such conditions on the effect of primary refinement being examined. For example, the effects of blade flexibility are presented in Fig. 10 where results are given with and without blade flexibility assuming constant inflow and steady aerodynamics. Similar results are presented in Figs. 11, 12, and 13 which show the effects of introducing unsteady aerodynamics, variable inflow without wake distortions, and variable inflow with wake distortions to form new base or reference conditions. The order in which the various refinements were added is summarized in Table II. In addition, a detailed cross reference between the various refinements and corresponding figure is given in Table III.

DISCUSSION OF RESULTS

The objective of this section is to examine the individual effects produced by the addition of blade flexibility, unsteady aerodynamics, and variable inflow. The mechanisms by which these refinements influence the response and performance of the rotor will also be discussed in some detail. Results relative to the blade section aerodynamics, flapping angles, bending and torsional responses, and loading time histories are presented where necessary to aid in the understanding of the various observed trends.

Blade Flexibility

The effect of introducing blade flexibility into the analytical model are shown in Figs. 10 through 13. In general, it was found that the principal effect of flexibility was to reduce rotor torque at the higher rotor lift coefficients where the rotor is susceptible to stall. The reduction in torque is in the direction required for improved correlation with experiment; however, when combined with unsteady aerodynamic effects, the total reduction is larger than that required for correlation (e.g., Fig. 11). Rotor lift was affected to a considerably less extent with small reductions in lift being noted for unstalled conditions where the blade sections are operating primarily on the linear portion of the lift curve. Finally, basic rotor propulsive force characteristics remained essentially unchanged when blade flexibility was introduced. The causes of the observed trends are discussed below.

The elastic deflection modes used to simulate blade flexibility consisted of three flapwise and two edgewise bending modes as well as one torsional mode. The primary modes which affect the aerodynamics are the torsional mode and the first flapwise bending mode. Of these, only the torsional response, which has a direct influence on the blade angle of attack distribution, has an important effect on the integrated forces and moments generated by the rotor. The first flapwise mode response, which alters the local inflow angle due to bending displacements and velocities, had a significant effect only on the cyclic blade loading.

The influence of the blade torsional response on rotor torque will now be discussed. At the low tip path plane angles, below rotor stall, the differences between the rigid and flexible blade results are generally small and the correlation with the experimental results is consistent with that of the lift. However, at the high angles of attack, a large reduction in torque is computed using flexible blades. The reduction is related to a large decrease in retreating blade angles of attack. This, in turn, has a major influence on section drag coefficients since $dc_d/d\alpha$ is high at these angles. The blade torsional deflection at the 75 percent radial station for the maximum rotor angle of attack condition is shown in Fig. 26 and indicates the large (up to -3 deg) nose down deflections computed. The resulting angle of attack variation, including the induced inflow angles caused by subsequent blade flapping and bending, is shown in Fig. 27. The difference between the rigid and flexible blade angle of attack consists of the torsional deflection, Fig. 26 and change in the inflow angle due to flapping and bending, Fig. 28. Finally, the reduction in drag coefficient resulting from the lower blade angles of attack is shown in Fig. 29. (This figure also shows the effect of unsteady aerodynamics which will be discussed later). Further investigation indicated that the large torsional deflections shown in Fig. 26 resulted from the large aerodynamic pitching moments predicted at the high blade angles. The pitching moment effects were examined by simply setting the airfoil pitching moment coefficients to zero in the Blade Response Program. The resulting torsional deflections are shown in Fig. 30 where it is evident that a large portion of the deflection has been eliminated. This results in a higher section angle of attack over the retreating side and produces a 60 percent increase in torque.

As noted previously, the introduction of blade flexibility also caused a reduction in rotor lift when the rotor was unstalled (see, for example, Fig. 10a, at the lower α_{TPP}'s). This was also traced to the torsional response of the blade, an example of which is shown in Fig. 31. An average nose down deflection is evident and, as might be expected, this produces an effect similar to a reduction in collective pitch, namely to reduce the effective blade angles (Fig. 32) and hence rotor lift. The cause of this nose down

deflection was found to be the forward position of the blade center of gravity axis. For the performance results presented in Figs. 10 through 25, the mass and elastic axes were located at 0.238 c. This meant that a steady nose down pitching moment was produced by the couple formed by the blade lift and the centrifugal force component normal to the blade span. The sensitivity of the rotor lift, propulsive force and torque to placement of the center of gravity axis is shown in Fig. 33. The higher values noted with a rearward movement of the axis are in the direction of improved correlation. It is interesting to note that a one percent error in the blade mass axis location is approximately equivalent to a 0.2 deg error in collective pitch at this advance ratio. The principal effect of the elastic axis location is to vary the cyclic torsional moment due to the variations in lift. A negligible effect on steady rotor forces and moments was noted when the elastic axis was moved rearward 1.2 percent to the quarter chord.

The importance and sensitivity of the torsional response of the blade is not surprising. Typical rotor blades have large aspect ratios ($\sim$20) and their structural stiffness is much smaller than that of a fixed wing designed to carry the same lift. Flapwise deflections of the blade are kept in hand in this situation by the powerful effective stiffness produced by the centrifugal forces acting on the rotating blade. The centrifugal forces, however, provide little additional stiffening to the torsional response of the blade. As a result, the potentially large torsional moments due to either aerodynamic or dynamic forces must be very carefully balanced if large torsional deflections are to be avoided. This rather extreme sensitivity of the blade in torsion places more stringent accuracy requirements on those facets of the analysis which influence the torsional response since what would normally be considered small errors could, in this case, result in relatively large response.

Unsteady Aerodynamics

The effects of introducing unsteady aerodynamics into the calculation of the rotor characteristics are summarized in Figs. 14 through 17. Here results based on steady and unsteady aerodynamics are plotted for different reference conditions (i.e., with and without blade flexibility, etc.). The principal effects of using unsteady aerodynamics are to increase rotor lift and to reduce propulsive force and torque under conditions at high angles of attack where rotor stall would normally be predicted. To gain some insight into the cause of the observed trends, the aerodynamic characteristics of a representative blade station were examined. This was done at an advance ratio of 0.3 for the maximum rotor angle of attack condition with and without blade flexibility. The effects of unsteady aerodynamic on performance were similar

for both cases; however, the occurrence of transient stall flutter for the flexible blade case did not enable a straightforward analysis and for this reason only the rigid blade results will be discussed at this time. A short section describing the stall flutter response is presented later in this report.

Lift Characteristics - Comparing the results in Figs. 14 through 17 indicates the predicted stall using the classical theory has been eliminated with the use of unsteady aerodynamics and that the predicted slopes of the lift curves at each rotor angle of attack agree well with the test results. The closest agreement between theory and experiment was obtained using unsteady aerodynamics with rigid blades and constant inflow (Fig. 14). At constant input controls and shaft angle of attack, there are two phenomena which occurred as a result of the use of unsteady airfoil data: (1) an increase in the maximum acheivable section lift coefficients above steady-state stall values on the retreating blade, and (2) a change in local inflow angles caused by the self-adjustments in flapping resulting from changes in the retreating blade lift coefficients. The variation in section lift coefficient at the 75 percent radial station for the 0.3 advance ratio, -8 deg twist condition, is presented in Fig. 34 as a function of section angle of attack and in Fig. 35 as a function of blade azimuth position. The variation with angle of attack (Fig. 34) illustrates the familiar characteristics of both steady and unsteady airfoil lift data. The results using steady data demonstrate the typical steady-state variation with a maximum c_ℓ of 1.18 occurring at an angle of attack of 13 deg. The unsteady data curve indicates a slightly nonlinear lift curve slope (due to M variations) up to an angle of attack of 18 deg (c_ℓ = 1.68) beyond which lift is reduced as a result of a reduction in the angular velocity parameter, A. The final closure of the c_ℓ loop resembles conventional unsteady loops as depicted in Ref. 4. Figure 35 clearly indicates the increase in lift coefficient over the retreating side of the rotor as well as small increases in lift coefficient on the advancing side. This advancing side increase is a result of the change in angle of attack caused by readjustment of the blade flapping motion initiated by the increase in retreating blade lift. The change in blade flapping, Fig. 36, produces an increase in local inflow angle (and, hence, angle of attack) on the advancing side and a reduction on the retreating side. The variation in inflow angle is shown in Fig. 37. This increases the angle of attack and results in the loading increase on the advancing side. On the retreating side, reductions of up to 4 deg in angle occurred; however, because of the nature of the unsteady data (Fig. 34) significantly higher lift coefficients were obtained even at the lower angles. The distribution of loading around the azimuth for the 75 percent station is given in Fig. 38 and indicates the higher average loading predicted using unsteady aerodynamics. It should be emphasized that

23

this increased loading is caused not only by the increased lift coefficients of the retreating blade but also by the associated increased angles of attack on the advancing blade. The trends in the lift results using unsteady data are similar for all flight conditions and for each reference condition used in the analysis.

Propulsive Force Characteristics - As indicated in Figs. 14 through 17, significantly improved agreement in the propulsive force data is obtained when unsteady aerodynamics are included. This improvement is not surprising considering the improvement in lift noted earlier and the fact that the rotor thrust (~ lift) at high angles of attack contributes significantly to the propulsive force. Furthermore, the agreement near zero α_{TPP} is noteworthy since it implies that the theory predicts the rotor force normal to shaft with good accuracy. Also, it should be noted that the decrease in propulsive force noted with the addition of unsteady aerodynamics is due to the aft tilt of the thrust vector for the particular stall conditions investigated. For forward tilt of the lift vector in stall, increases in propulsive force would be expected.

Torque Characteristics - The rotor torque results exhibit similar characteristics in all the comparisons made in Figs. 14 through 17. Generally, reasonable agreement is indicated between the steady and unsteady aerodynamic results and the experimental results at the low angles of attack; however, the use of unsteady data causes a significant reduction in predicted torque at high angles of attack. For the conditions including blade flexibility, the torque results using unsteady data fall well below the experimental results at the maximum angle of attack (e.g., Fig. 15). The effects of flexibility have been shown previously to cause a reduction in angle of attack on the retreating side which produced a measurable reduction in section drag coefficient and, hence, rotor torque. The effect of unsteady aerodynamics produced a similar effect. This is shown in Figs. 39 and 29 where section drag coefficient for the 75 percent station is presented as a function of angle of attack and azimuth position, respectively. As a result of the absence of stall and the lower maximum section angles predicted for the unsteady case (see Fig. 29), the drag coefficient levels are lower than those for the stalled, steady case. It can be seen from Figs. 39 and 29 that the difference is almost entirely over the azimuth region from 210 deg to 360 deg. Also, as shown in Fig. 39, additional reductions in drag coefficient are predicted by the unsteady drag analytical model when the angular velocity parameter, A, is positive (α increasing). This reduction is not compensated by increases in drag coefficient when A is negative. In all the cases investigated, the references made to the unsteady aerodynamics includes the effect of the synthesized unsteady drag data; however, an estimate of the individual effect

of unsteady drag can be obtained by comparing the following results for rigid blades, constant inflow, and unsteady aerodynamics with and without unsteady drag:

	With Synthesized Unsteady Drag	With Steady State Drag
α_s, deg	10.7	10.7
α_{TPP}, deg	9.4	9.3
c_L/σ	0.111	0.111
c_{PF}/σ	-0.0158	-0.0147
c_Q/σ	0.00423	0.00504

The most significant difference in the above comparison is noted in the torque coefficient where a reduction of approximately 15 percent occurs when unsteady drag data are used.

The torque discrepancy described above was noted even when the most sophisticated analytical simulation was attempted (Fig. 17) and represents the principal discrepancy observed in this investigation. Improvements in correlation should be expected at the low angle of attack conditions if lift correlation were achieved, due to the corresponding increase in blade profile and induced drag. The effects of lift correlation on torque at the higher angles of attack are more difficult to assess since autorotative conditions may be approached depending on the method used to increase lift. Probably the most likely potential cause of the torque discrepancy lies in the use of synthesized unsteady drag data. Experimentally obtained unsteady drag data would obviously be extremely desirable.

Stall Flutter - While not a primary objective of this study, it should be noted that an important characteristic of unsteady aerodynamic, flexible blade analyses is the large amplitude, high frequency blade torsional responses that are often predicted at high angles of attack. This is a stall flutter phenomenon which can occur under certain combinations of unsteady aerodynamic parameters. The type of torsional deflections encountered are illustrated on Fig. 40 where they are compared with the torsional deflections assuming steady aerodynamics. The curves illustrate generally similar characteristics if the high frequency component of the torsional displacement is eliminated for the unsteady aerodynamic case. The high frequency response had no important direct effect on performance.

Variable Inflow

The results shown on Figs. 18 through 25 indicate a relatively small effect of variable inflow on the integrated rotor performance. The most notable effect is shown on Fig. 18a, where the classical rotor lift curve, indicating stall, was replaced by a relatively smooth curve which continued to increase in lift, although not linearly, up to the maximum shaft angle of attack. The change in character of the lift curve can be attributed to a generally lower average angle of attack of the outboard sections, thereby lessening the severity of stall on the retreating side. This is caused by the higher downwash velocities over the outer portion of the blade as a result of the strong tip vortex produced by the high lift coefficients in this region. Local induced velocities are calculated to be as high as eight times the constant inflow momentum value. A sample induced velocity distribution is shown on Fig. 41. (Note that these are velocities observed at the blade.) The induced velocities are relatively high on the retreating side (high tip loading and strong tip vortex) compared to those on the advancing side where the tip loading is generally low, producing a relatively weaker tip vortex. It is also interesting to note in Fig. 41 the ridge of upwash produced in the two forward quadrants. This is caused by the tip vortices generated by the passage of previous blades passing slightly below and downstream of this region. A comparison is made in Fig. 42 of the angle variations at the 87 percent station for the variable inflow and constant inflow conditions. The general reduction in section angle of attack due to variable inflow over a major portion of the azimuth is indicated.

The geometry of the distorted tip vortex and the undistorted lower strength inboard vortex filaments which produced the induced velocity patterns of Fig. 41 are shown in top view in Fig. 43 for one blade and rotor position. Presented in Figs. 44 and 45 are rear and side views of the tip vortex for the same condition for one and three-quarter revolutions. Both the classical helical wake and the distorted wake are shown. Distinguishing features of the distorted wake are the tip vortex roll-up, which occurs on the sides of the wake similar to that of a fixed wing wake, and the contraction of the fore and aft wake boundaries caused by presence of the semi-infinite wake. While the wake distortions can alter the distribution of loading over the disc (see Fig. 46) and thus should be important from a blade stress and rotor vibration standpoint, the distortions have little influence on the rotor performance as evidenced by the results shown on Figs. 20 and 21. The major influence of variable inflow on rotor performance originates from the downwash produced on the outboard sections of the blade by that portion of its trailing vortex immediately aft of the blade. The position, and hence the influence, of this region of the tip vortex is not significantly altered if the vortex is allowed to distort.

26

For all conditions investigated the addition of variable inflow generally produced a small reduction in rotor lift (for reasons discussed earlier) and a negligible effect on propulsive force and torque. Relative to the experimental results, variable inflow produced no general improvement in correlation; however, neither was the improved correlation noted with the introduction of unsteady aerodynamics altered.

CONCLUSIONS

1. The use of incompressible, two-dimensional unsteady lift and moment data, generalized in terms of section angle of attack and its first two time derivatives and scaled to approximate compressibility effects, significantly increases predicted rotor lift at nominally stalled rotor operating conditions. Predicted rotor torque and propulsive force are, on the other hand, reduced.

2. Additional reductions in predicted torque result when synthesized unsteady drag data are employed and/or when the blade torsional response is considered in the analysis.

3. The introduction of the blade flapwise and edgewise bending responses in the analysis had a negligible effect on predicted rotor stall characteristics.

4. The introduction of variable inflow, either with or without wake distortions, generally had a secondary effect on rotor stall characteristics.

5. The increase in lift and decrease in propulsive force predicted when unsteady aerodynamics are used significantly improve correlation with experimental results over that achieved with classical analyses.

6. The reduction in torque due to the use of unsteady aerodynamics is in the direction desired for improved correlation. However, when this reduction is combined with that caused by blade torsional flexibility, predicted torques result which are significantly less than those measured.

7. The increase in predicted lift noted when unsteady aerodynamics are used in the analysis results from the higher values of maximum lift coefficient achievable under unsteady conditions. This has two effects: (a) the lift capability of the retreating blades is increased and (b) as a result of the increased retreating blade capability, higher lifts are permitted on the advancing blade.

8. Rotor blades, because of their high aspect ratio and low torsional centrifugal stiffening, are typically quite flexible in torsion. Inasmuch as the torsional response strongly influences the blade aerodynamics, careful attention to its prediction is necessary if satisfactory correlation of rotor stall characteristics is to be achieved.

RECOMMENDATIONS

The results of this study have demonstrated the importance of unsteady normal force data in simulating the aerodynamic environment of rotor blades and contributing to a more reliable performance analysis. There is, however, a definite need for additional experiments to provide a more direct substantiation of the assumptions forming the basis for the unsteady aerodynamic model used in this study. It is recommended, therefore, that experiments be undertaken to (1) verify the commonly made assumption that unsteady airfoil data from sinusoidal oscillations can, in fact, be used to predict the characteristics associated with other types of motion into stall, (2) define unsteady drag characteristics, and (3) determine the influence of yawed flow on unsteady stall characteristics. Because of the potential complexity of such experiments, complementary analyses should also be pursued to provide both the guidance for efficient experimental programs and the basis for a longer term solution to the rotor unsteady aerodynamics problem. For example, the use of advanced boundary layer techniques to predict the point of incipient stall for an airfoil executing arbitrary motions appears to be feasible. The results of such an analysis obviously form the logical starting point for further study of the complete dynamic stall phenomenon.

In addition to the fundamental, long term studies recommended above, it is also recommended that the blade stress data obtained during the full scale tests be reduced and compared with the theoretical stress results obtained in the performance of this investigation. Preliminary comparisons of the vibratory stresses predicted by theory refinements indicate significant differences. These differences must necessarily be resolved before a reliable blade stress analysis can be developed. The requirement for such an analysis is becoming more critical at higher forward speeds where blade stress plays a more important role in determining maximum speed performance.

REFERENCES

1. Tanner, W. H.: Charts for Estimating Rotary Wing Performance in Hover and at High Forward Speeds. NASA CR-114, 1964.

2. Arcidiacono, P. J.: Aerodynamic Characteristics of a Model Helicopter Rotor Operating Under Nominally Stalled Conditions in Forward Flight. Journal of the American Helicopter Society, Vol. 9, No. 3, July 1964.

3. Rabbott, J. P.: Comparison of Theoretical and Experimental Model Helicopter Rotor Performance in Forward Flight. U. S. Army Transportation Research Command Report TCREC Technical Report 61-103, July 1961.

4. McCloud III, J. L. and McCullough, G. B.: Comparison of Calculated and Measured Stall Boundaries of a Helicopter Rotor at Advance Ratios from 0.3 to 0.4, NASA TN D-73, September 1959.

5. Sweet, G. E. and Jenkins, Jr., J. L.: Results of Wind Tunnel Measurements on a Helicopter Rotor Operating at Extreme Thrust Coefficients and High Tip Speed Ratios. Journal of the American Helicopter Society, Vol. 8, No. 3, July 1963.

6. Harris, F. D. and Pruyn, R. R.: Blade Stall--Half Fact, Half Fiction. American Helicopter Society, In., 23rd Annual National Forum Proceedings, No. 101, May 1967.

7. McCloud III, J. L. and Biggers, J. C.: An Investigation of Full-Scale Helicopter Rotors at High Advance Ratios and Advancing Tip Mach Numbers. NASA TN D-4632, 1968.

8. Harris, F. D., et al.: Rotor High Speed Performance, Theory versus Test. Proceedings of the V/STOL Technology and Planning Conference AFFDL, September 1969.

9. Betz, A., Hockstauftrieb von Flugeln an untaufenden Radern, Zeitschrift fur Flugwissensch aften, Vol. 9, No. 4/5, April-May 1961, pp. 97-99.

10. Sopher, R.: Three-Dimensional Potential Flow Past the Surface of a Rotor Blade. Paper presented at the 25th Annual National Forum of the American Helicopter Society.

11. Harris, F. D.: Preliminary Study of Radial Flow Effects on Rotor Blades. Journal of the American Helicopter Society, July 1966.

12. Arcidiacono, P. J.: Prediction of Rotor Instability at High Forward Speeds, Vol. I: Differential Equations of Motion for a Flexible Helicopter Rotor Blade in Steady Flight Including Chordwise Mass Unbalance Effects. USAAVLABS Technical Report 68-18A, February 1969.

13. Landgrebe, A. J.: Analytical Methods for Predicting Rotor Wake Geometry. Journal of American Helicopter Society, Vol. 14, No. 4, October 1969, pp. 30-32.

14. Piziali, R. A. and DuWaldt, F. A.: A Method for Computing Rotary Wing Airload Distributions in Forward Flight. TRECOM Report No. TCREC TR 62-44, November 1962.

15. Miller, R. H.: Unsteady Airloads on Helicopter Rotor Blades. Journal of the Royal Aeronautical Society, Vol. 68, April 1964, pp. 217-229.

16. Carta, F. O. and Niebanck, C. F.: Prediction of Rotor Instability at High Forward Speeds, Vol. III: USAAVLABS Technical Report 68-18C, February 1969.

17. Gray, L. and Liiva, J.: Two-Dimensional Tests of Airfoils Oscillating Near Stall. Vol. II - Data Report. USAAVLABS Technical Report 68-13B, April 1968.

18. Arcidiacono, P. J., et al.: Investigation of Helicopter Control Loads Induced by Stall Flutter. USAAVLABS Technical Report 70-2, March 1970.

19. Paglino, V. M. and Logan, A. H.: An Experimental Study of the Performance and Structural Loads of a Full-Scale Rotor at Extreme Operating Conditions. USAAVLABS Technical Report 68-3, 1968.

20. Pope, A.: Wind-Tunnel Testing. John Wiley and Sons, Inc., 1947.

21. Heyson, H. H.: Linearized Theory of Wind-Tunnel Jet-Boundary Corrections and Ground Effect for VTOL-STOL Aircraft. NASA TR R-124, 1962.

22. Bisplinghoff, R. L., Ashley, H., and Halfman, R. L.: Aeroelasticity. Addison-Wesley Publishing Co., Inc., 1955.

TABLE I - CORRECTED H-34 WIND TUNNEL TEST DATA

Velo-city, Knots	Collective Pitch, deg	Twist, deg	Shaft Angle, deg (a)	Lift Coefficient Solidity	Prop. Force Coefficient Solidity	Torque Coefficient Solidity	Velocity Tip Speed, μ	Longitudinal Cyclic Angle, A_{1_s}, deg	Lateral Cyclic Angle, B_{1_s}, deg
117	8	-8	-4.54	0.0780	0.00596	0.00424	0.301	-1.5	5.4
117	8	-8	0.58	0.1020	0.000004	0.00388	0.307	-2.1	6.8
117	8	-8	5.65	0.1106	-0.00704	0.00402	0.302	-2.3	8.6
117	8	-8	10.71	0.1204	-0.01849	0.00442	0.299	-3.1	9.7
116	8	0	-4.56	0.0752	0.00604	0.00448	0.304	-2.6	5.4
116	8	0	0.57	0.0977	0.00024	0.00415	0.304	-3.3	6.7
116	8	0	5.40	0.1094	-0.00778	0.00439	0.303	-3.8	8.3
116	8	0	10.68	0.1169	-0.01870	0.00484	0.300	-4.2	9.8
194	8	0	-4.92	0.0351	0.00080	0.00388	0.500	-2.7	6.2
194	8	0	-2.90	0.0461	0.00005	0.00387	0.507	-2.8	7.1
194	8	0	2.15	0.0736	-0.00383	0.00398	0.510	-3.3	9.4
194	8	0	5.18	0.0862	-0.00751	0.00422	0.507	-4.6	10.7

[a] $\alpha_s = \alpha_{TPP}$

Assumptions Made in the Calculations	Advance Ratio, μ	Twist, θ_1, deg	Shaft Angle, a_s, deg	Flapping, 1st Cosine Harmonic, a_{1h}, deg	Flapping, 1st Sine Harmonic, b_{1h}, deg	Tip Path Plane Angle of attack, α_{TPP}, deg
Rigid blades, steady	0.3	-8	-4.6	-0.5	0.9	-5.1
aerodynamics and constant	0.3	-8	0.5	-0.8	0.9	-0.3
inflow(Classical Theory)	0.3	-8	5.6	-0.3	2.7	5.3
	0.3	-8	10.7	0.4	3.4	11.1
	0.3	0	-4.7	-0.5	0.3	-5.2
	0.3	0	0.5	-0.2	1.0	0.3
	0.3	0	5.6	0.0	2.6	5.6
	0.3	0	10.7	-0.2	3.7	10.5
	0.5	0	-5.0	-0.1	-0.6	-5.1
	0.5	0	-2.9	-0.3	-0.2	-3.2
	0.5	0	2.1	-0.1	1.5	2.0
	0.5	0	5.2	-0.3	1.5	4.9
Flexible blades, steady	0.3	-8	-4.6	-0.5	-0.7	-5.1
aerodynamics and constant	0.3	-8	0.5	-1.2	-1.1	-0.7
inflow	0.3	-8	5.6	-1.4	-1.3	4.2
	0.3	-8	10.7	0.2	-1.3	10.9
	0.3	0	-4.6	-0.5	-0.7	-5.1
	0.3	0	0.5	-0.8	-1.1	-0.3
	0.3	0	5.6	-0.2	-0.9	5.4
	0.3	0	10.7	0.7	-0.3	11.3
	0.5	0	-4.9	-0.4	-0.9	-5.3
	0.5	0	-2.9	-0.6	-0.8	-3.5
	0.5	0	2.1	0.2	-0.3	2.3
	0.5	0	5.2	0.8	1.0	6.0
Rigid blades, unsteady	0.3	-8	-4.6	-0.4	0.9	-5.0
aerodynamics and constant	0.3	-8	0.6	-0.7	1.1	-0.1
inflow	0.3	-8	10.7	-1.3	3.3	9.4
	0.3	0	-4.7	-0.4	-0.2	-5.1
	0.3	0	0.5	-0.5	0.2	0.1
	0.3	0	10.7	-1.5	2.5	9.2
	0.5	0	-5.0	-0.0	-0.7	-5.0
	0.5	0	2.1	-0.7	1.5	1.4
	0.5	0	5.2	-1.0	1.4	4.2

TABLE II (Continued)

Assumptions Made in the Calculations	Advance Ratio, μ	Twist, θ_1, deg	Shaft Angle, α_s, deg	Flapping, 1st Cosine Harmonic a_{1_h}, deg	Flapping, 1st Sine Harmonic, b_{1_h}, deg	Tip Path Plane Angle of attack, α_{TPP}, deg
Flexible blades, unsteady aerodynamics and constant inflow	0.3	-8	-4.6	-0.6	-0.5	-5.2
	0.3	-8	0.5	-1.1	-0.9	-0.6
	0.3	-8	5.6	-1.6	-0.6	4.0
	0.3	-8	10.7	-1.4	-1.0	9.3
	0.3	0	-4.6	-0.6	-0.6	-5.2
	0.3	0	0.5	-0.8	-0.9	-0.3
	0.3	0	5.6	-1.1	-0.8	4.5
	0.3	0	10.7	-1.1	-0.5	9.6
	0.5	0	-4.9	-0.4	-0.8	-5.3
	0.5	0	-2.9	-0.6	-0.6	-3.5
	0.5	0	2.1	-0.8	-0.4	1.3
	0.5	0	5.2	-0.8	-1.1	4.4
Rigid blades, steady aerodynamics and variable inflow without wake distortions	0.3	-8	-4.6	-0.6	1.4	-5.2
	0.3	-8	0.5	-1.2	1.4	-0.7
	0.3	-8	10.7	0.1	3.9	10.8
	0.3	0	-4.7	-0.8	0.2	-5.5
	0.3	0	0.5	-0.8	0.5	-0.3
	0.3	0	10.7	-0.3	3.3	10.4
	0.5	0	-5.0	-0.2	-0.7	-5.2
	0.5	0	2.1	-0.2	1.5	1.9
	0.5	0	5.2	-0.4	1.4	4.8
Flexible blades, unsteady aerodynamics and variable inflow without wake distortions	0.3	-8	-4.6	-0.5	0.0	-5.1
	0.3	-8	0.5	-1.0	-0.1	-0.5
	0.3	-8	5.6	-1.3	0.2	4.3
	0.3	-8	10.7	-1.0	0.0	9.7
	0.3	0	-4.6	-0.6	-0.3	-5.2
	0.3	0	0.5	-1.1	-0.5	-0.6
	0.3	0	5.6	-1.1	-0.2	4.5
	0.3	0	10.7	-1.0	0.1	9.7
	0.5	0	-4.9	-0.4	-1.0	-5.3
	0.5	0	-2.9	-0.6	-0.8	-3.5
	0.5	0	2.1	-0.6	-0.8	1.5
	0.5	0	5.2	-0.5	-2.0	4.7

TABLE II (Continued)

Assumptions Made in the Calculations	Advance Ratio, μ	Twist, θ_1, deg	Shaft Angle, a_s, deg	Flapping, 1st Cosine Harmonic a_{1h}, deg	Flapping, 1st Sine Harmonic b_{1h}, deg	Tip Path Plane Angle of attack, a_{TPP}, deg
Rigid blades, steady aerodynamics and variable inflow with wake distortions	0.3	-8	-4.6	-0.6	1.5	-5.2
	0.3	-8	0.5	-1.3	1.7	-0.8
	0.3	-8	10.7	0.0	3.9	10.7
	0.3	0	-4.7	-0.7	0.3	-5.4
	0.3	0	0.5	-1.2	0.5	-0.7
	0.3	0	10.7	-0.3	3.2	10.4
	0.5	0	-5.0	-0.2	-0.7	-5.2
	0.5	0	2.1	-0.2	1.4	1.9
	0.5	0	5.2	-0.4	1.4	4.8
Rigid blades, unsteady aerodynamics and variable inflow with wake distortions	0.3	-8	-4.6	-0.4	1.5	-5.0
	0.3	-8	0.6	-0.7	1.9	-0.1
	0.3	-8	10.7	-1.2	3.8	9.5
	0.3	0	-4.7	-0.5	0.2	-5.2
	0.3	0	0.5	-1.2	0.6	-0.7
	0.3	0	10.7	-1.4	2.8	9.3
	0.5	0	-5.0	-0.1	-0.6	-5.1
	0.5	0	2.1	-0.5	1.4	1.6
	0.5	0	5.1	-0.9	1.3	4.2
Flexible blades, steady aerodynamics and variable inflow with wake distortions	0.3	-8	-4.6	-0.5	-0.1	-5.1
	0.3	-8	0.5	-1.3	-0.5	-0.8
	0.3	-8	10.7	-1.2	-1.8	9.5
	0.3	0	-4.6	-0.6	-0.4	-5.2
	0.3	0	0.5	-1.2	-0.8	-0.7
	0.3	0	10.7	0.4	-0.2	11.1
	0.5	0	-4.9	-0.5	-1.1	-5.4
	0.5	0	2.1	-0.2	-0.8	1.9
	0.5	0	5.2	0.3	-1.4	5.5

TABLE II (Concluded)

Assumptions Made in the Calculations	Advance Ratio, μ	Twist, θ_1, deg	Shaft Angle, α_s, deg	Flapping, 1st Cosine Harmonic a_{1_h}, deg	Flapping, 1st Sine Harmonic b_{1_h}, deg	Tip Path Plane Angle of attack, α_{TPP}, deg
Flexible blades, unsteady aerodynamics and variable inflow with wake distortions	0.3	-8	-4.6	-0.5	0.0	-5.1
	0.3	-8	0.5	-1.7	0.0	-1.2
	0.3	-8	5.6	-1.5	0.1	4.1
	0.3	-8	10.7	-1.2	-0.3	9.5
	0.3	0	-4.6	-0.6	-0.2	-5.2
	0.3	0	0.5	-1.1	-0.4	-0.6
	0.3	0	5.6	-1.1	-0.3	4.5
	0.3	0	10.7	-1.1	0.0	9.6
	0.5	0	-4.9	-0.4	-0.9	-5.3
	0.5	0	-2.9	-0.7	-0.7	-3.6
	0.5	0	2.1	-0.7	-0.5	1.4
	0.5	0	5.2	-0.7	-1.7	4.5

TABLE III - LIFT, PROPULSIVE FORCE AND TORQUE COEFFICIENT FIGURE NUMBER INDEX

COMPARISON OF THE EFFECT OF:	UNDER THE ASSUMPTIONS OF:	CONTAINED IN FIG. NO.:
Blade Flexibility	Steady aerodynamics and constant inflow	10
	Unsteady aerodynamics and constant inflow	11
	Steady aerodynamics and variable inflow without wake distortions	12
	Unsteady aerodynamics and variable inflow with wake distortions	13
Unsteady Aerodynamics	Rigid blades and constant inflow	14
	Flexible blades and constant inflow	15
	Rigid blades and variable inflow with wake distortions	16
	Flexible blades and variable inflow with wake distortions	17
Variable inflow without wake distortions	Rigid blades and steady aerodynamics	18
	Flexible blades and unsteady aerodynamics	19
Wake Distortions	Rigid blades and steady aerodynamics	20
	Flexible blades and unsteady aerodynamics	21
Variable Inflow with wake Distortions	Rigid blades and steady aerodynamics	22
	Flexible blades and steady aerodynamics	23
	Rigid blades and unsteady aerodynamics	24
	Flexible blades and unsteady aerodynamics	25

$\theta_1 = 0°$ $\theta_{75} = 8°$ $\mu = 0.5$ $M_{1,90} = 0.82$

CLASSICAL THEORY (REF. 1)
○   EXP. (REF. 7, a_C CORRECTED FOR INTERFERENCE EFFECTS)
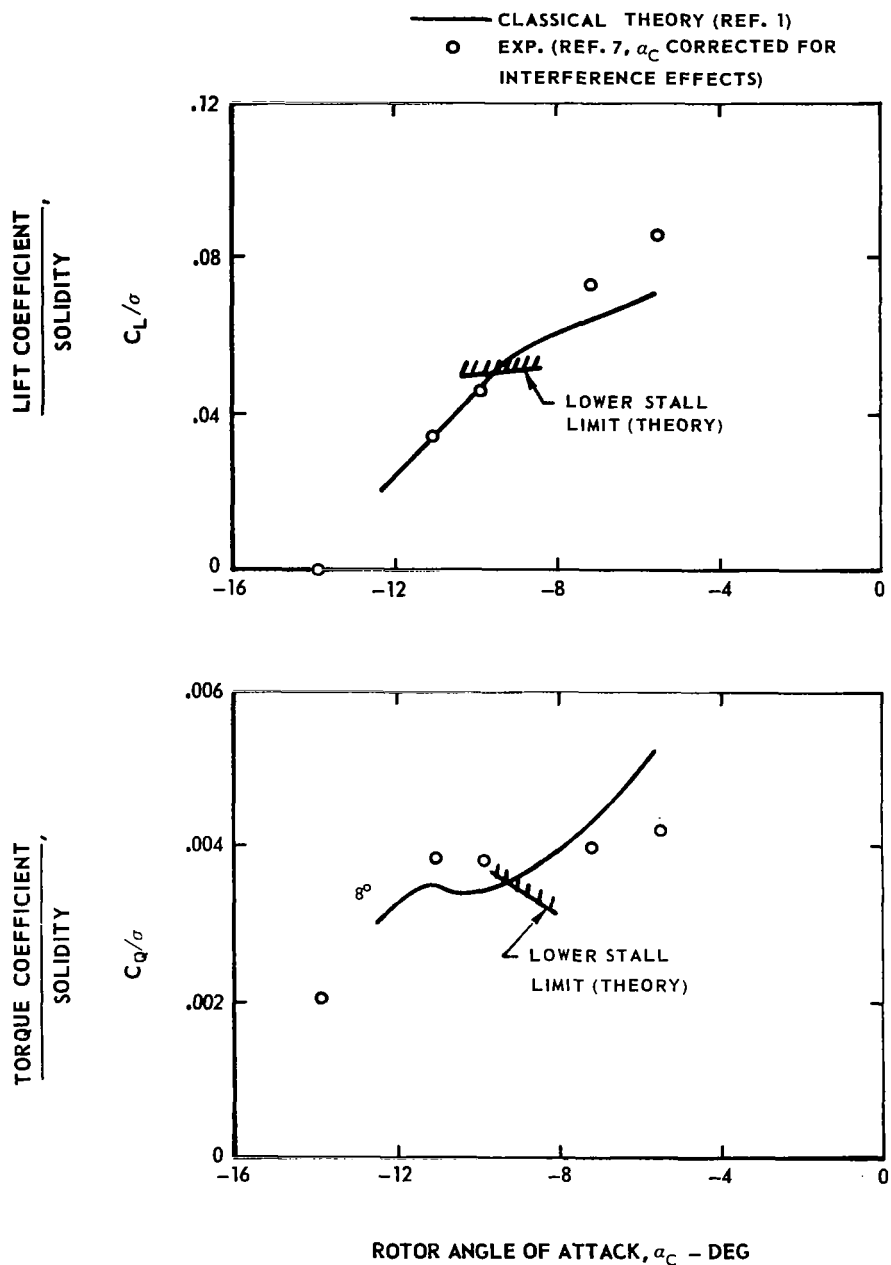
Figure 1.—Comparison of typical theoretical and experimental performance characteristics.

37

$C_L / \sigma \approx 0$

$a_{1_h} = b_{1_h} = 0$ DEG

$\theta_{75} = 0$ DEG

$\theta_1 = 0$ DEG

$a_s = 0$ DEG

CORRECTION CURVE

LONGITUDINAL CYCLIC ANGLE, ΔA_{1_s} – DEG

LATERAL CYCLIC ANGLE, ΔB_{1_s} – DEG

WIND TUNNEL VELOCITY, V – KNOTS
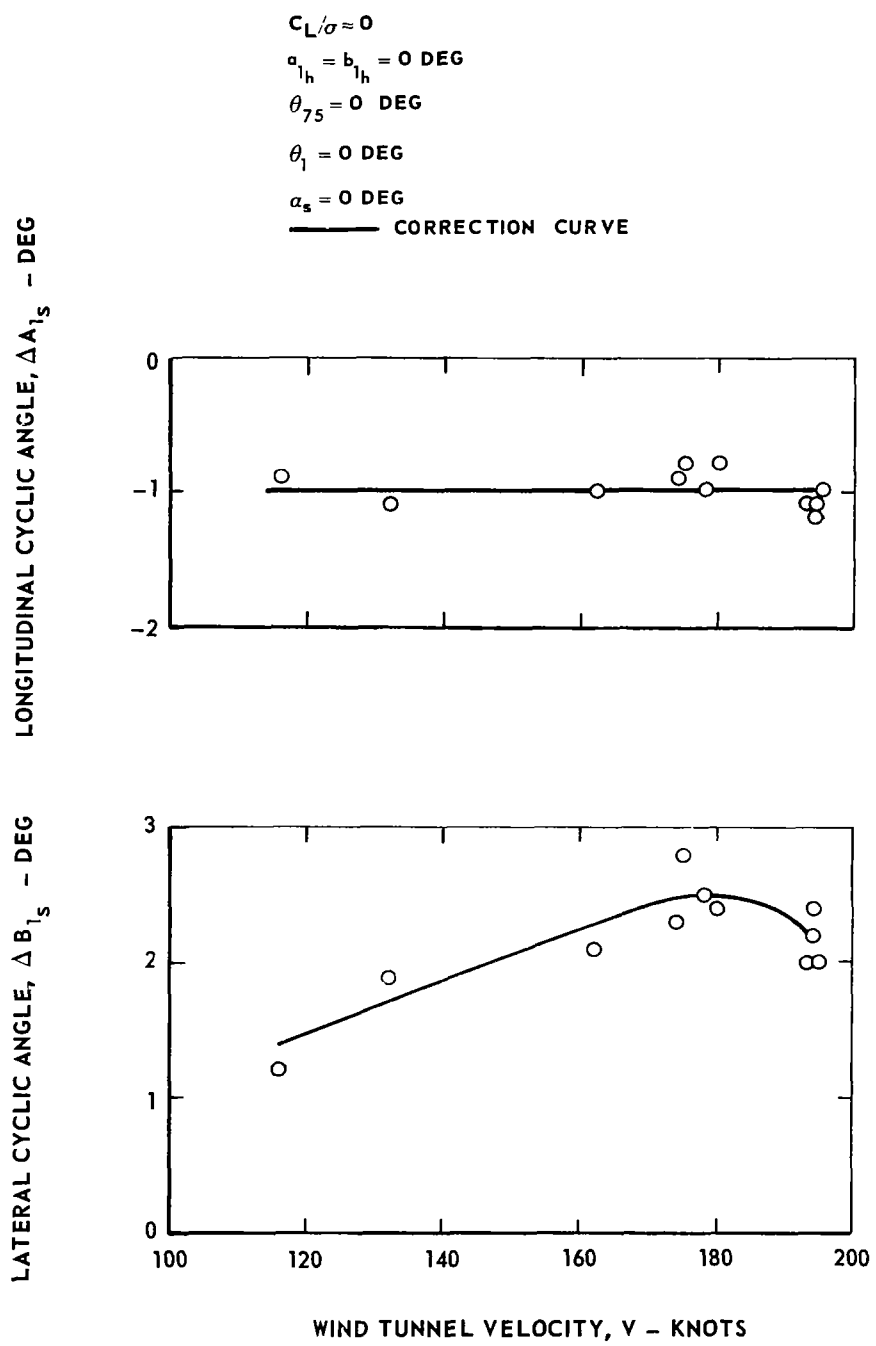
- Figure 2.– Experimental cyclic pitch inputs to eliminate first harmonic flapping at zero lift.

UNSTEADY 2–D
AIRFOIL DATA

a, a_{OL}, a_{max}, u
AS FUNCTIONS
OF A & B

NONDISTORTED
WAKE GEOMETRY

STEADY 2–D
AIRFOIL DATA

SCALING PROCEDURES

CONTROL
ANGLES

BLADE DATA

CONSTANT
INDUCED
VELOCITY

| BLADE RESPONSE PROGRAM |

SECTION OPERATING
CONDITIONS (a, A, B)

| CIRCULATION PROGRAM |

CIRCULATIONS

| DISTORTED WAKE GEOMETRY |

WAKE
GEOMETRY

INDUCED VELOCITIES

PERTINENT OUTPUT:
INTEGRATED ROTOR FORCES
BLADE MOTIONS AND STRESSES
BLADE ROOT PITCHING MOMENT

Figure 3.– UAC rotor analysis.

NORMAL FORCE COEFFICIENT , c_n

PITCHING MOMENT COEFFICIENT, $c_{m_c/4}$
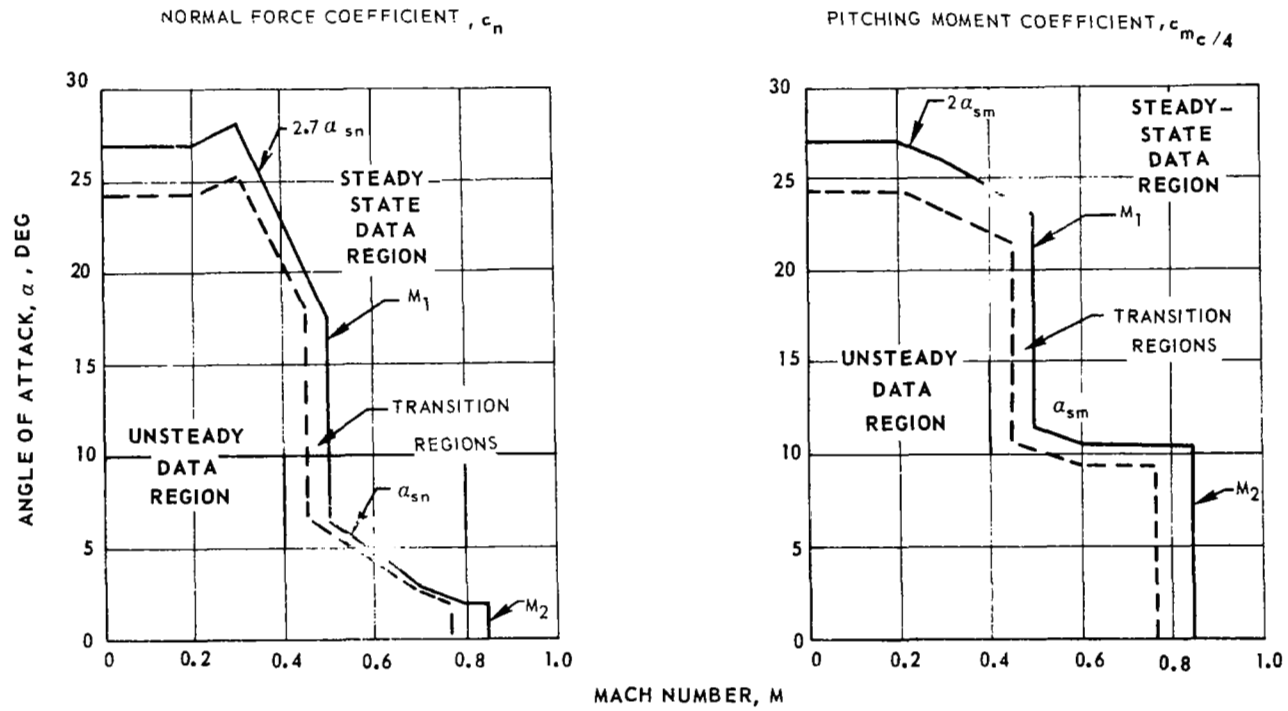
Figure 4.—Parameters defining regions in which scaled unsteady aerodynamics are used.

NACA 0012 $B' = \left(\dfrac{c}{2}\right)^2 \dfrac{\ddot{a}}{U^2} = 0$ $M = 0.2$
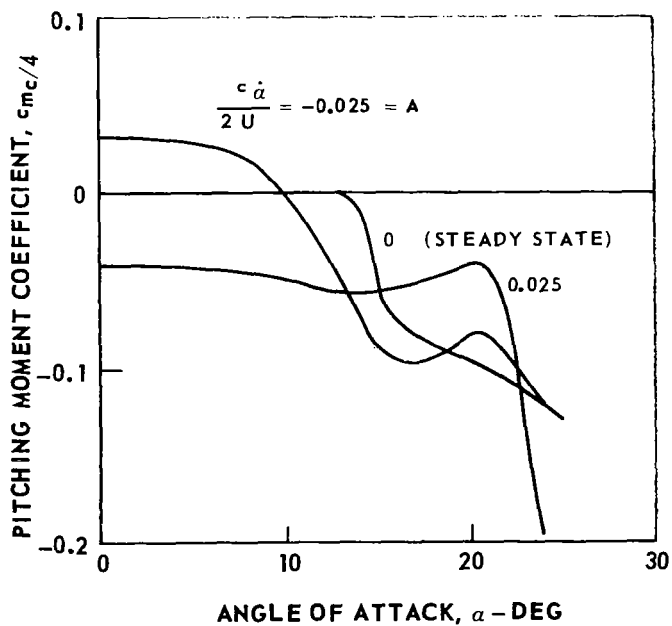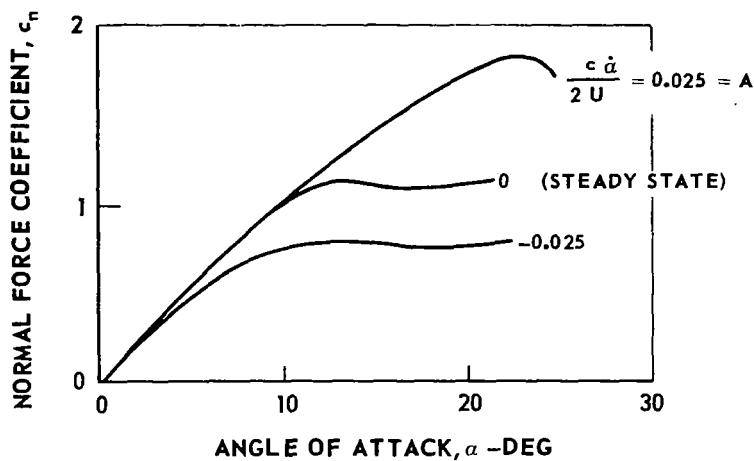
Figure 5.—Sample of generalized unsteady data.

MACH NO. RANGE = 0.3 TO 0.75
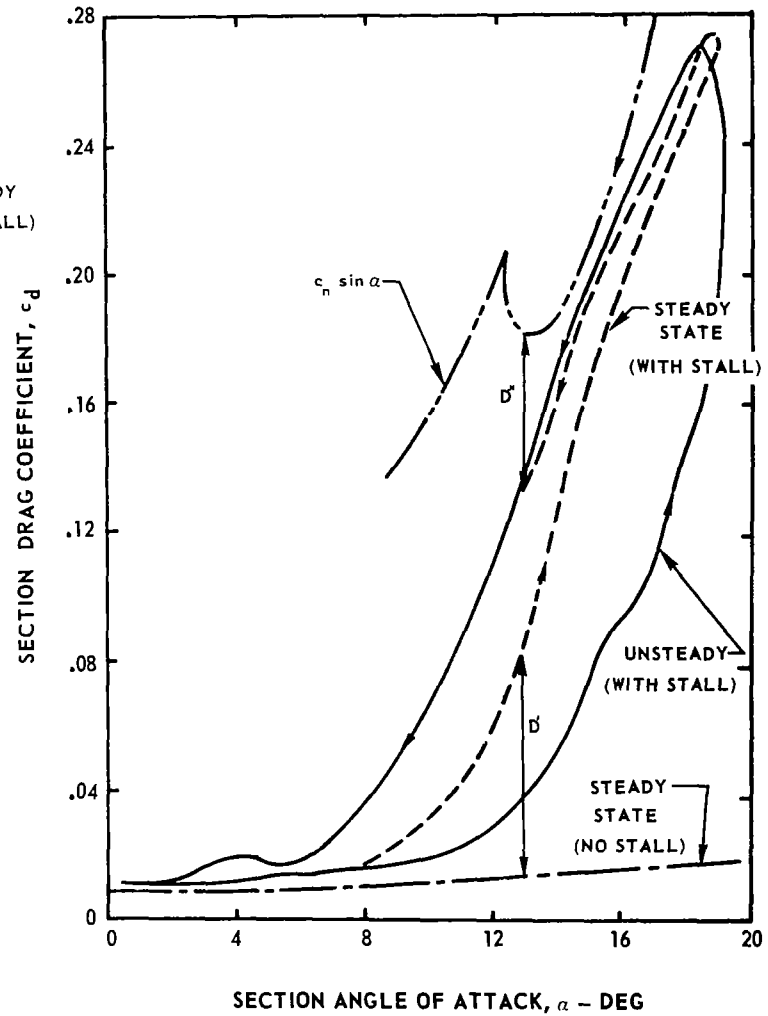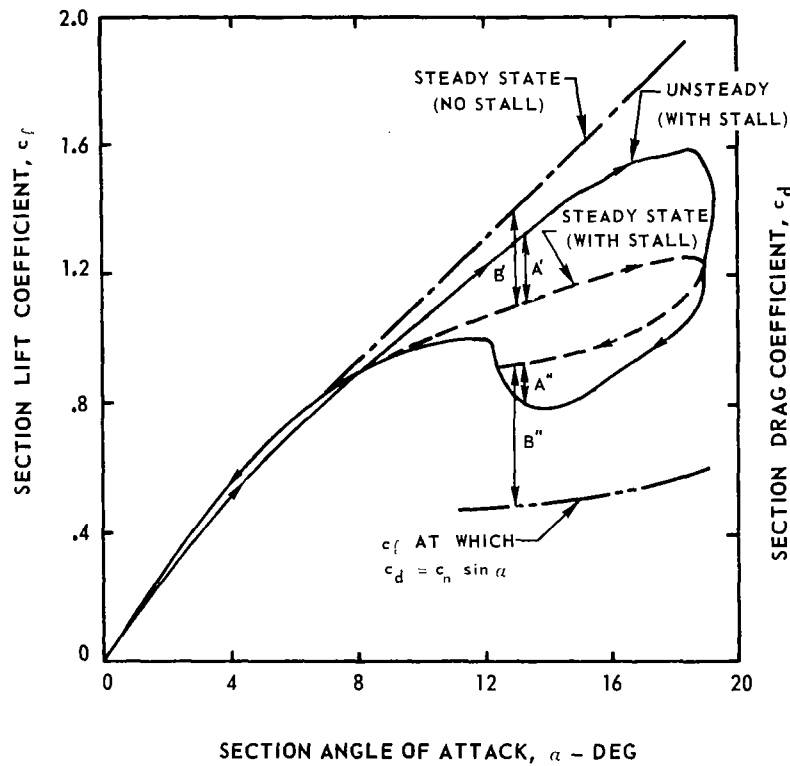
Figure 6.—Airfoil characteristics under steady and unsteady conditions.

Legend:

——————— $c_n \sin \alpha$

— — — — c_d STATIC (MEASURED)

——·——·— $c_{d_{NO\ STALL}}$ (EXTRAPOLATION FROM UNSTALLED REGION)

Left plot:

LIFT COEFFICIENT, $c_\ell \sim c_n$

NO STALL (POTENTIAL FLOW)

$\bar{A}(\alpha)$

$\bar{B}$

α_{st}

$(c_d = c_n \sin \alpha$

FOR $\alpha > \alpha_{st})$

SECTION ANGLE OF ATTACK, α

Right plot:

DRAG COEFFICIENT, c_d

$c_n \sin \alpha$

$\bar{D}$

$\bar{C}(\alpha)$

α_{st}

SECTION ANGLE OF ATTACK, α
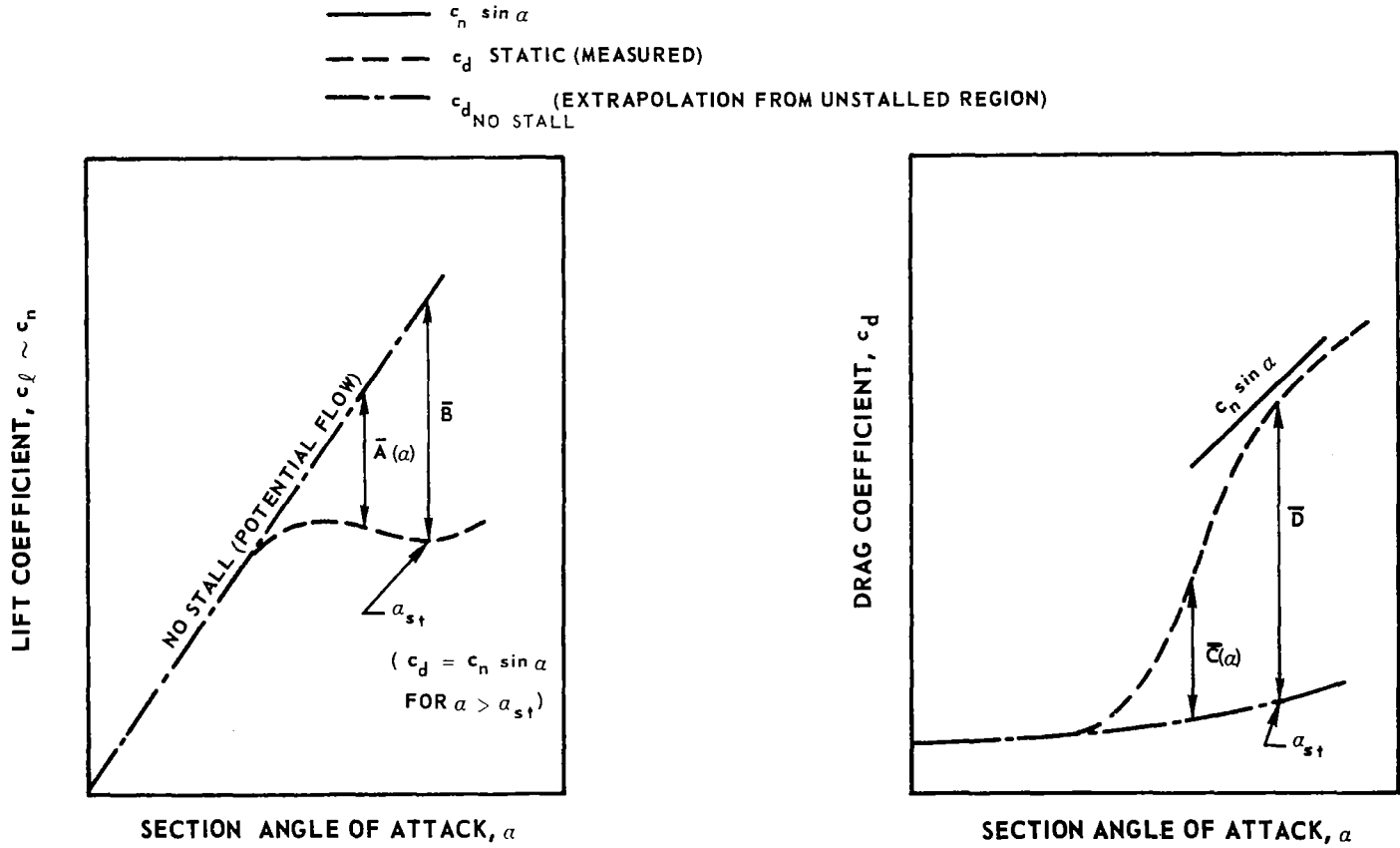
$$c_d = c_{d_{NS}} + (\frac{\bar{C}}{\bar{D}})\,\bar{D} = c_{d_{NS}} + (\frac{\bar{A}}{\bar{B}})\,\bar{D}$$

Figure 7.- Illustration of use of steady-state lift characteristics to estimate steady-state drag.
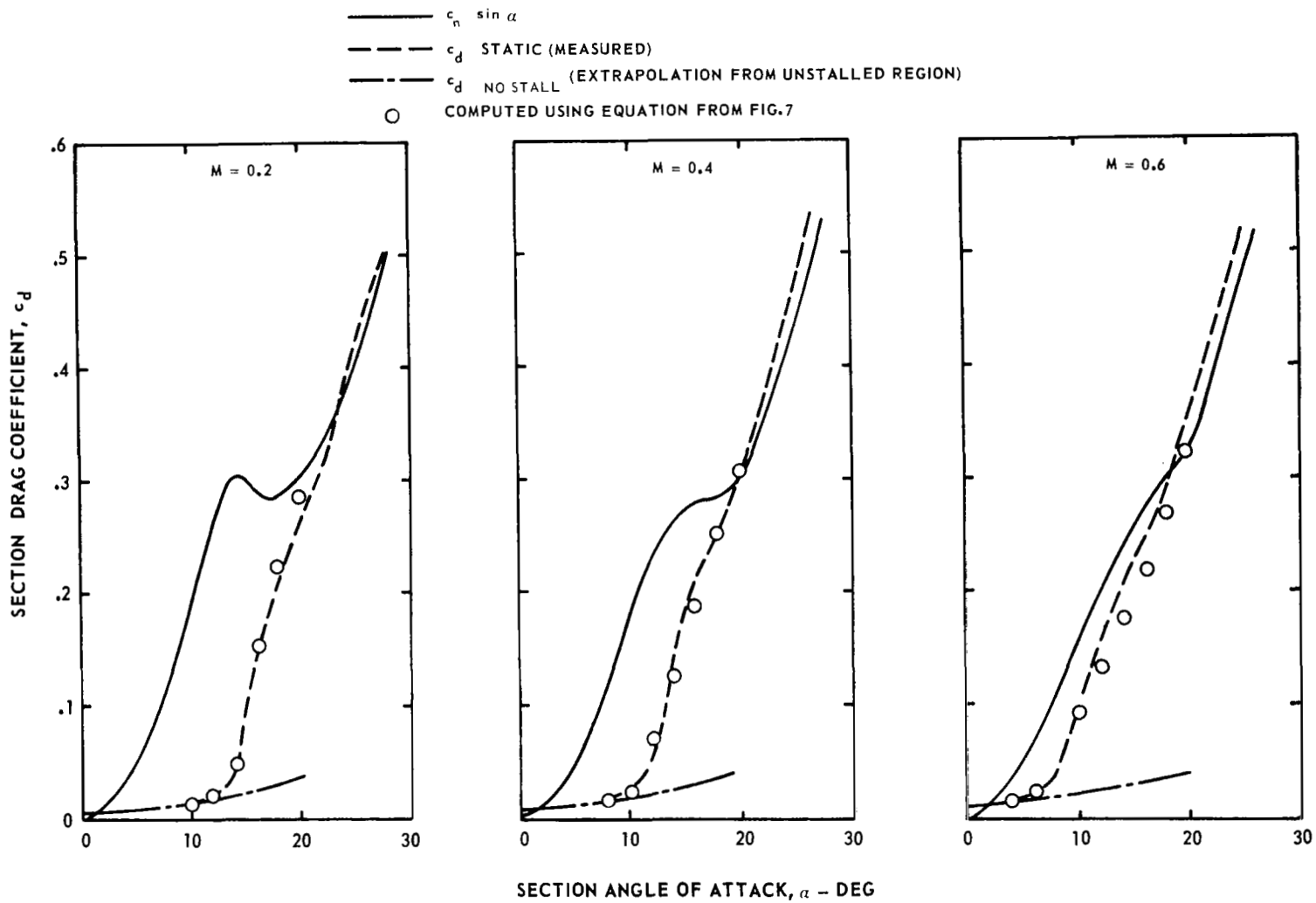
Figure 8.—Comparison of measured and computed steady–state drag.
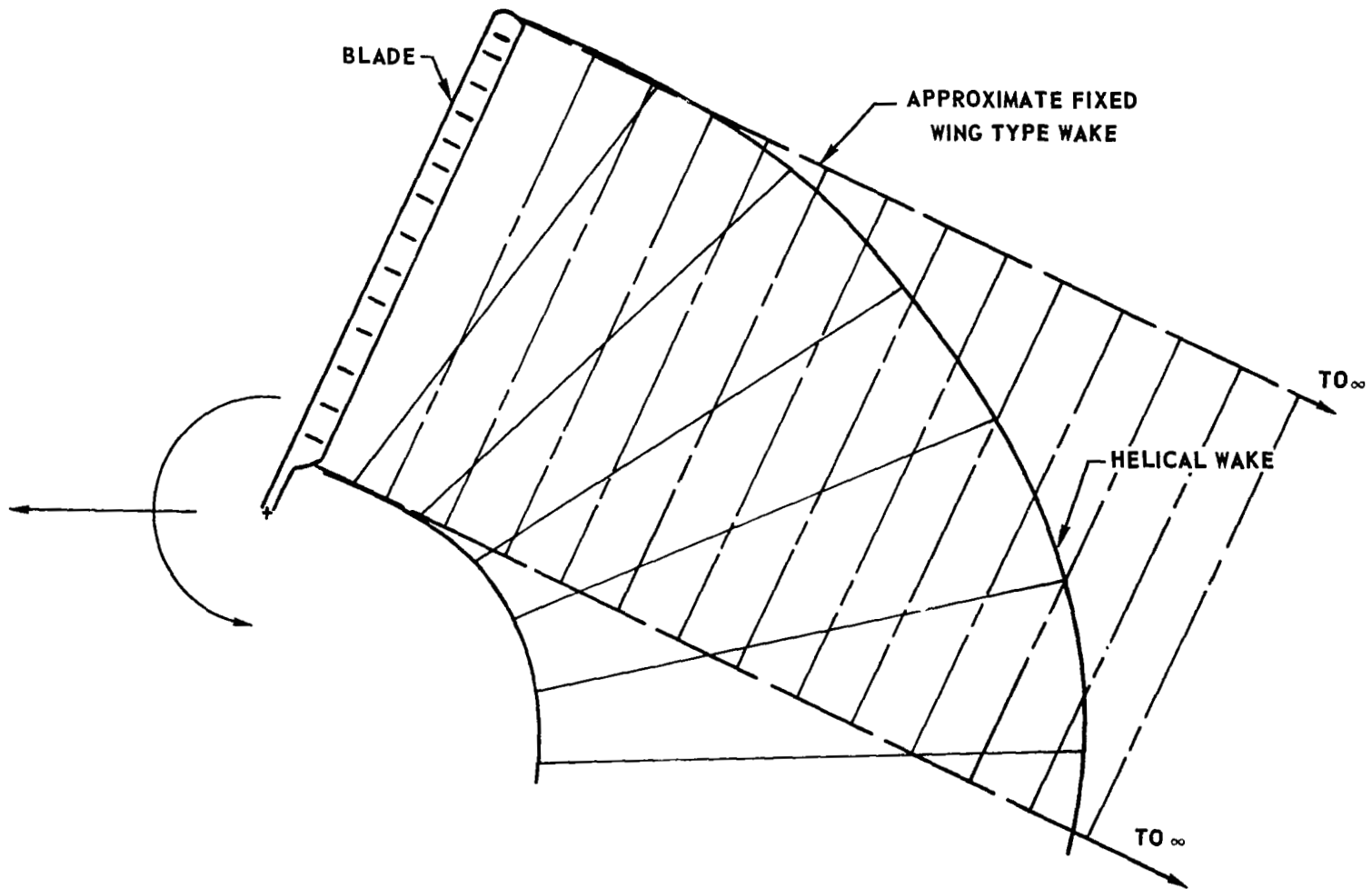
Figure 9.– Schematic blade wake geometry approximation.
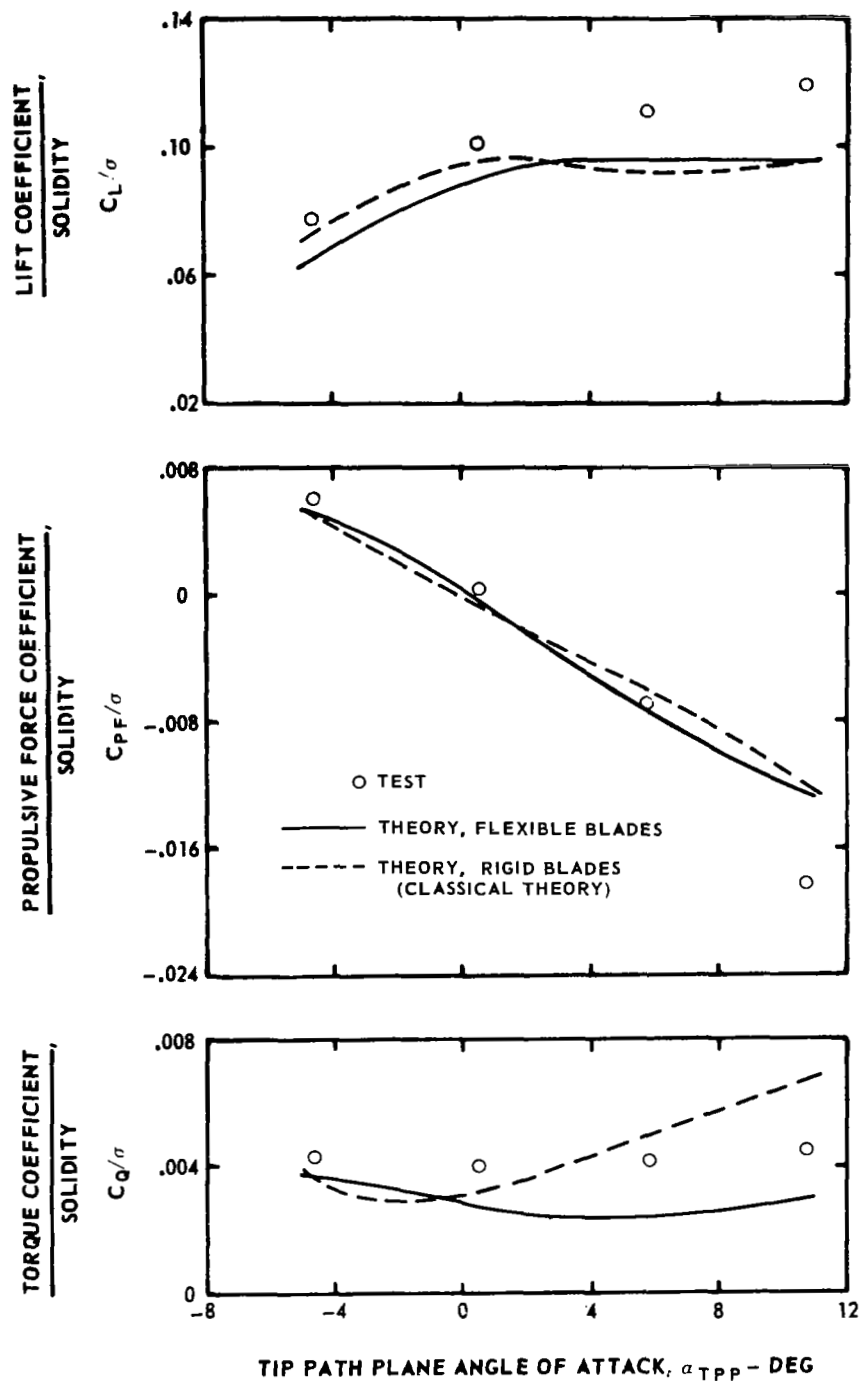
(a) Twist = −8 deg, advance ratio = 0.3

Figure 10.— Effect of blade flexibility on rotor performance with steady aerodynamics and constant inflow.
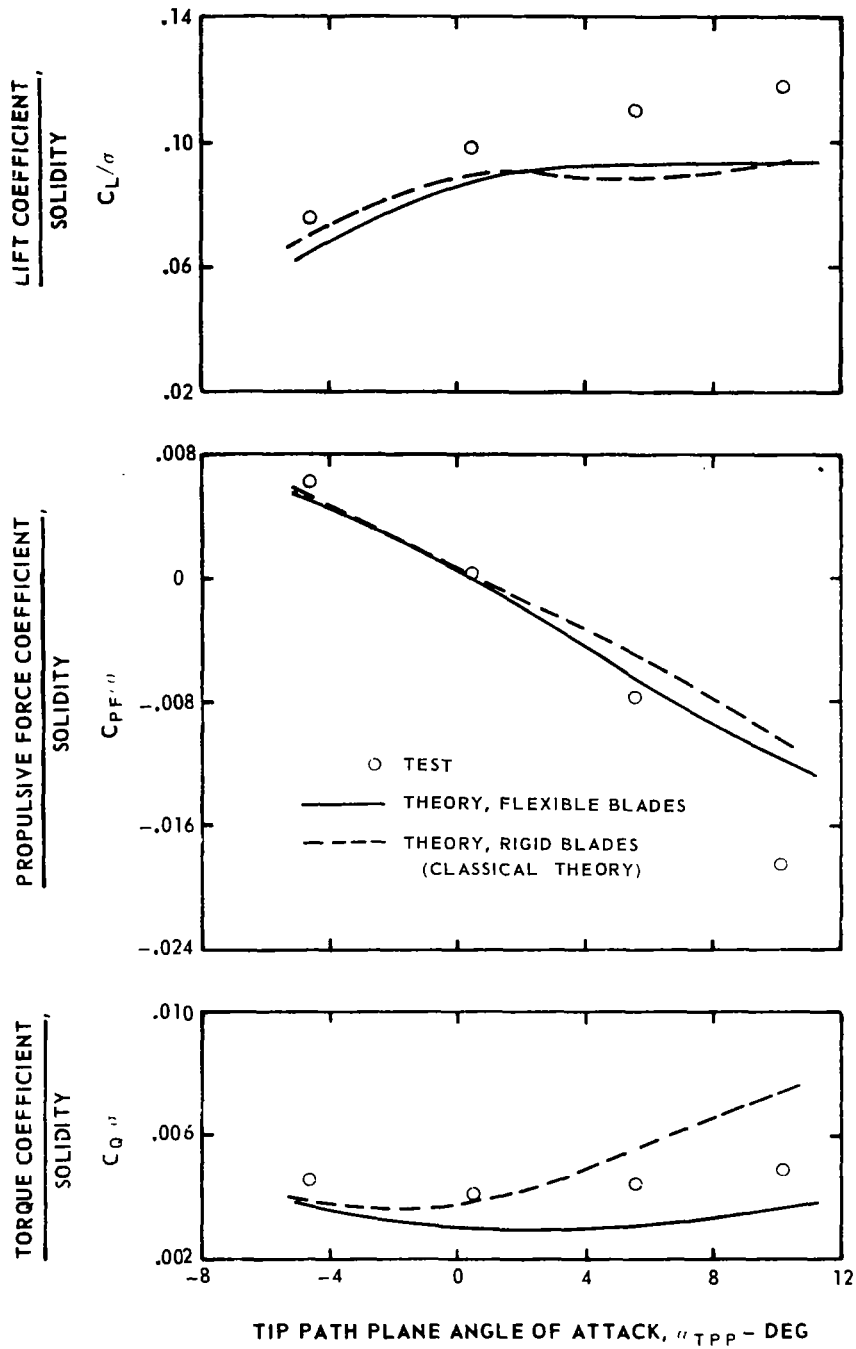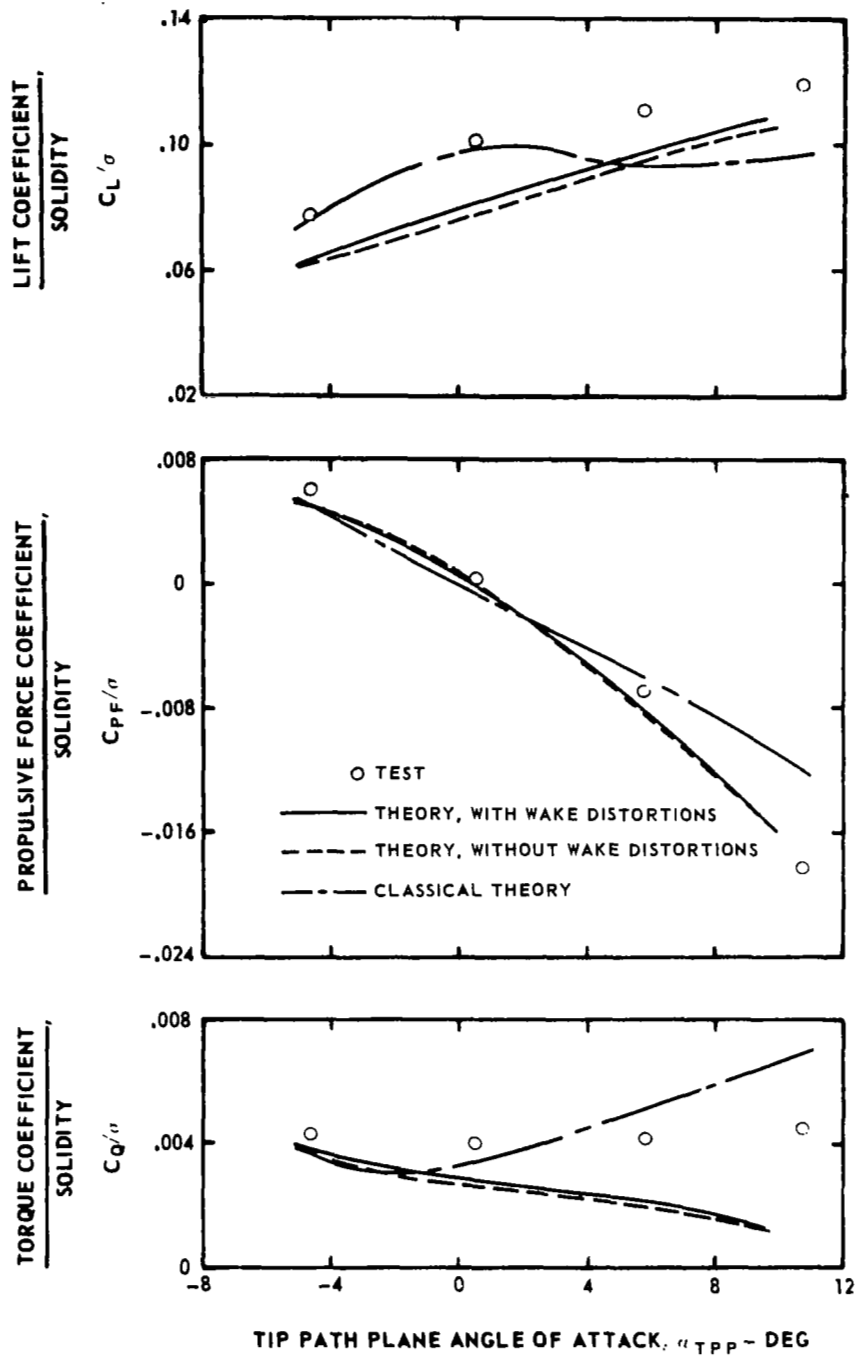
(b) Twist = 0 deg, advance ratio = 0.3

Figure 10. — Continued
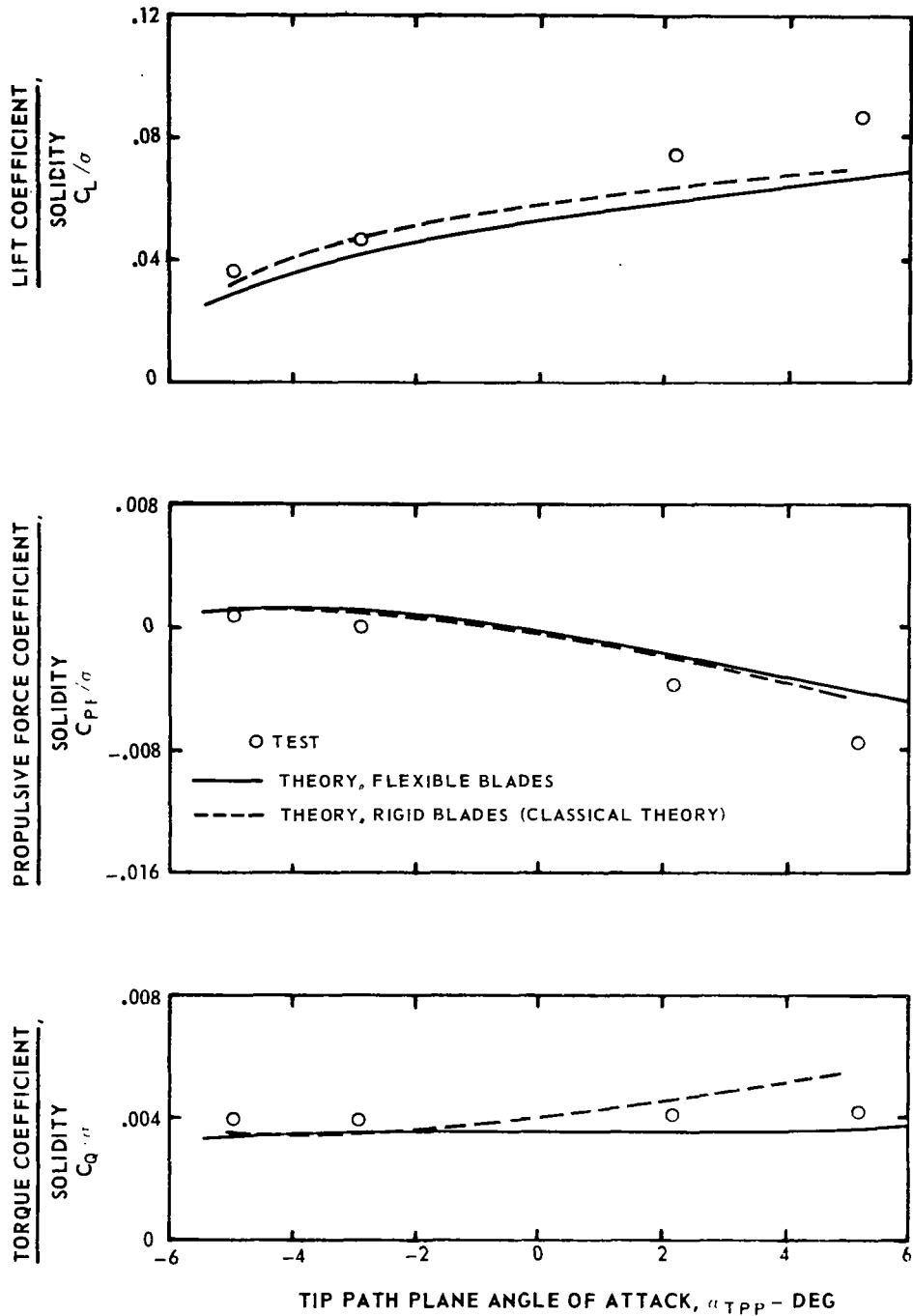
(c) Twist = 0 deg, advance ratio ≈0.5

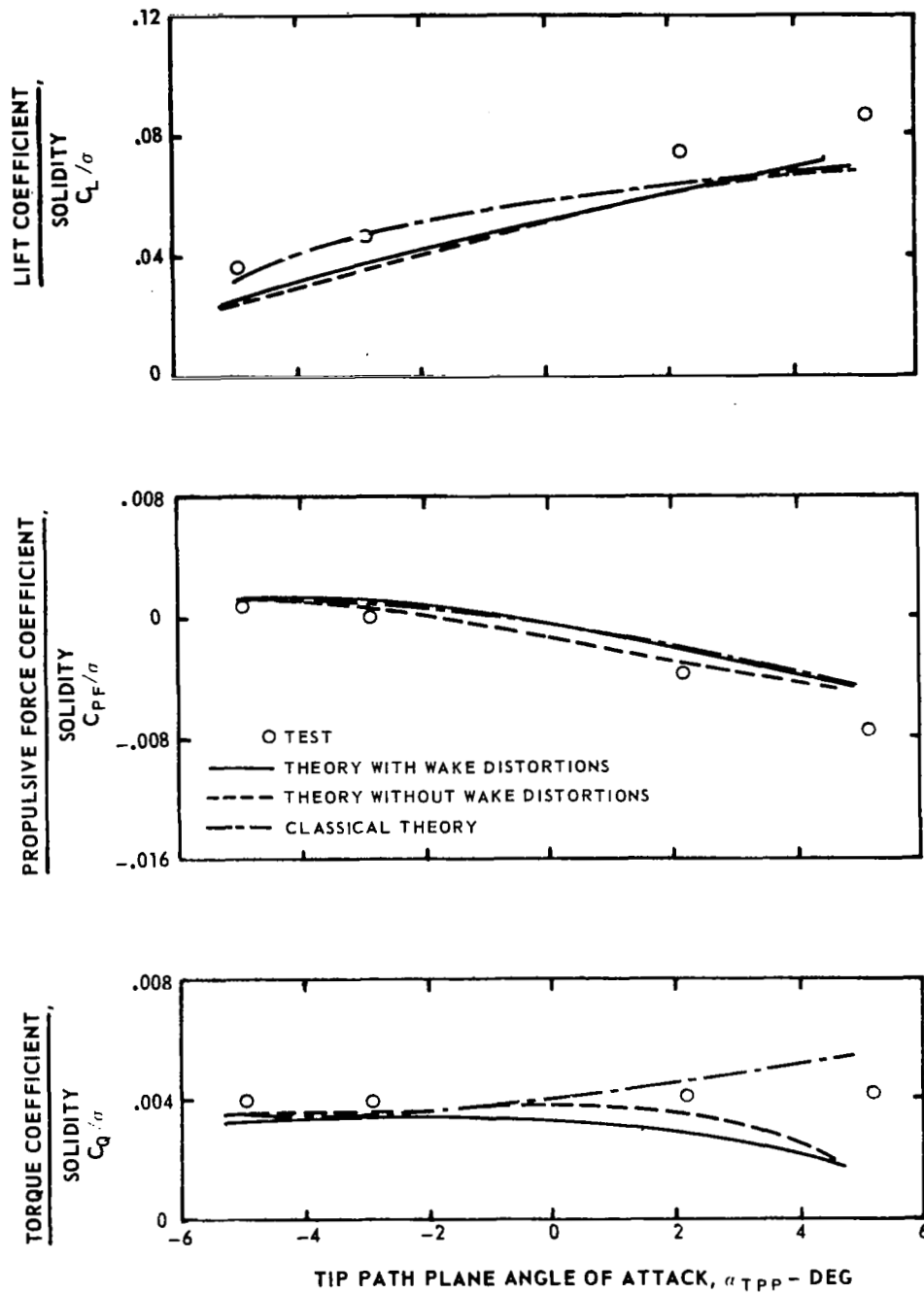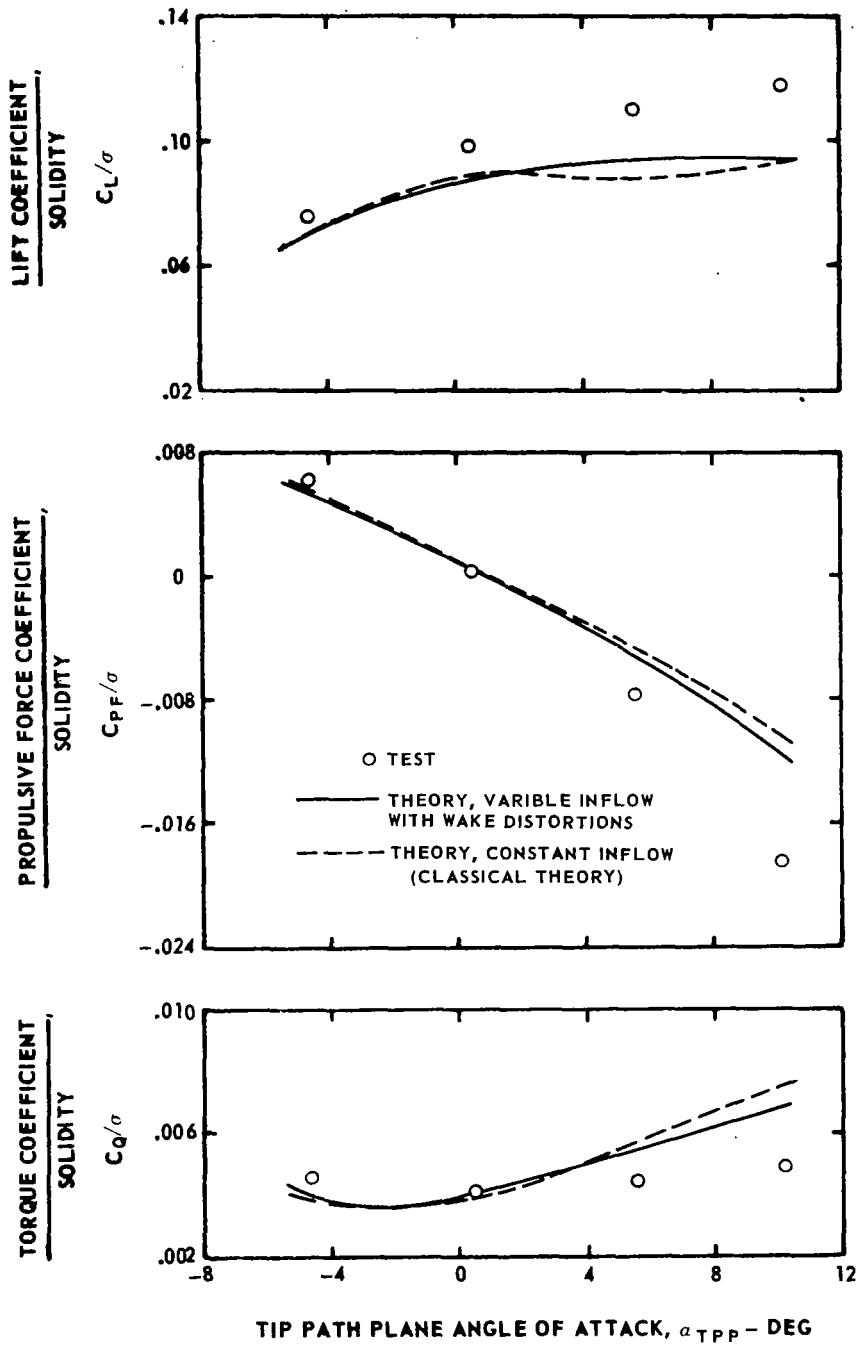Figure 10. — Concluded.
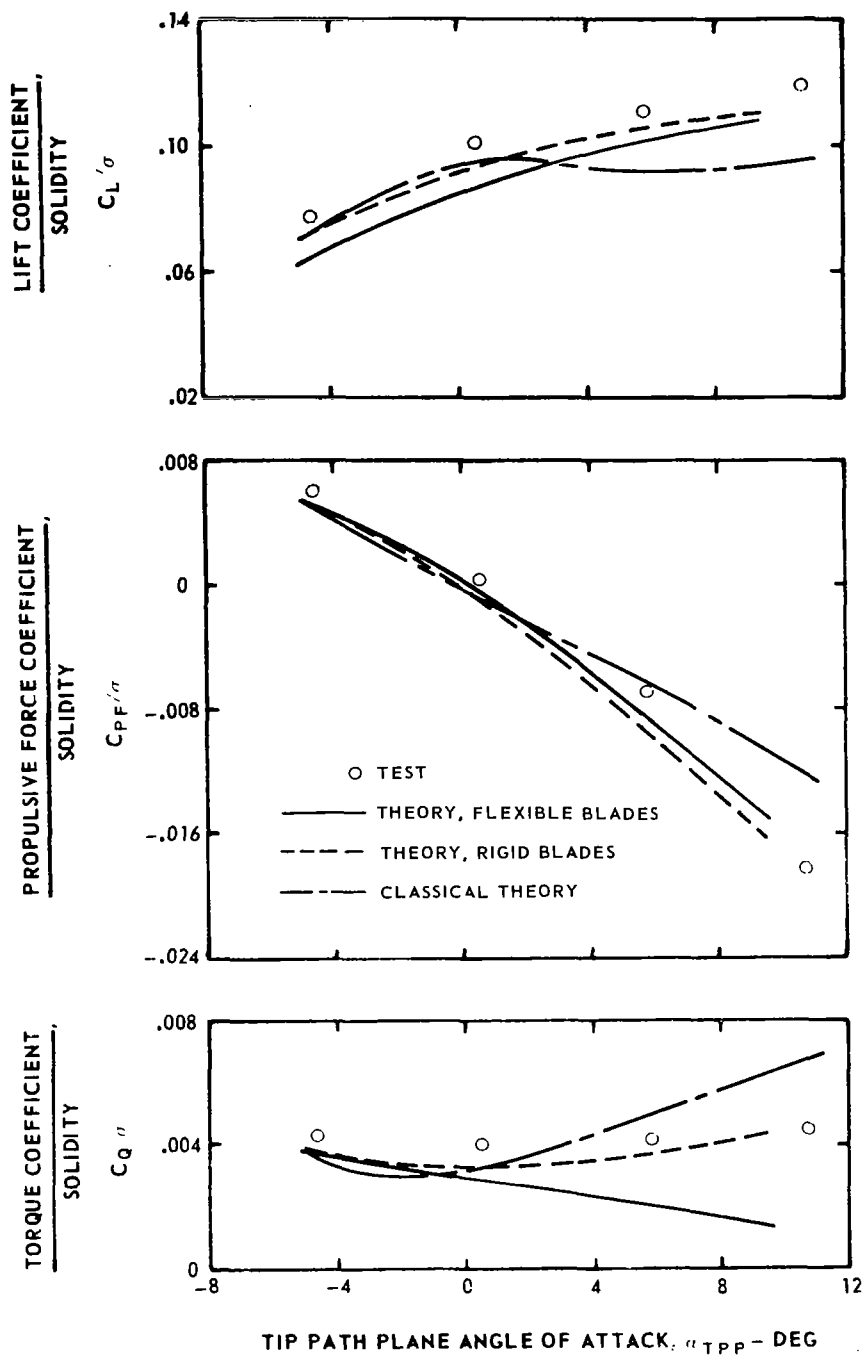
(a) Twist ≈ −8 deg, advance ratio = 0.3

Figure 11.—Effect of blade flexibility on rotor performance with unsteady aerodynamics and constant inflow.
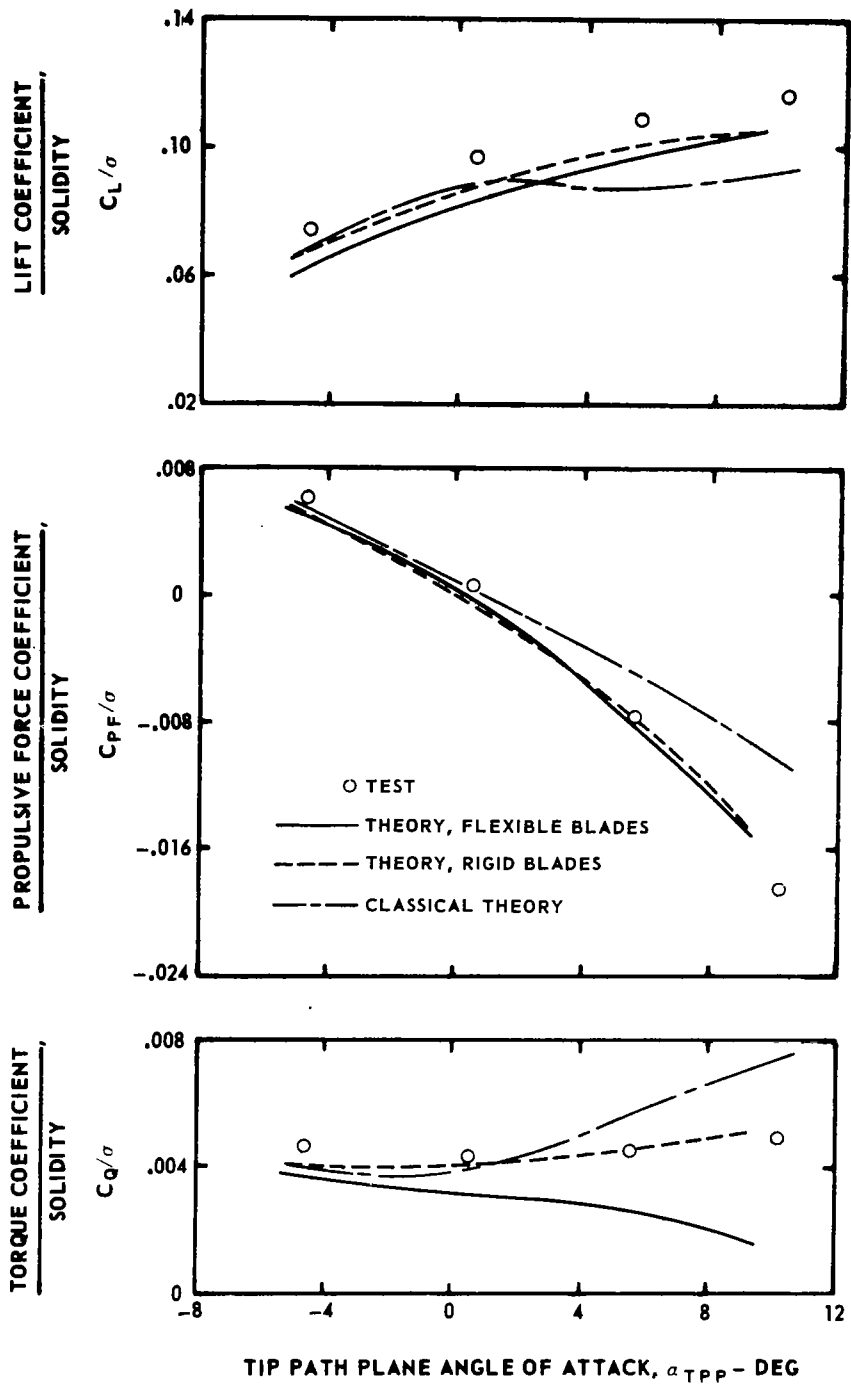
(b) Twist = 0 deg, advance ratio = 0.3

Figure 11. — Continued.
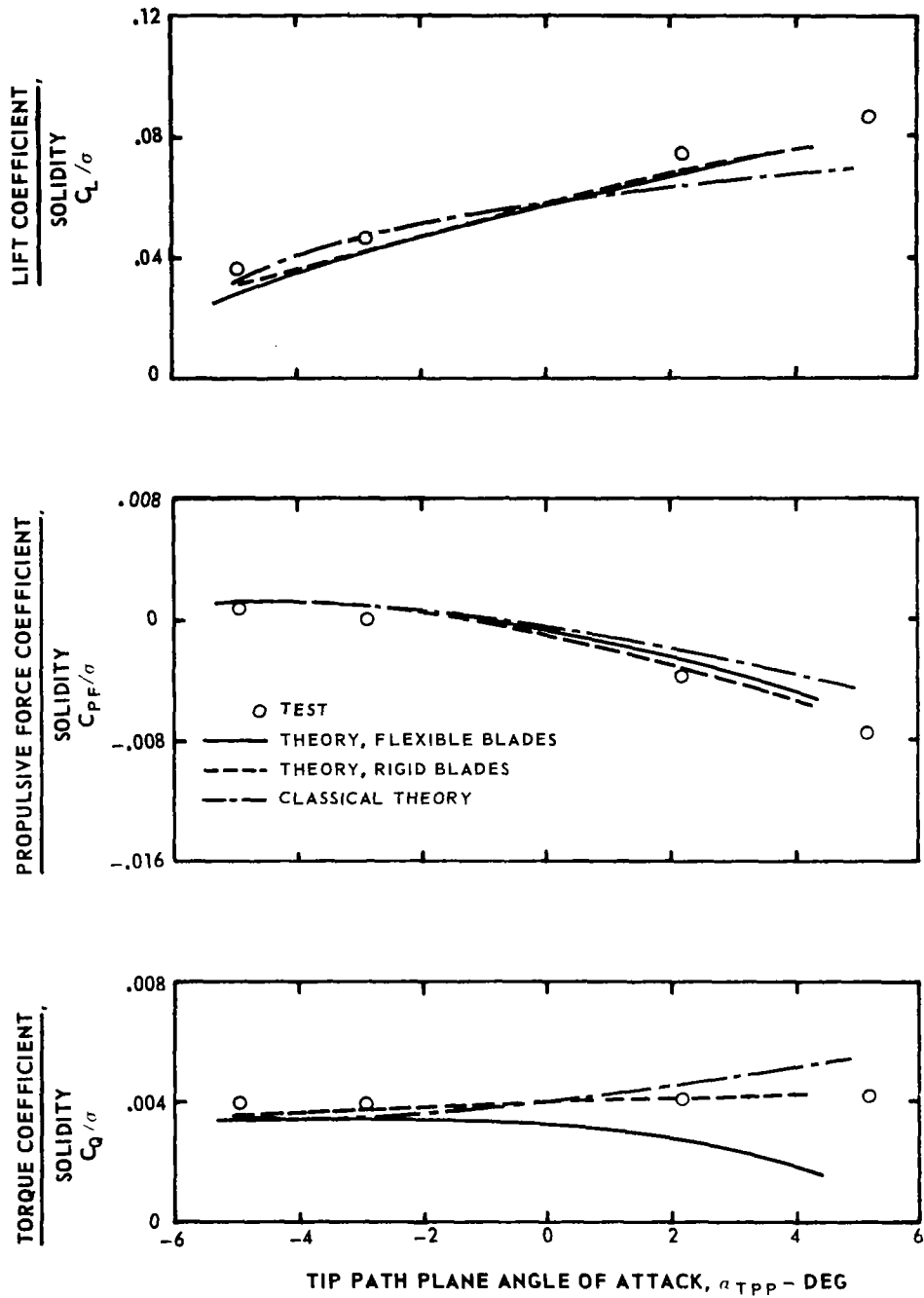
(c) Twist = 0 deg, advance ratio = 0.5

Figure 11. — Concluded.
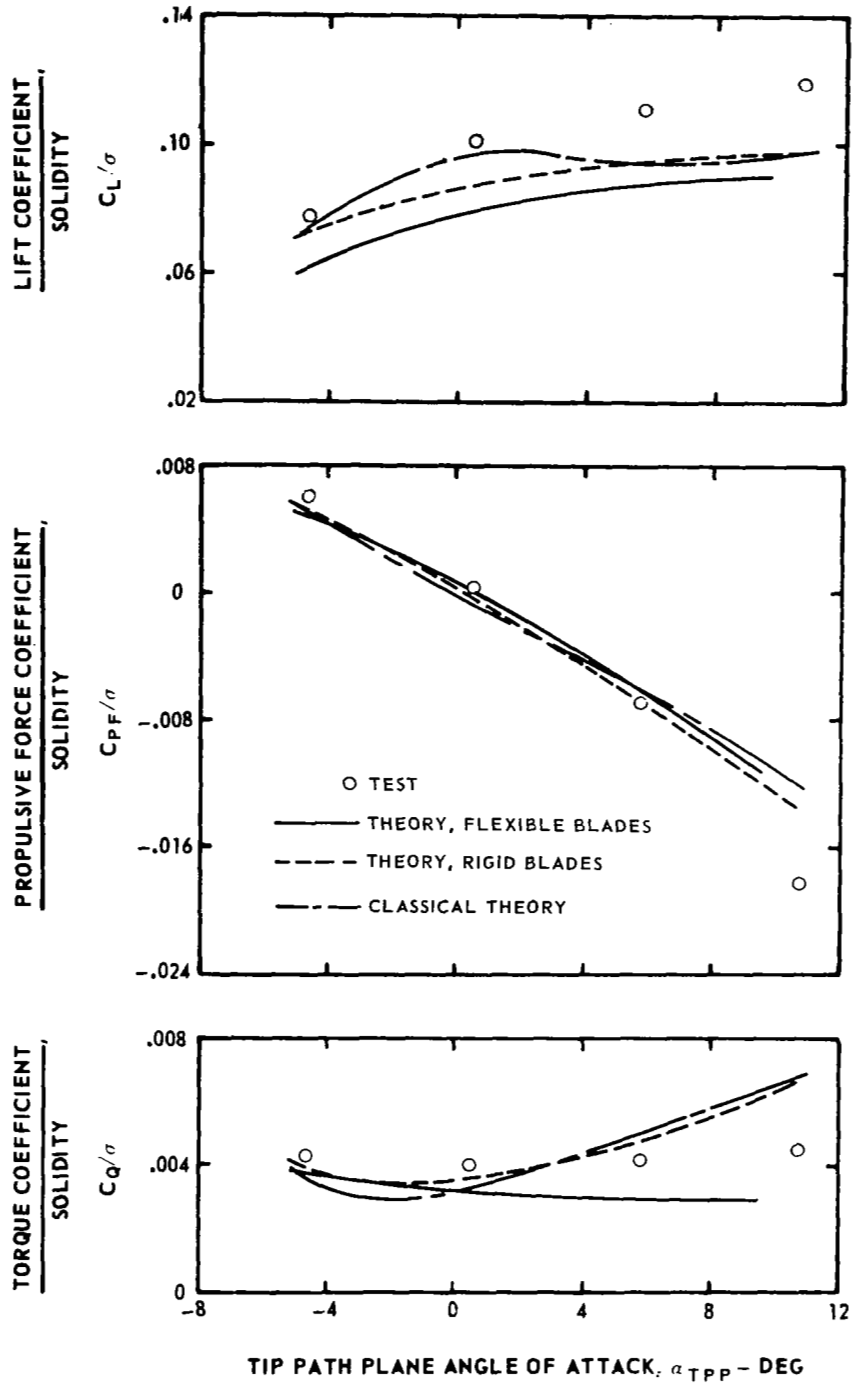
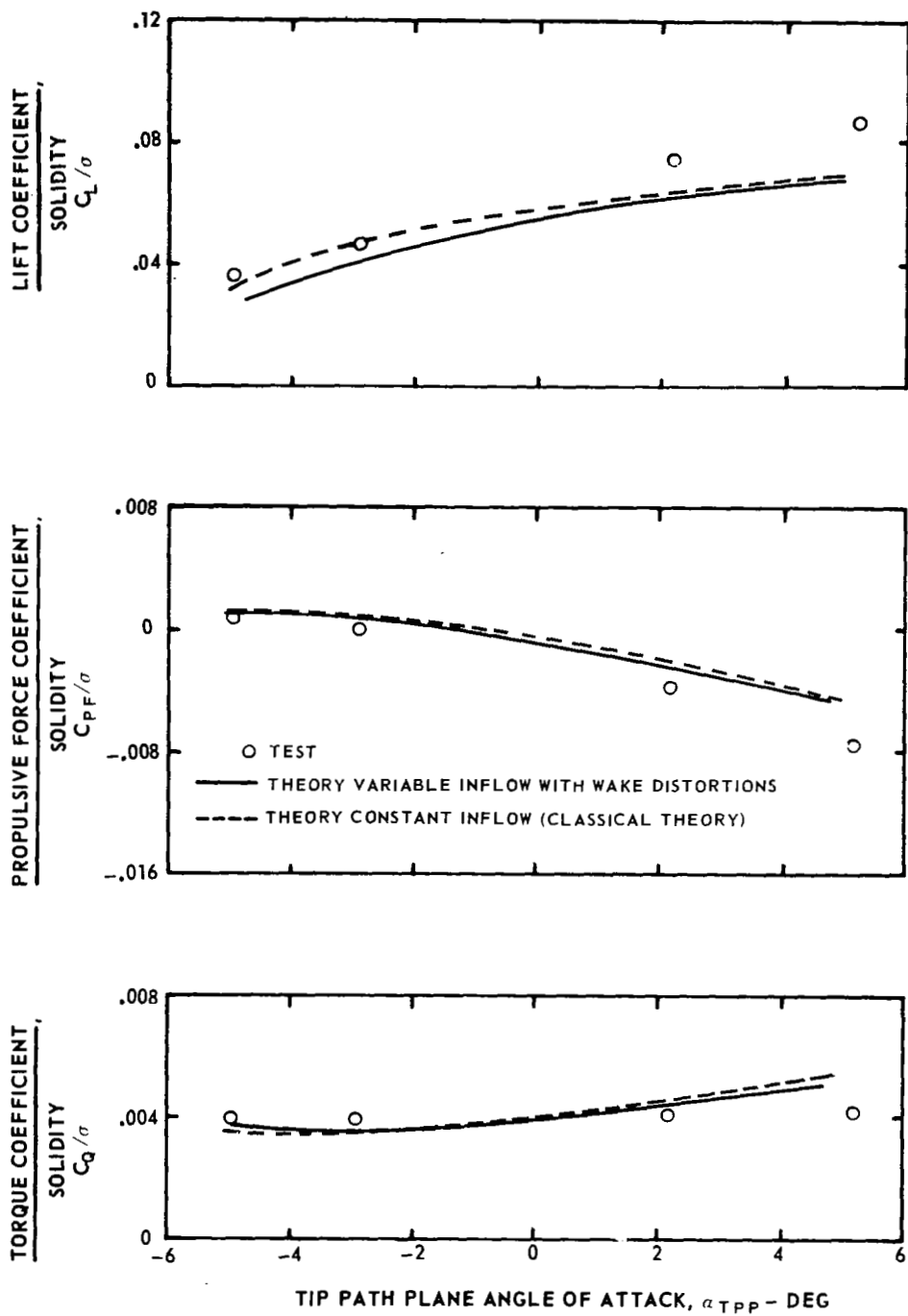(a) Twist = − 8 deg, advance ratio = 0.3

Figure 12.—Effect of blade flexibility on rotor performance with steady aerodynamics and variable inflow with wake distortions.
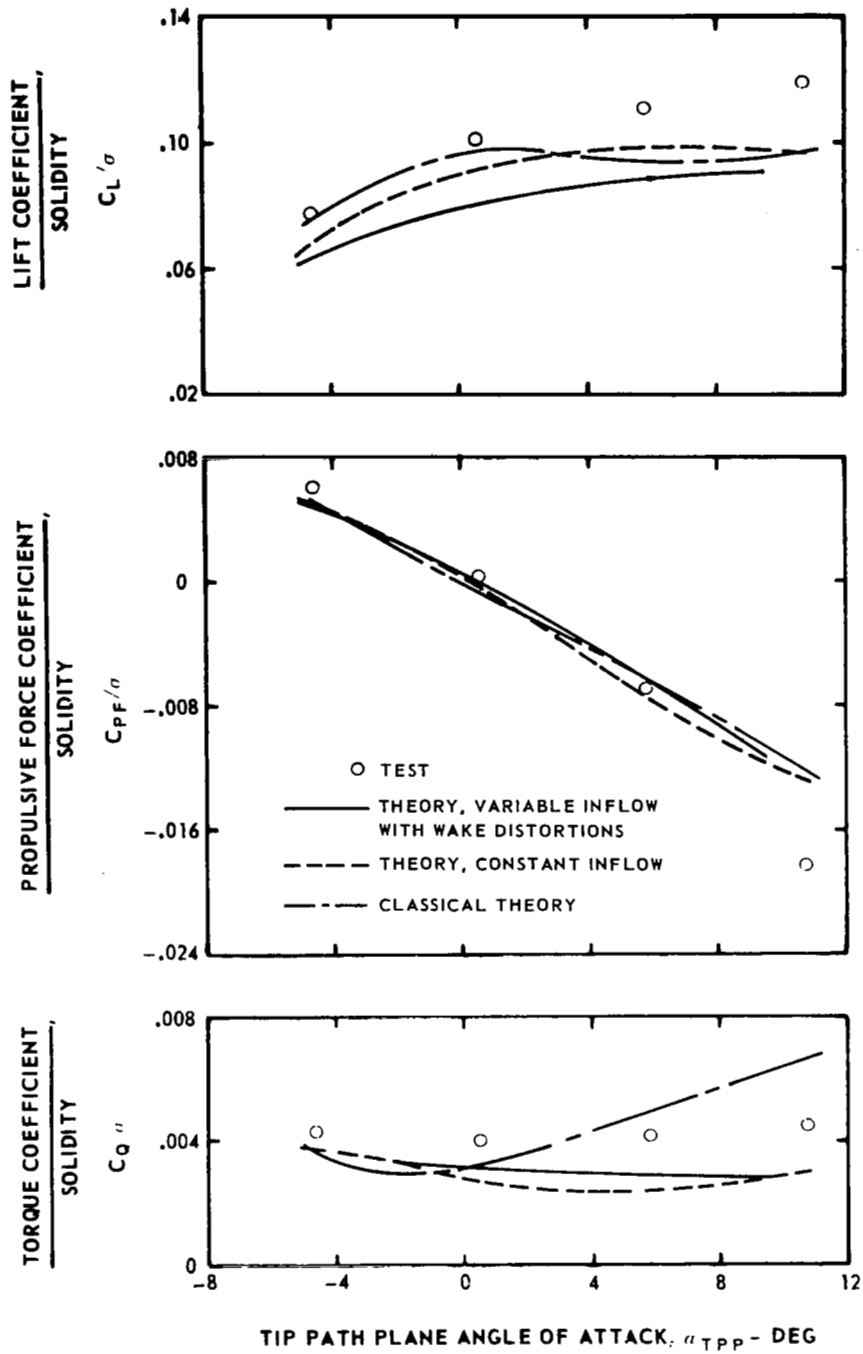
52
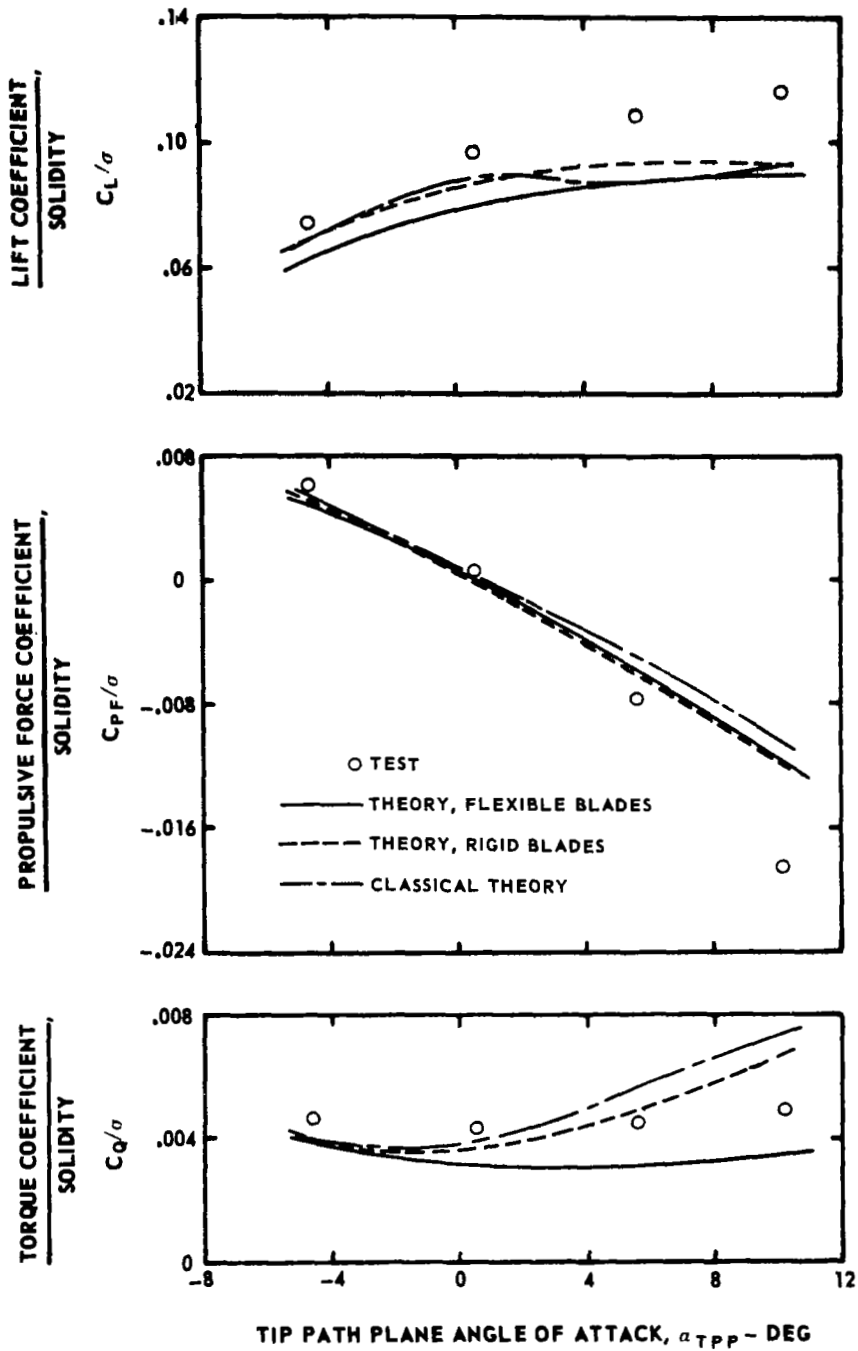
(b) Twist = 0 deg, advance ratio = 0.3

Figure 12. – Continued.

53
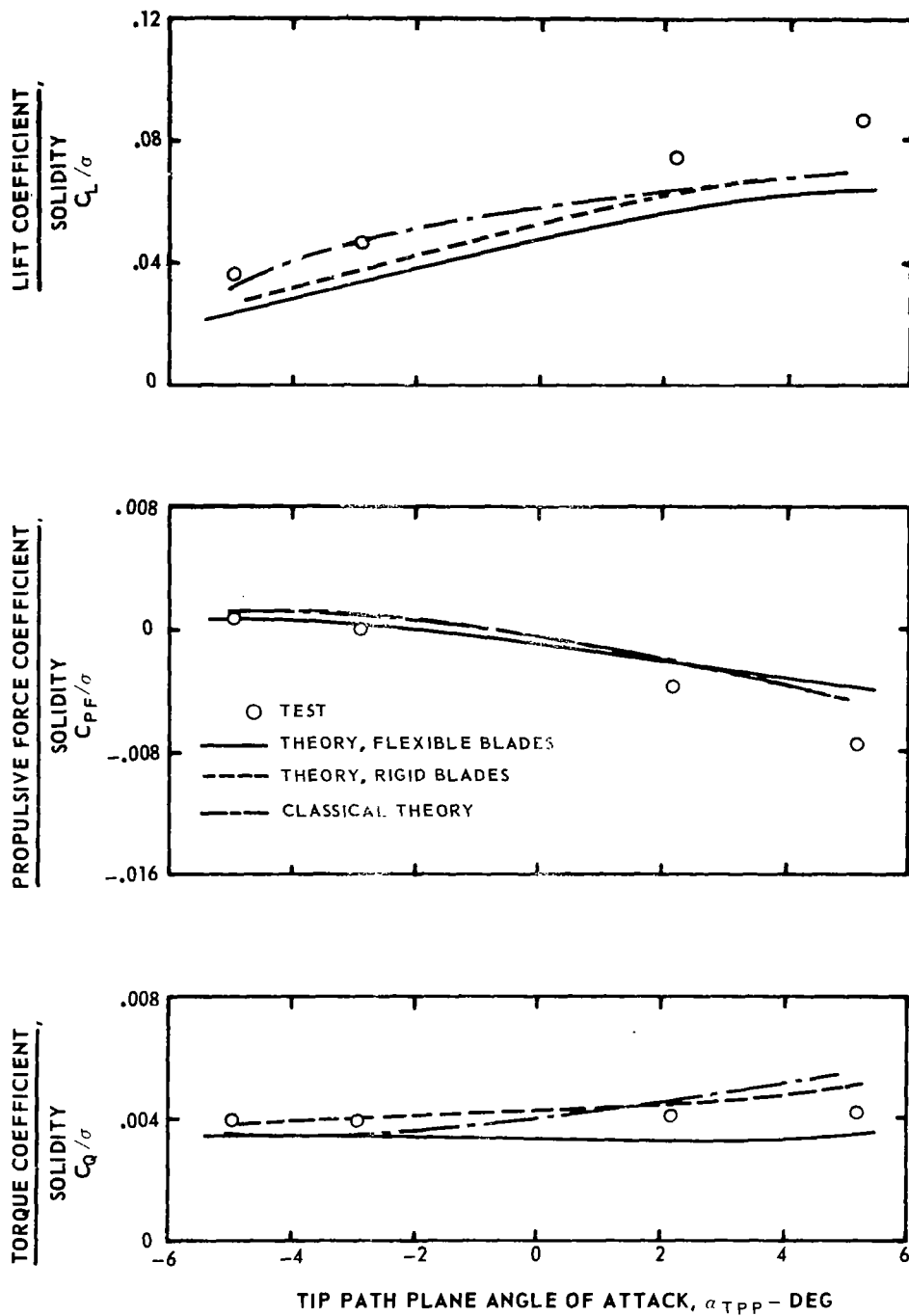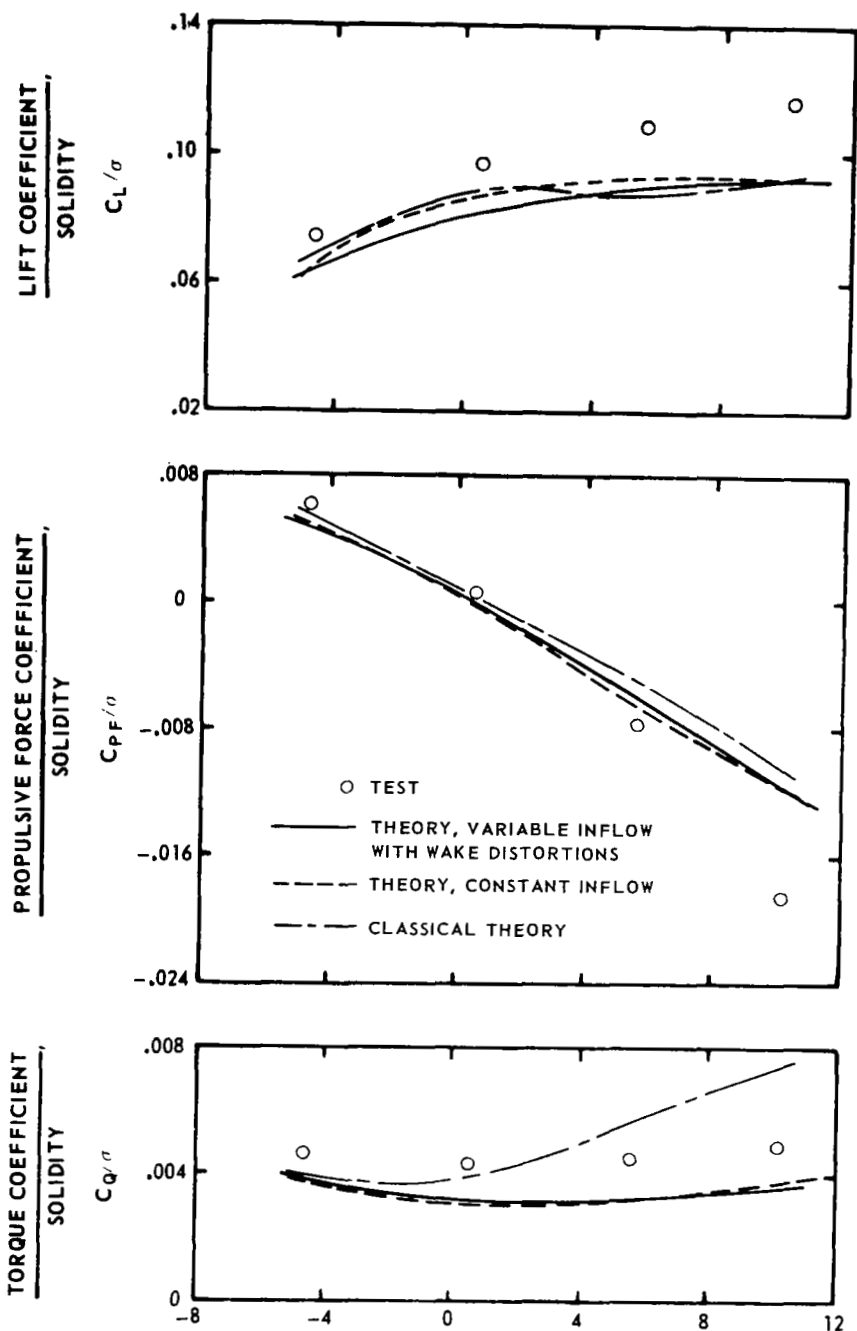
(c) Twist = 0 deg, advance ratio = 0.5

Figure 12. – Concluded.
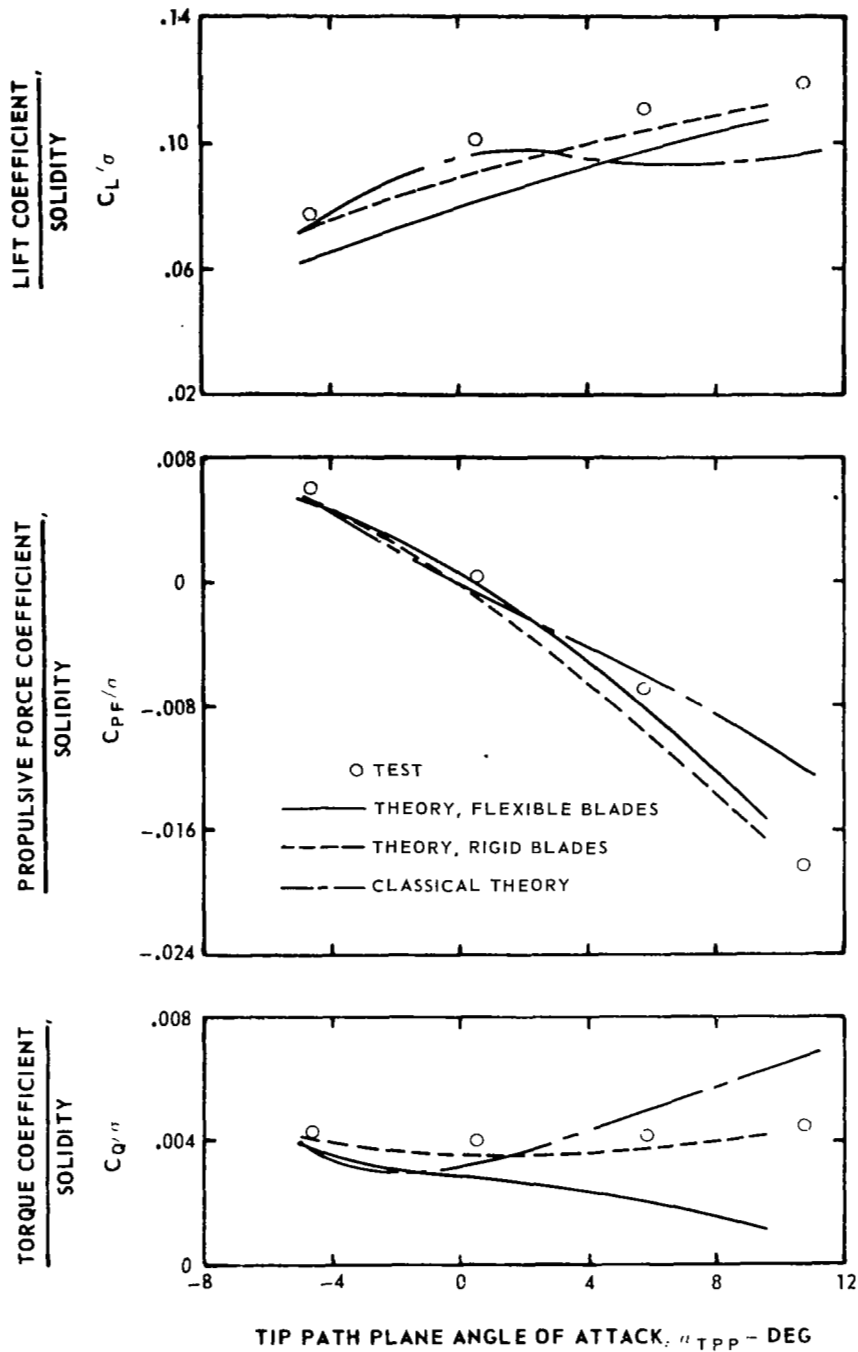
(a) Twist = −8 deg, advance ratio = 0.3

Figure 13. — Effect of blade flexibility on rotor performance with unsteady aerodynamics and variable inflow with wake distortions.
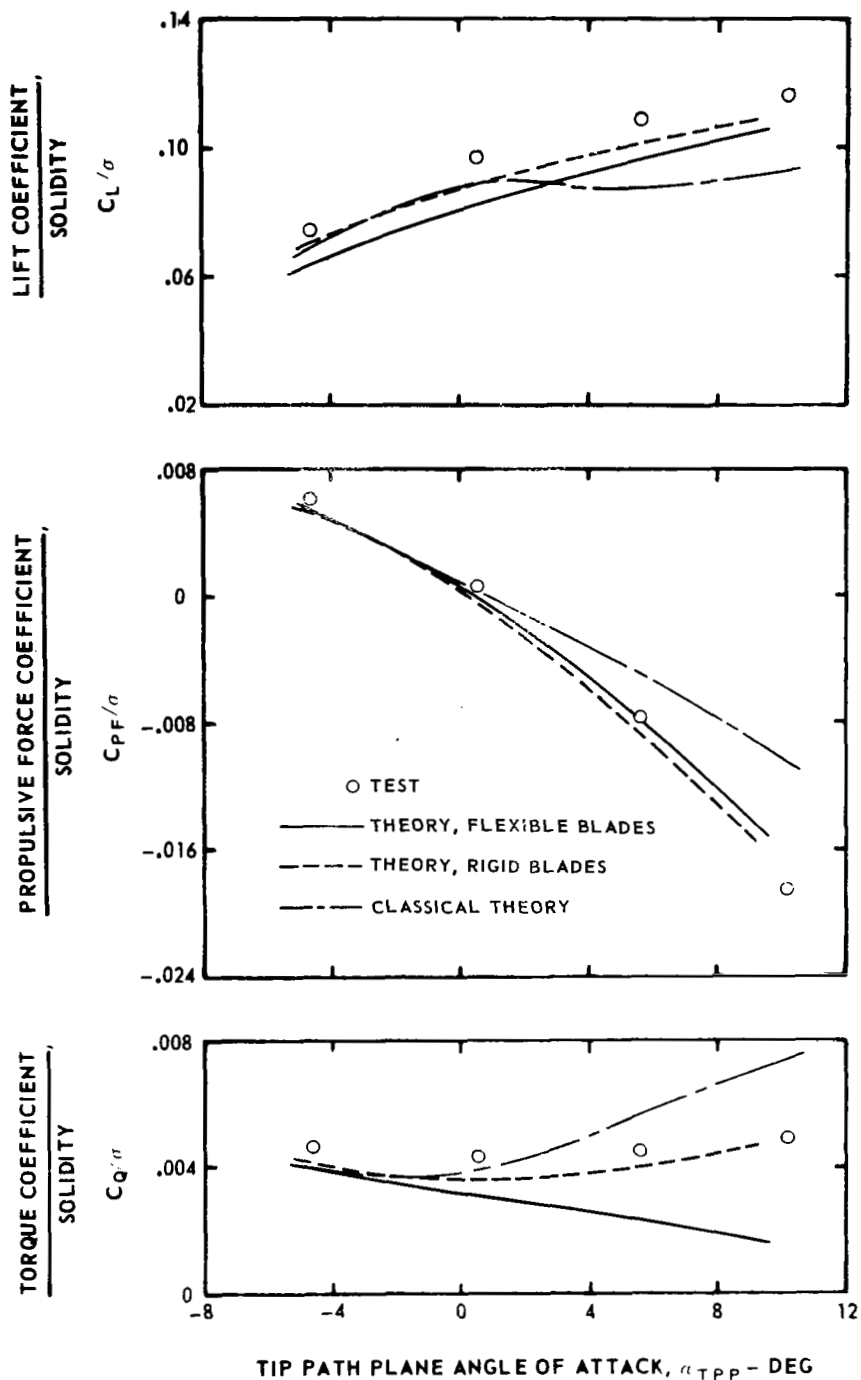
(b) Twist = 0 deg, advance ratio = 0.3

Figure 13. – Continued.

56
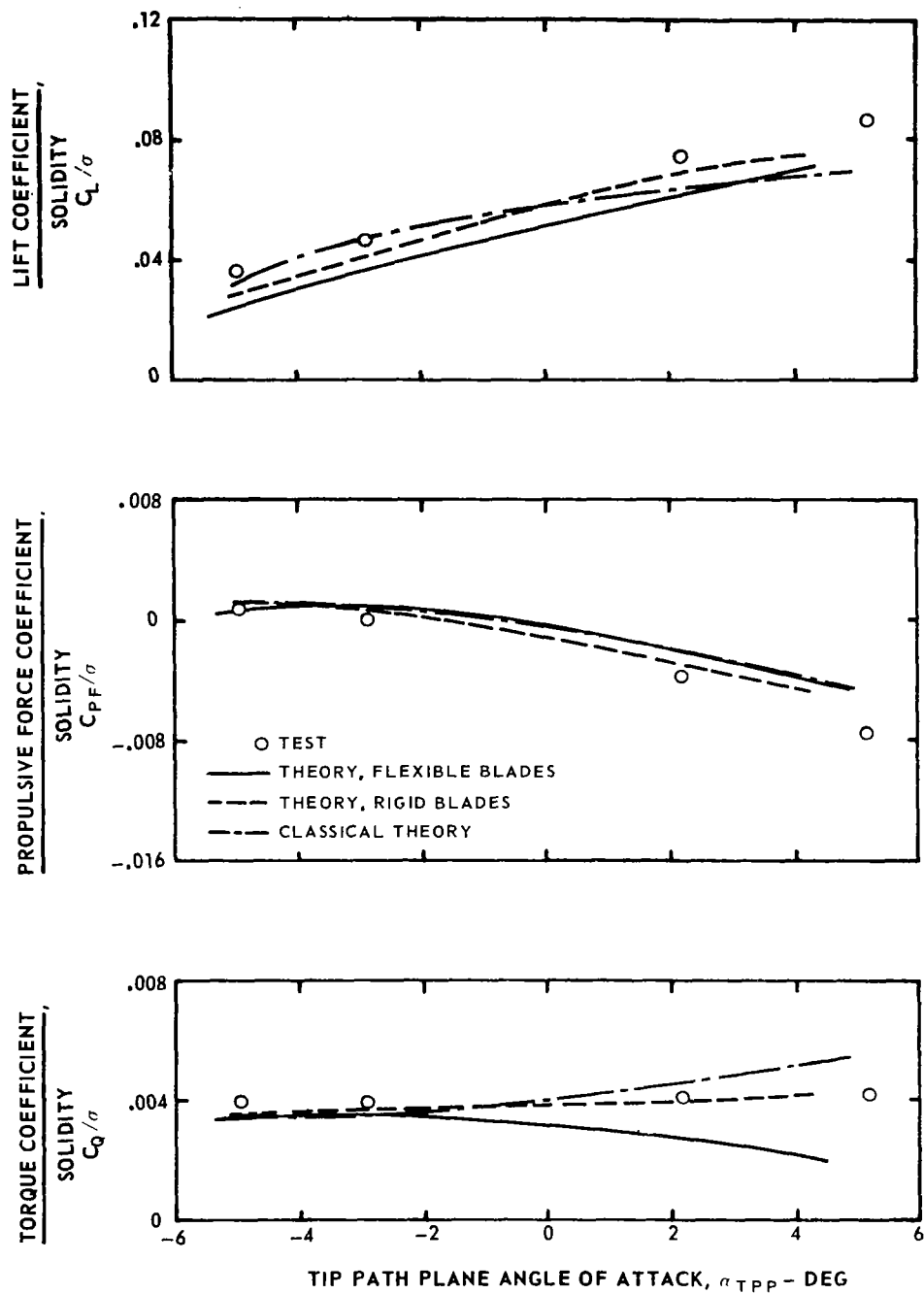
(c) Twist = 0 deg, advance ratio = 0.5

Figure 13. — Concluded.
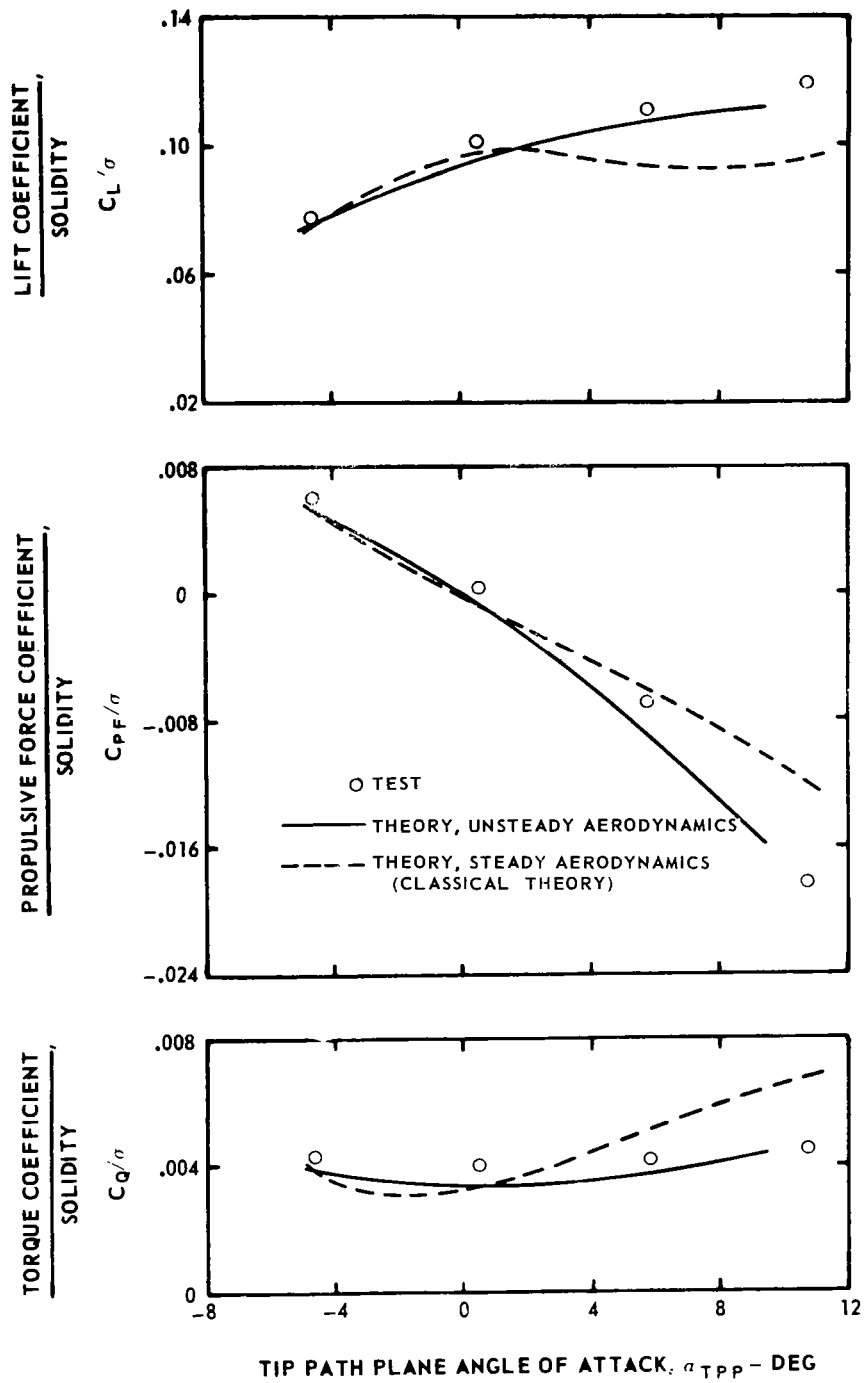
(a) Twist = −8 deg, advance ratio = 0.3

Figure 14.−Effect of unsteady aerodynamics on rotor performance with rigid blades and constant inflow.
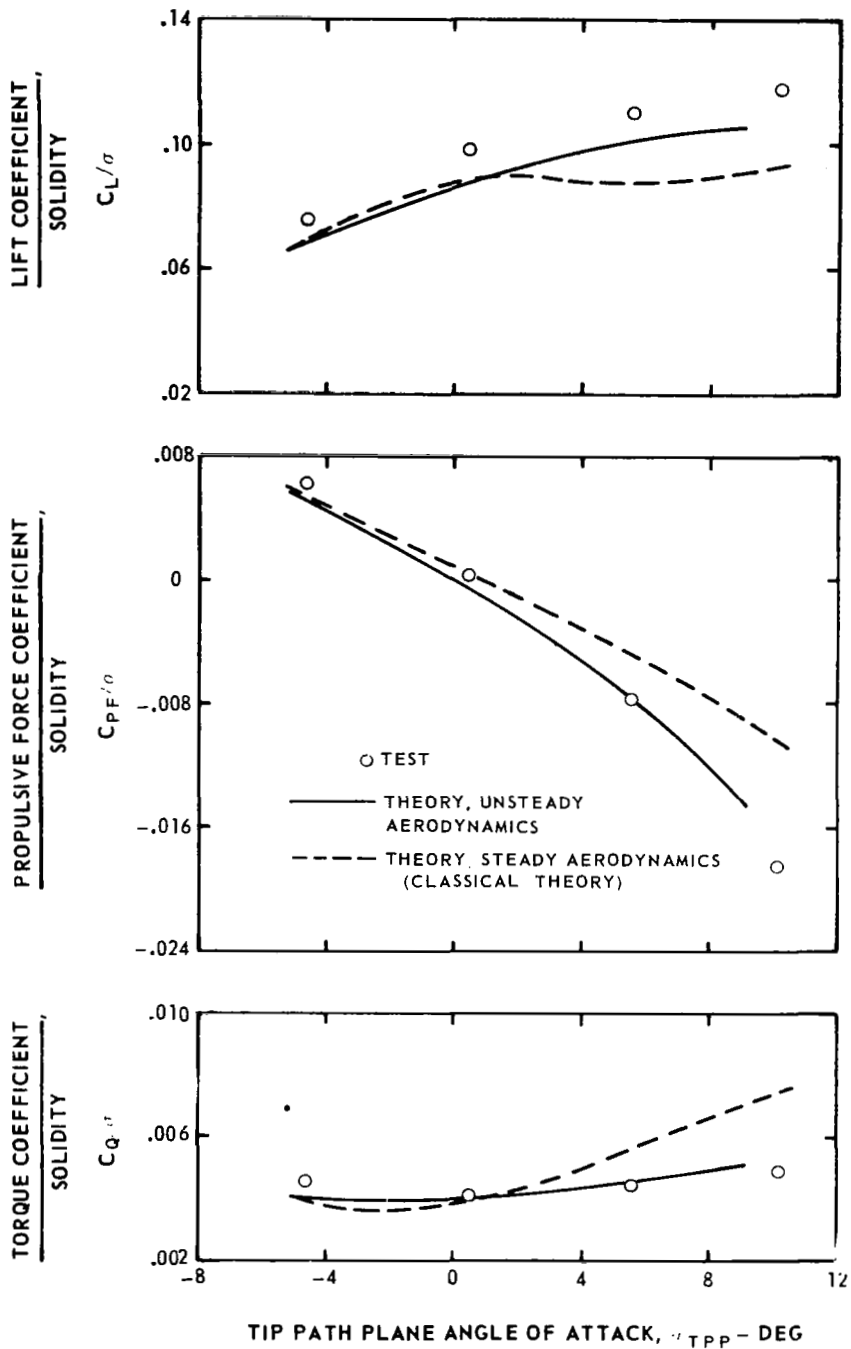
(b) Twist =0 deg, advance ratio =0.3

Figure 14. — Continued.
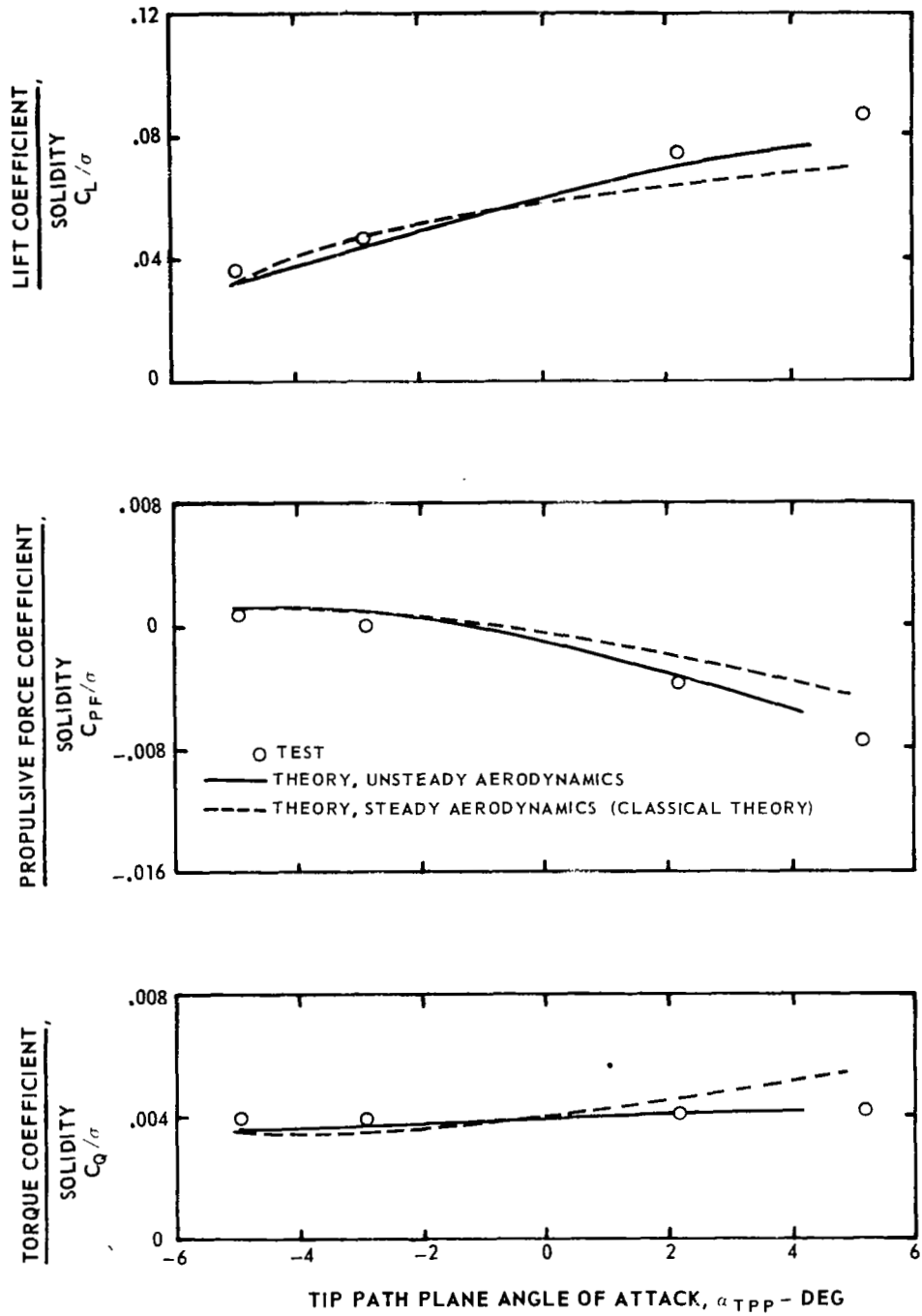
(c) Twist = 0 deg, advance ratio = 0.5

Figure 14. — Concluded.
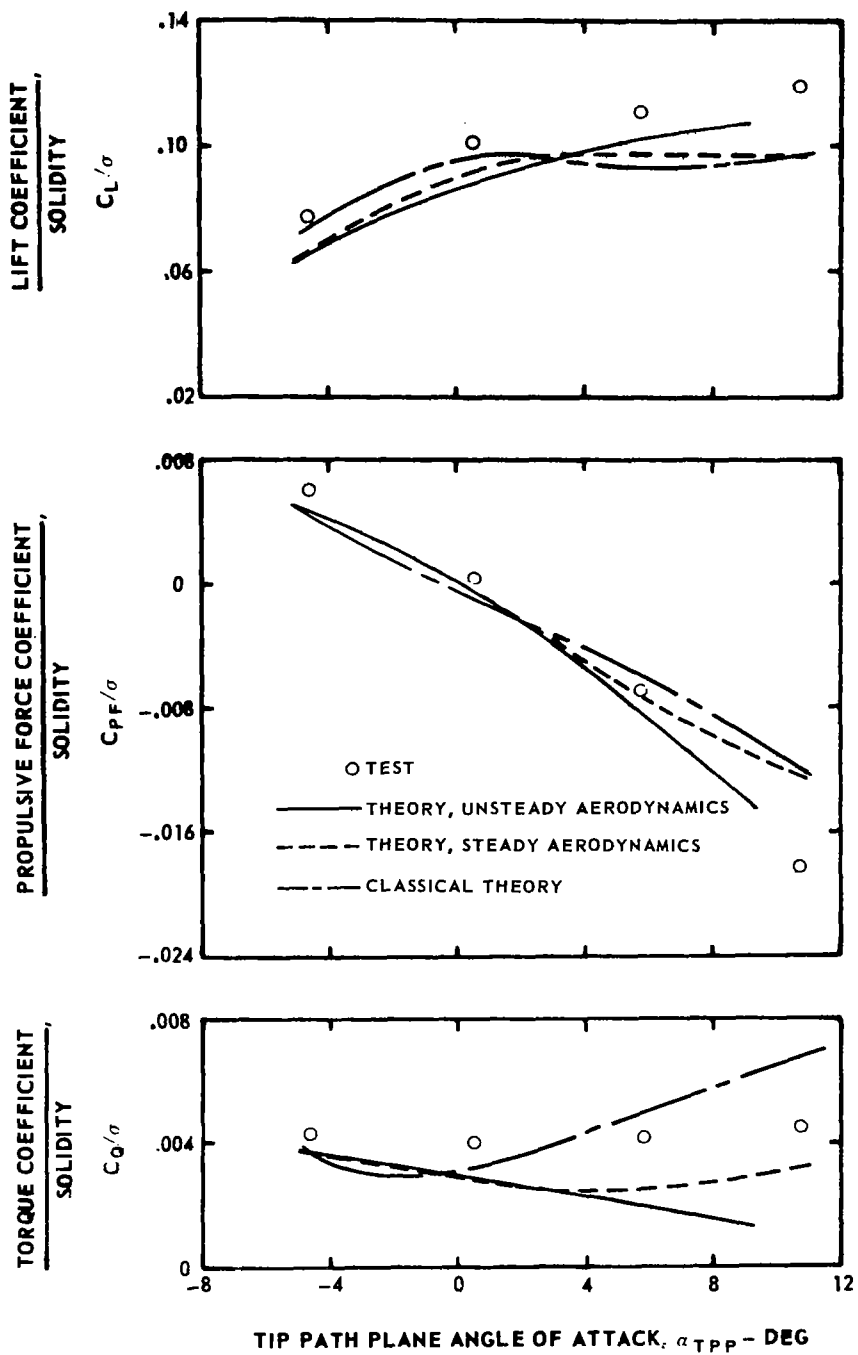
(a) Twist = −8 deg, advance ratio = 0.3

Figure 15.— Effect of unsteady aerodynamics on rotor performance with flexible blades and constant inflow.
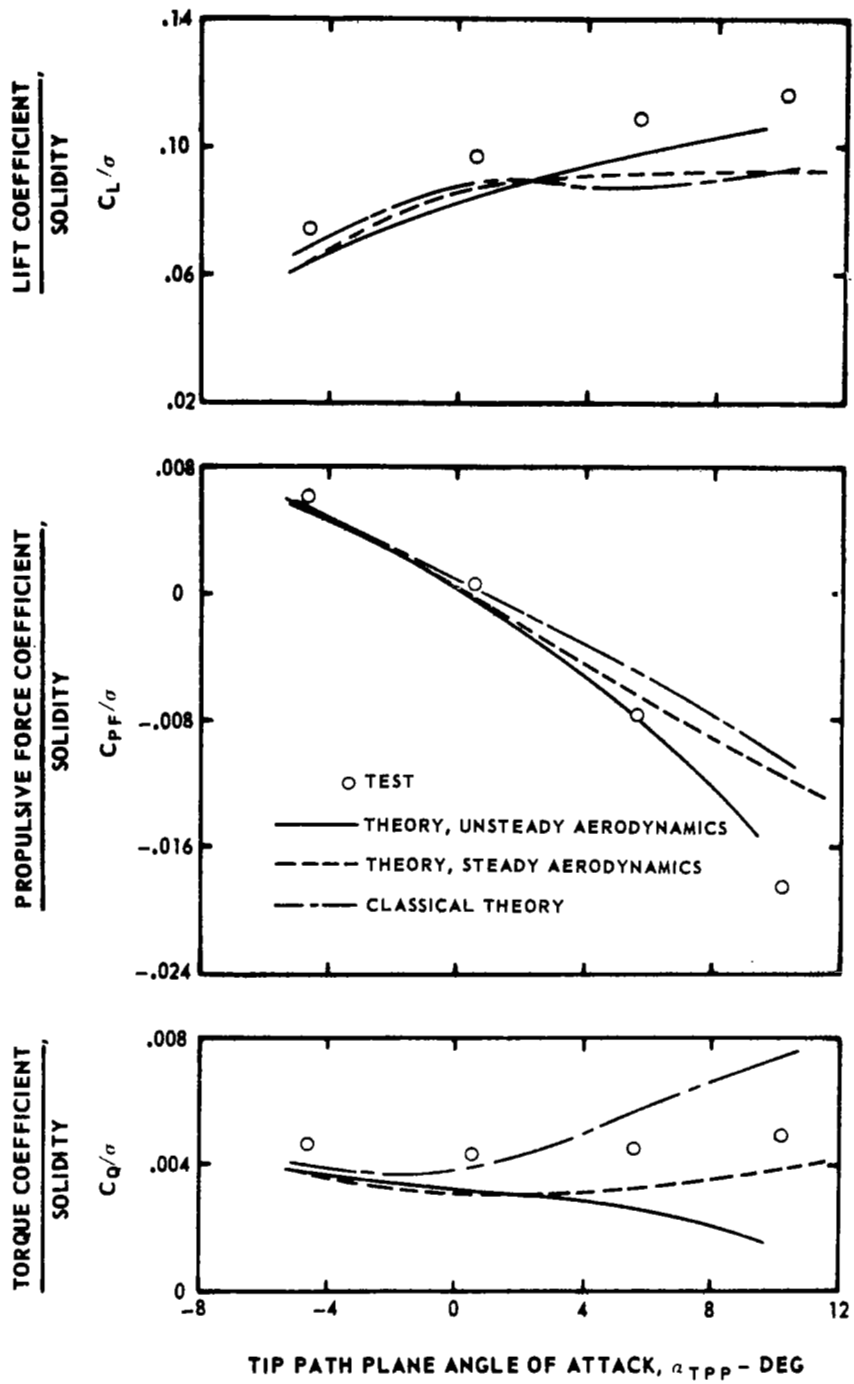
(b) Twist = 0 deg, advance ratio = 0.3

Figure 15. – Continued.
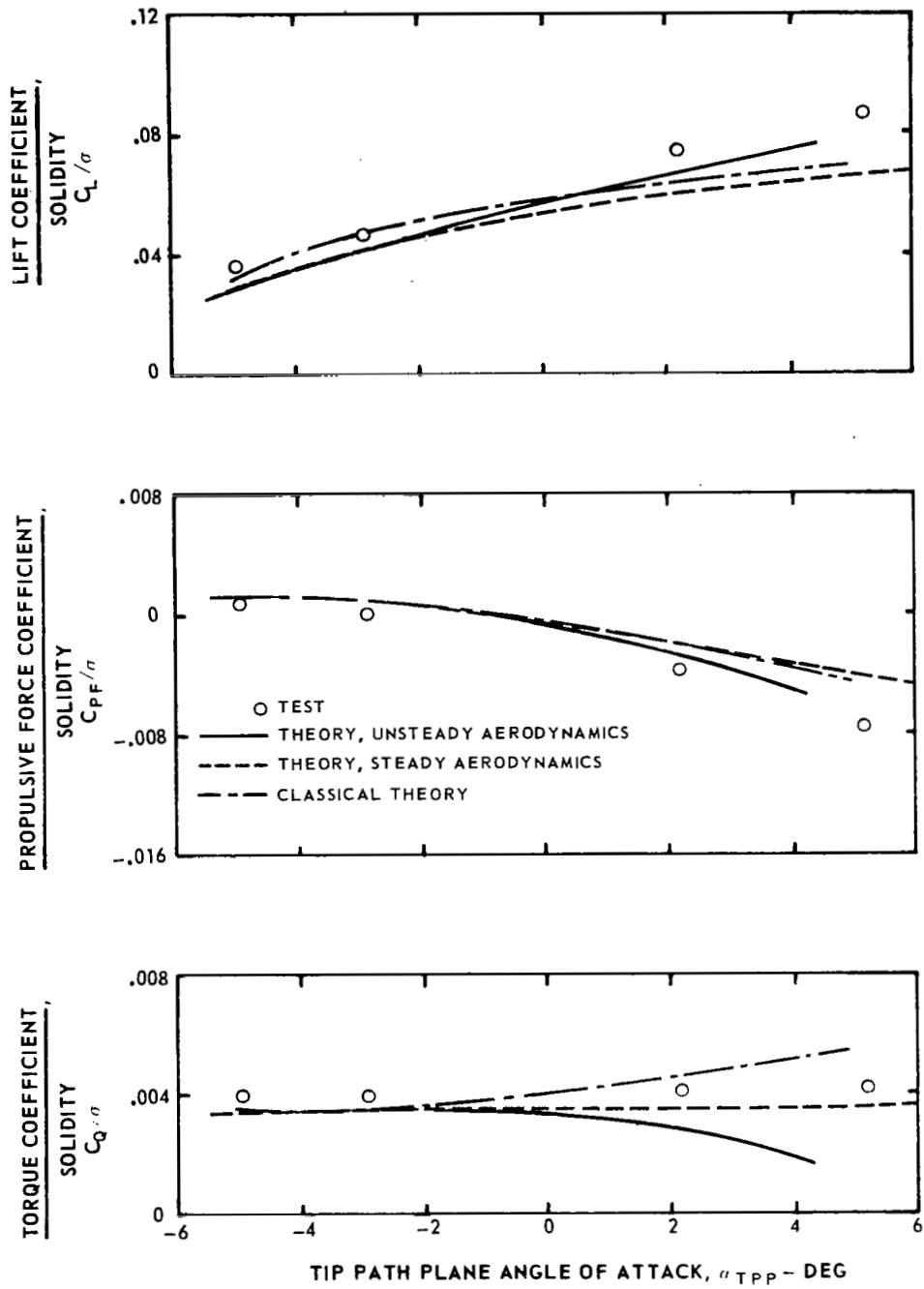
(c) Twist – 0 deg, advance ratio = 0.5

Figure 15. – Concluded.
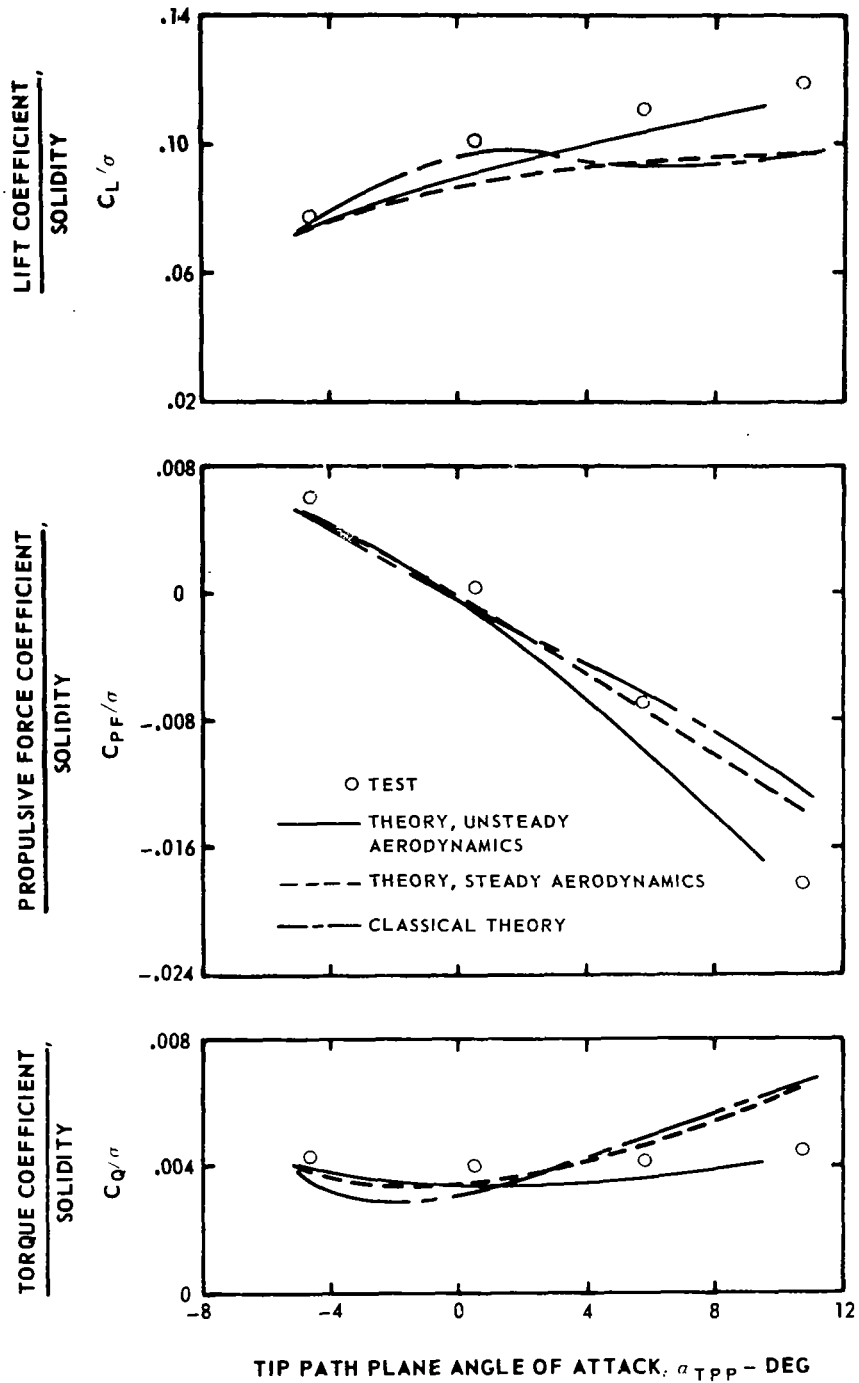
(a) Twist = −8 deg, advance ratio = 0.3

Figure 16.—Effect of unsteady aerodynamics on rotor performance with rigid blades and variable inflow with wake distortions.
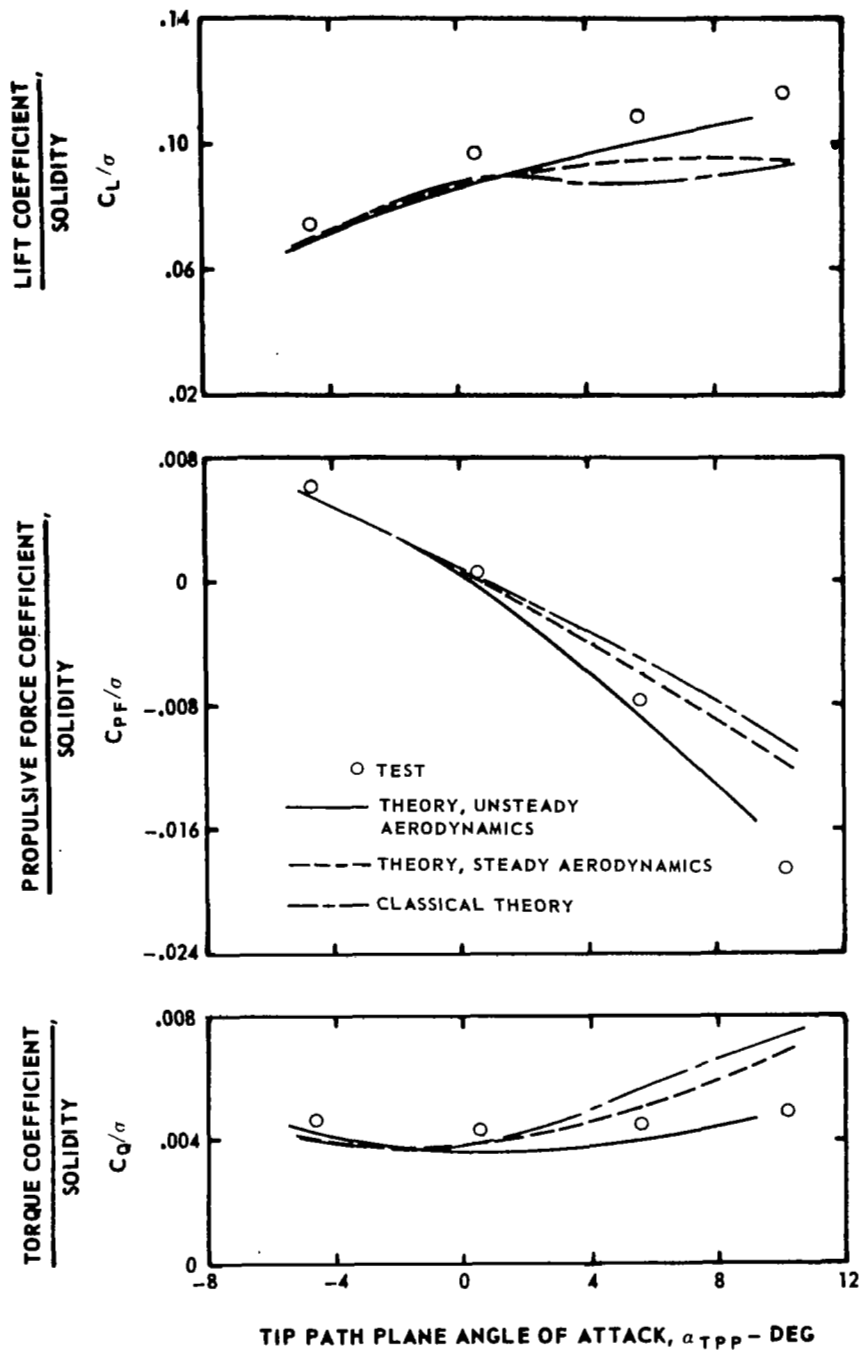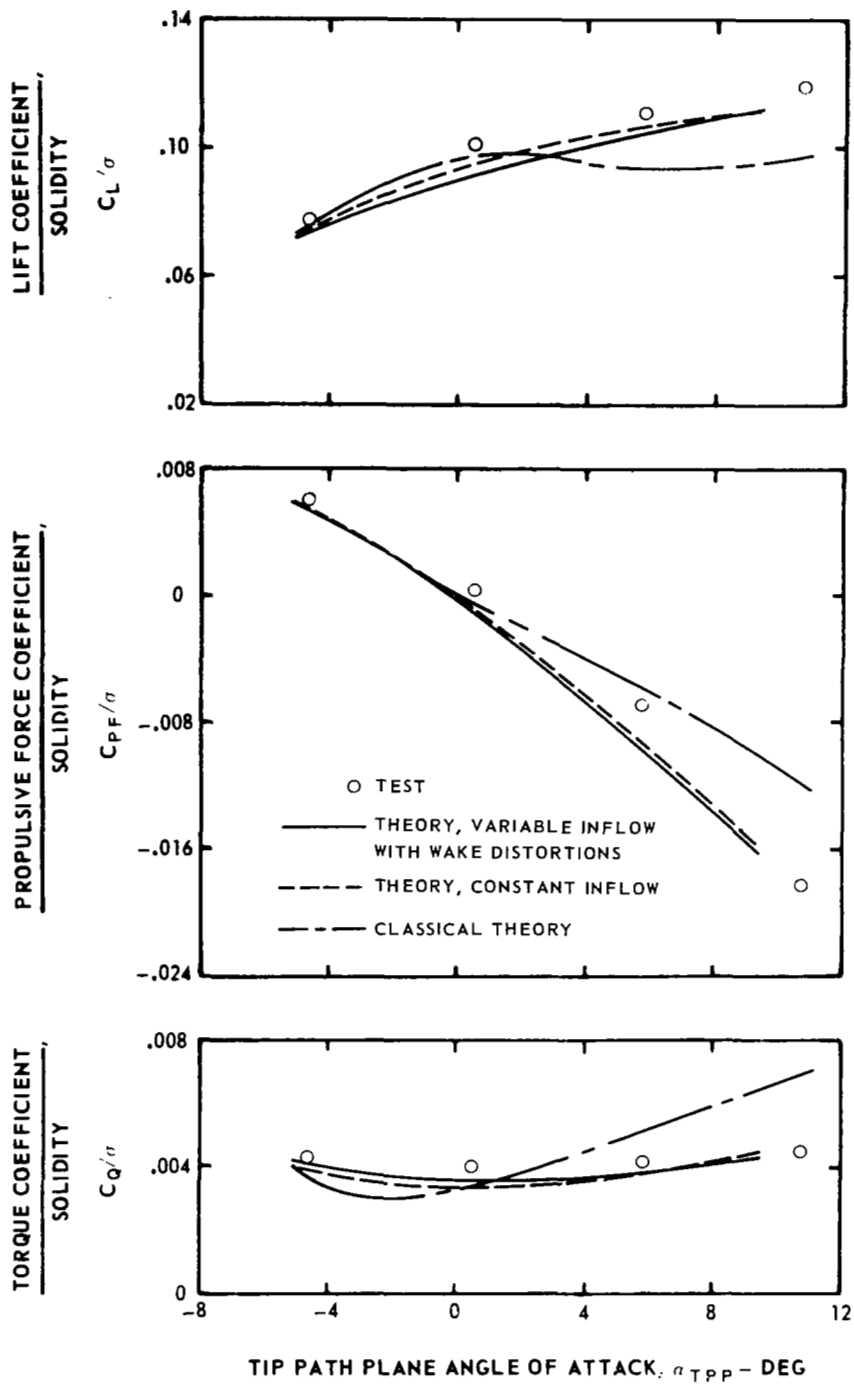
(b) Twist = 0 deg, advance ratio =0.3

Figure 16. – Continued.
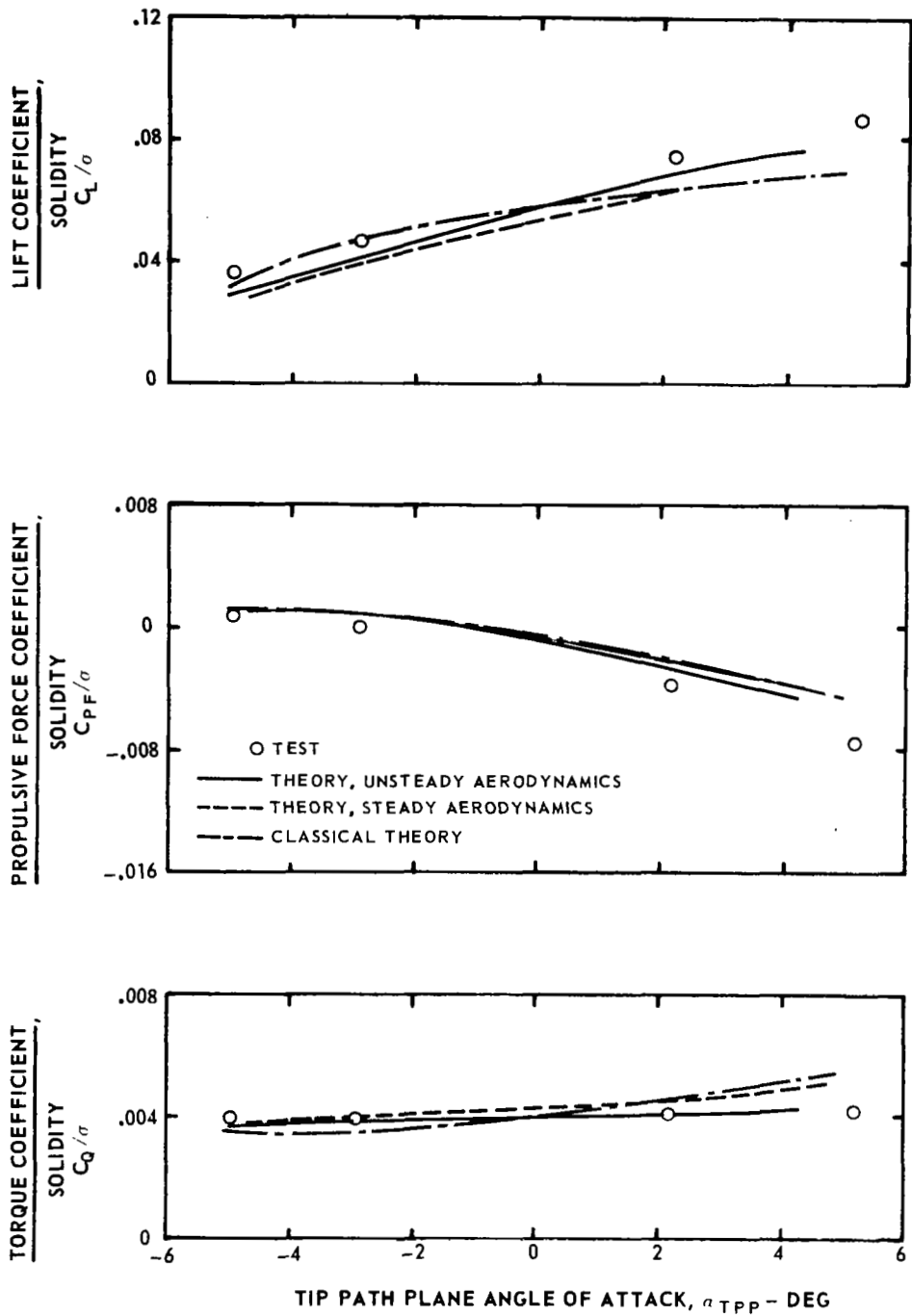
(c) Twist = 0 deg, advance ratio = 0.5

Figure 16. – Concluded.
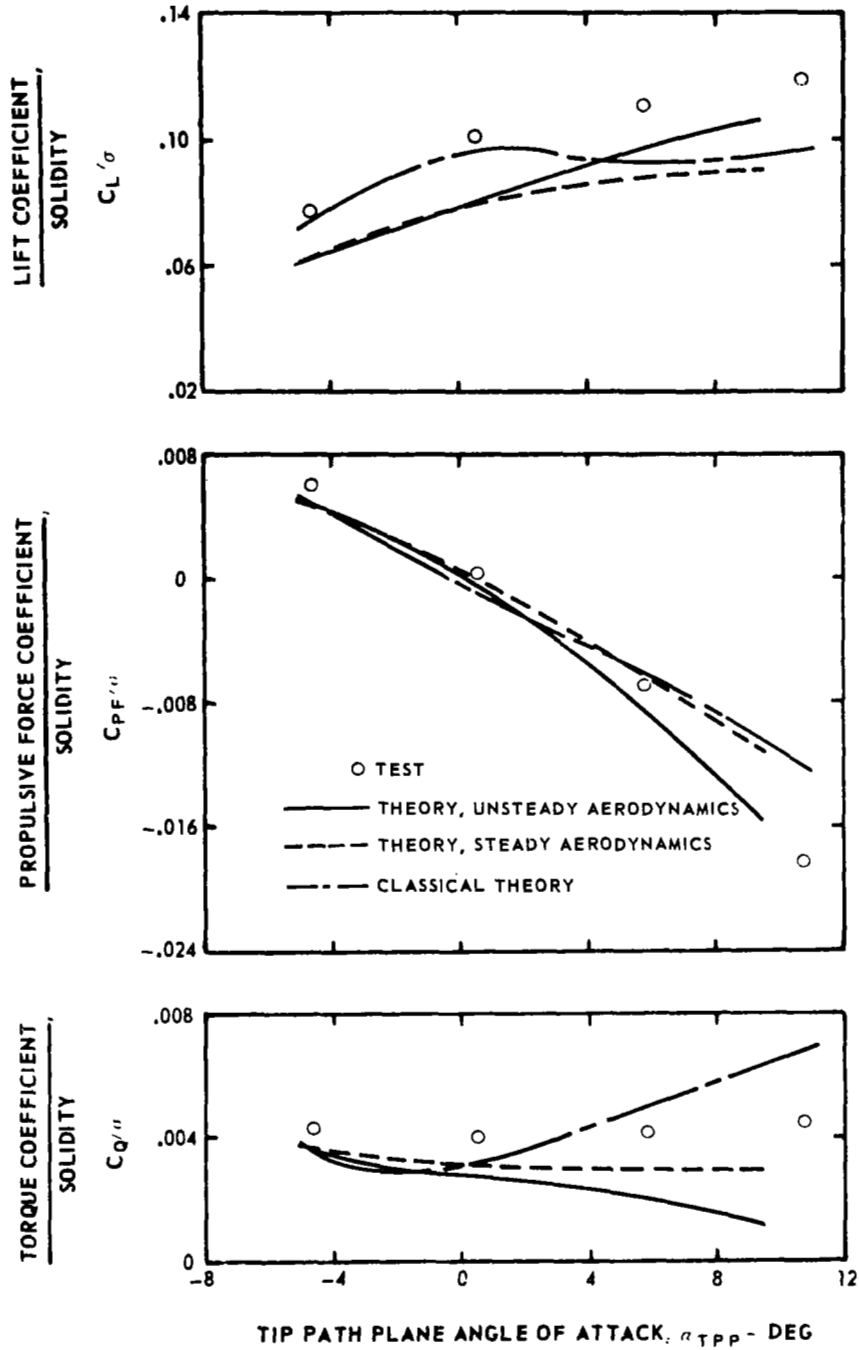
(a) Twist = −8 deg, advance ratio - 0.3

Figure 17.— Effect of unsteady aerodynamics on rotor performance with flexible blades and variable inflow with wake distortions.
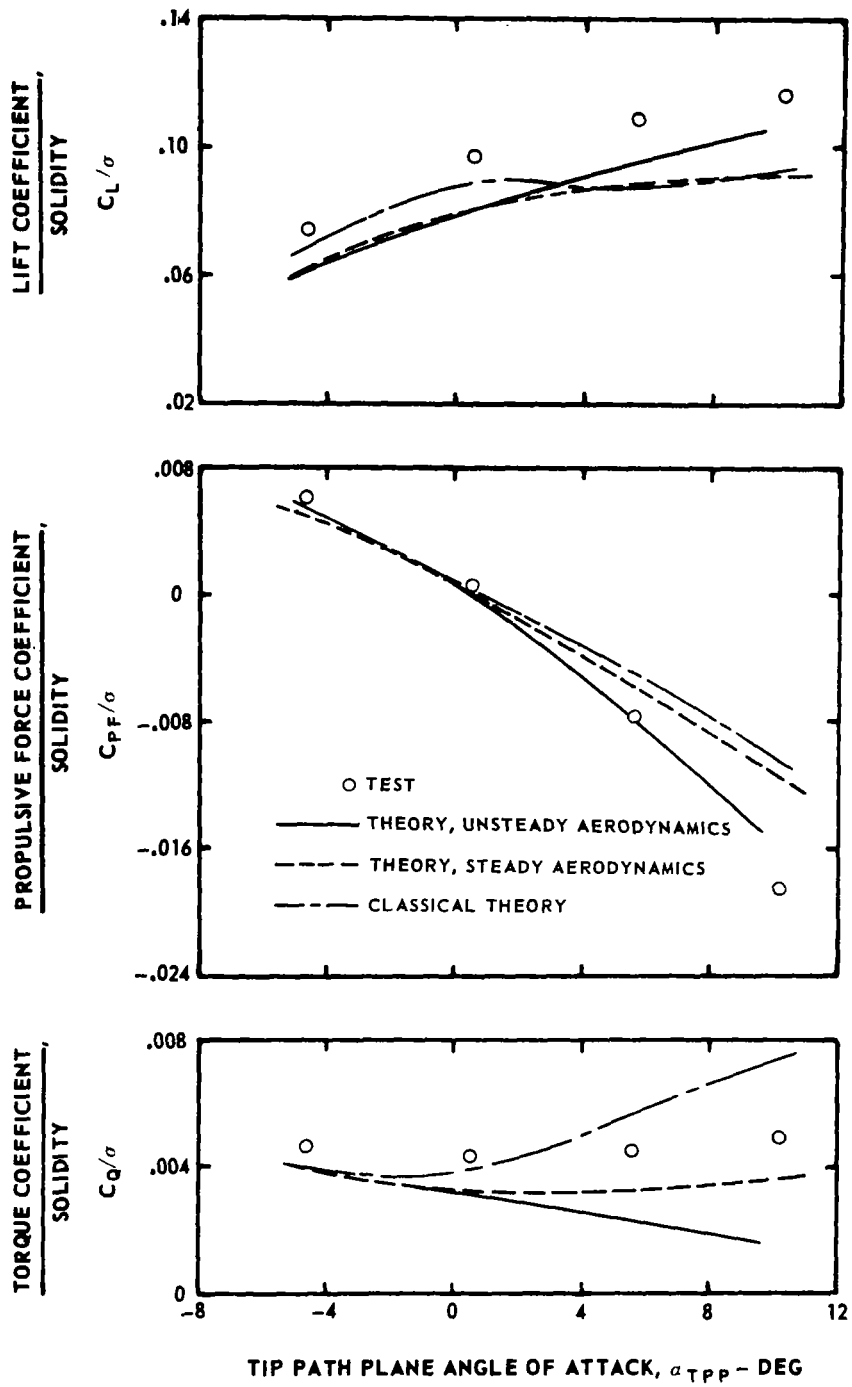
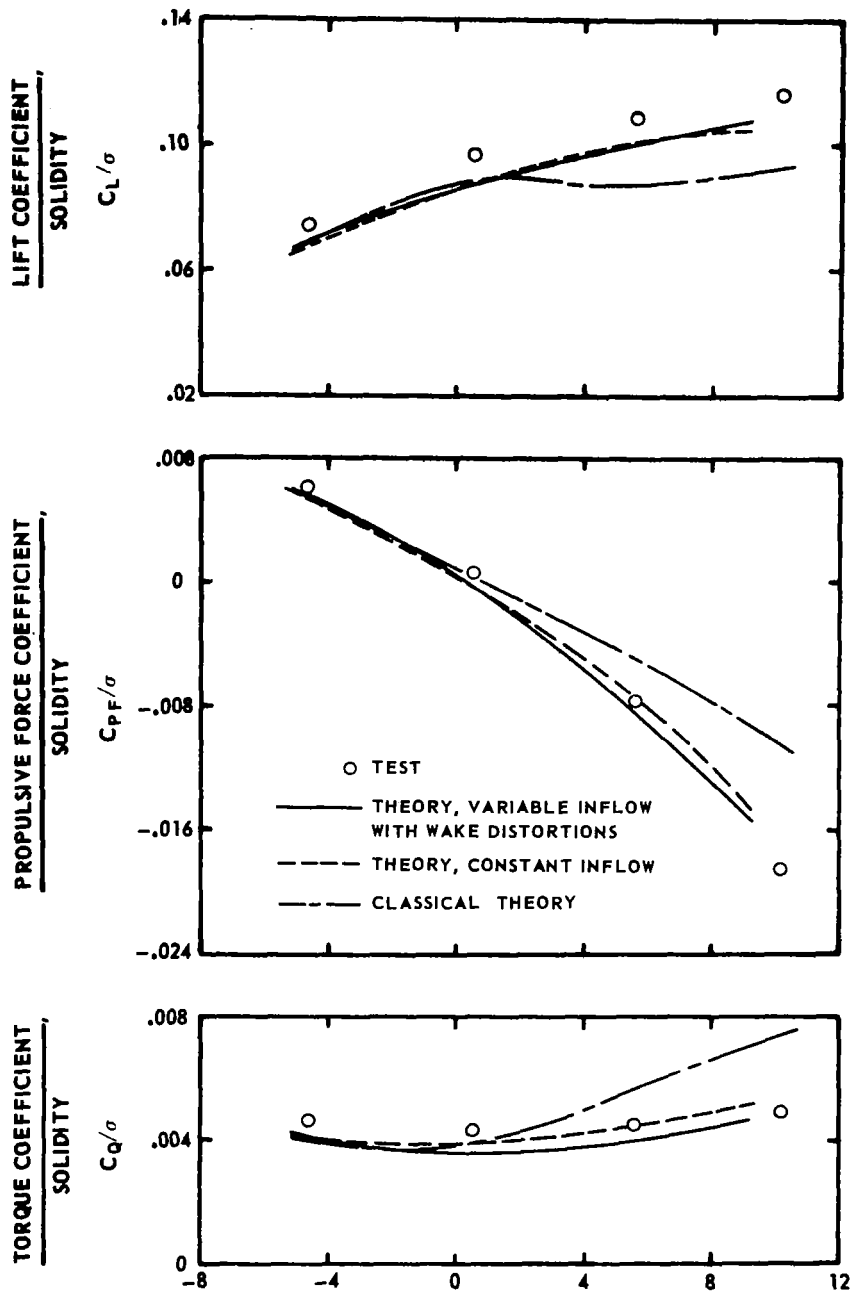(b) Twist = 0 deg, advance ratio = 0.3

Figure 17. — Continued.
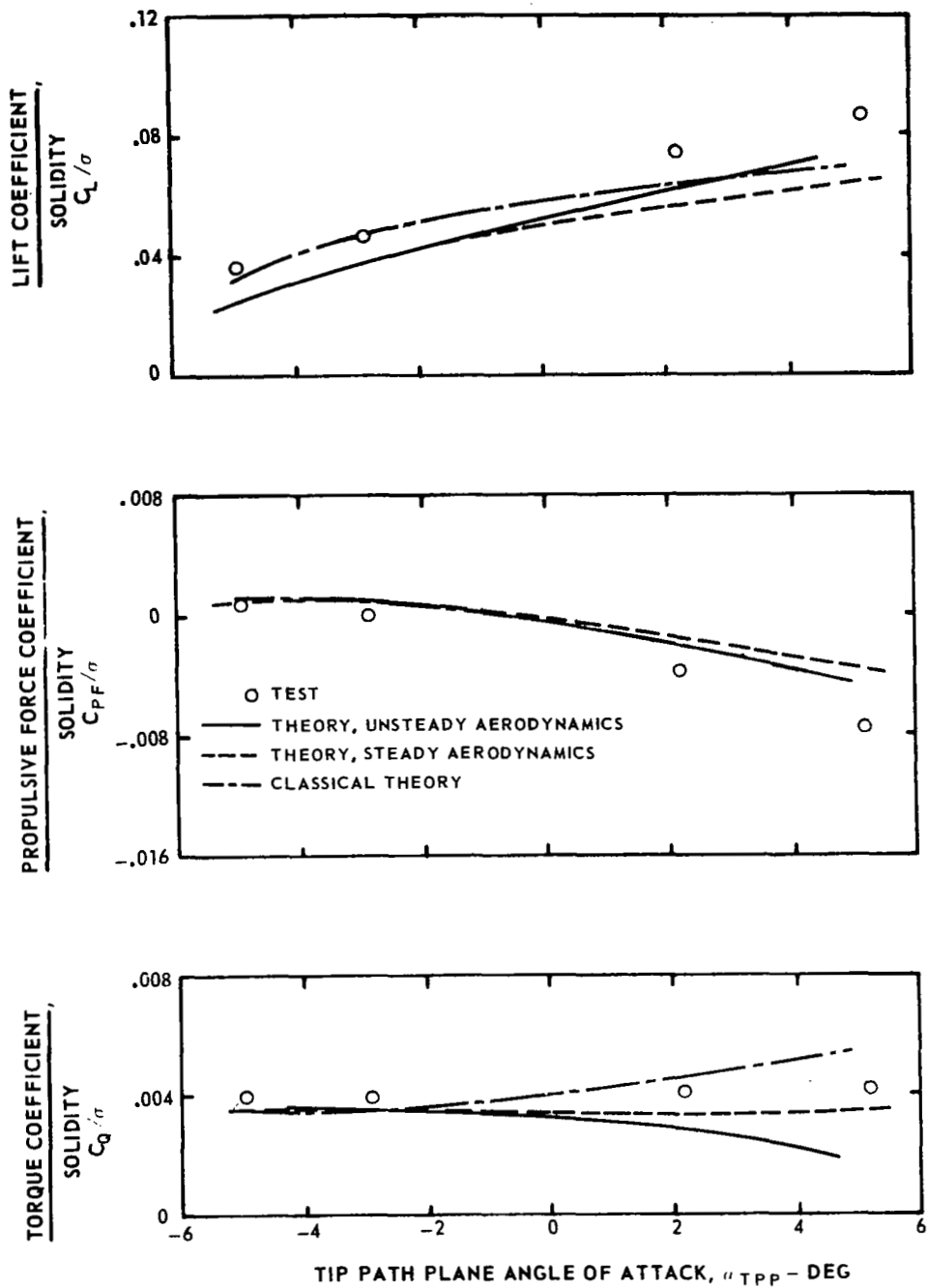
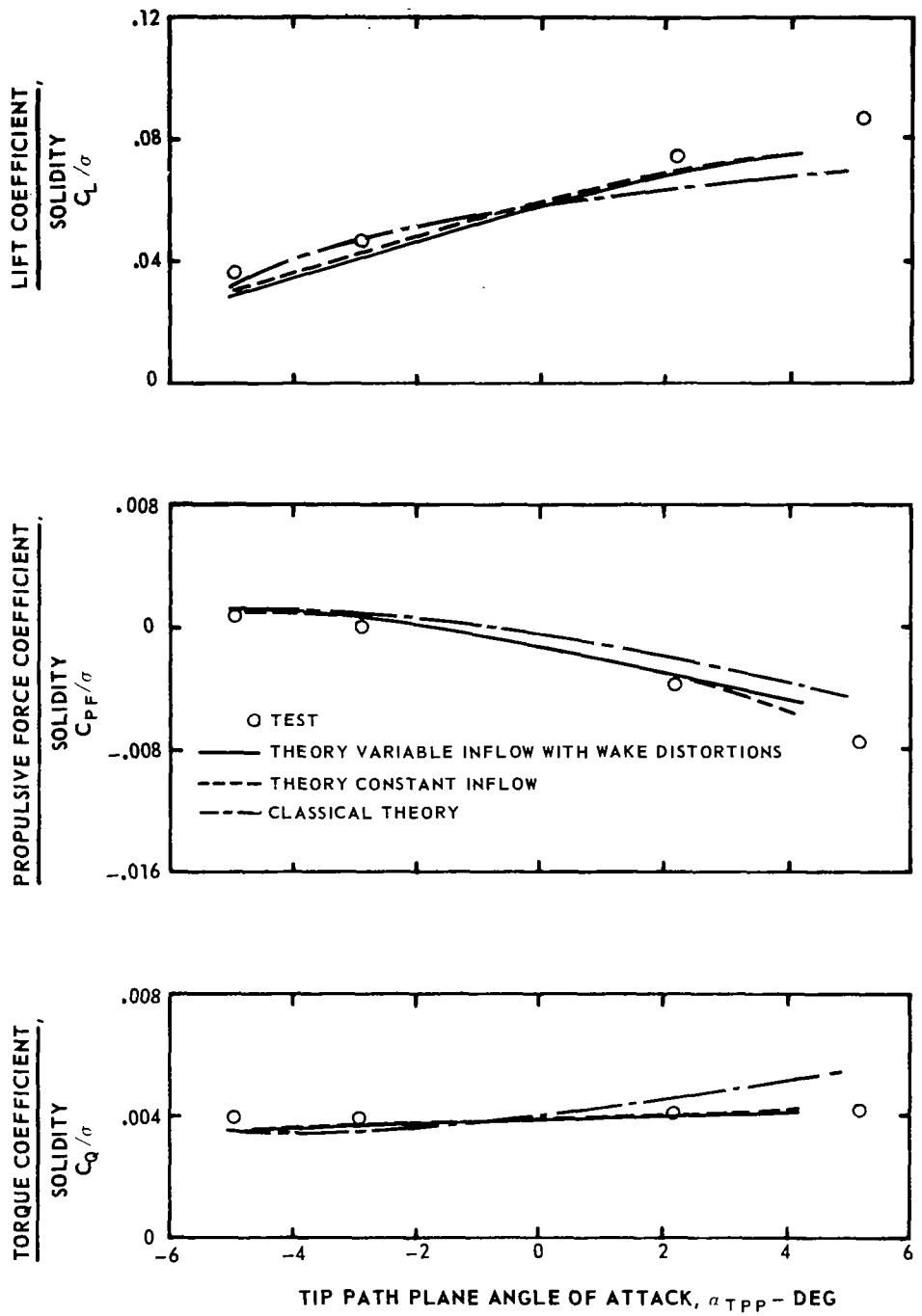(c) Twist = 0 deg, advance ratio = 0.5

Figure 17. – Concluded.
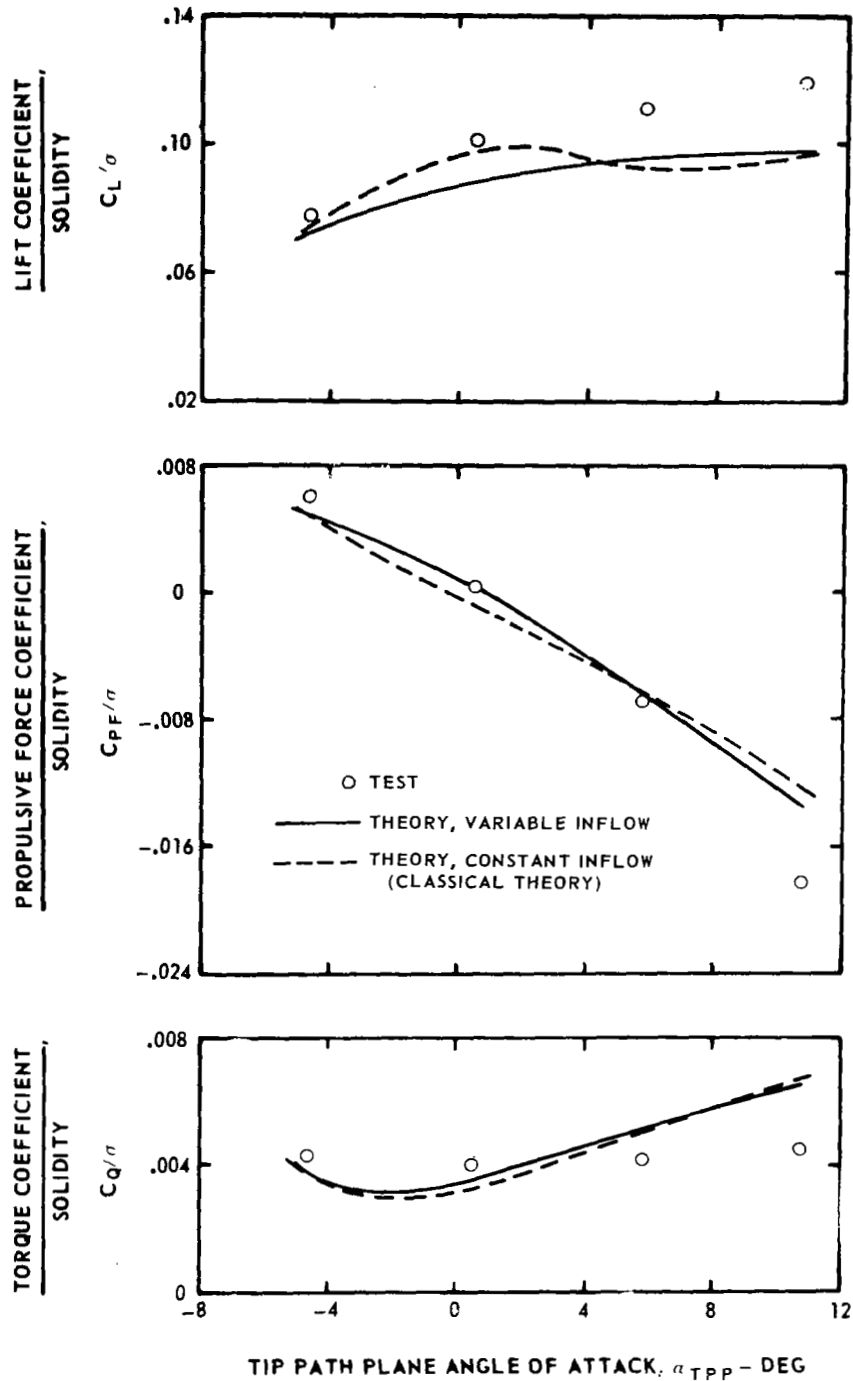
(a) Twist = −8 deg, advance ratio = 0.3

Figure 18.— Effect of variable inflow without wake distortions on rotor performance with rigid blades and steady aerodynamics.
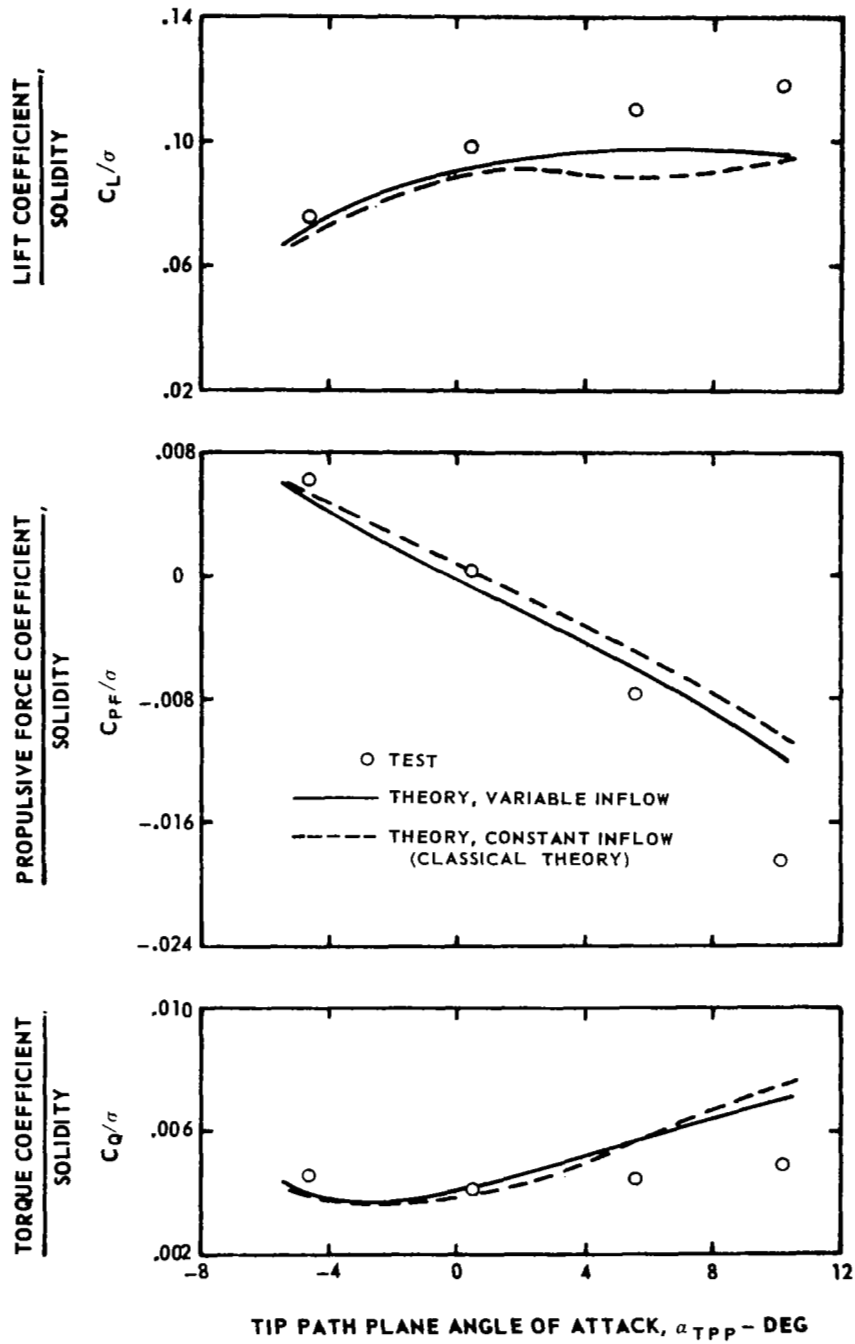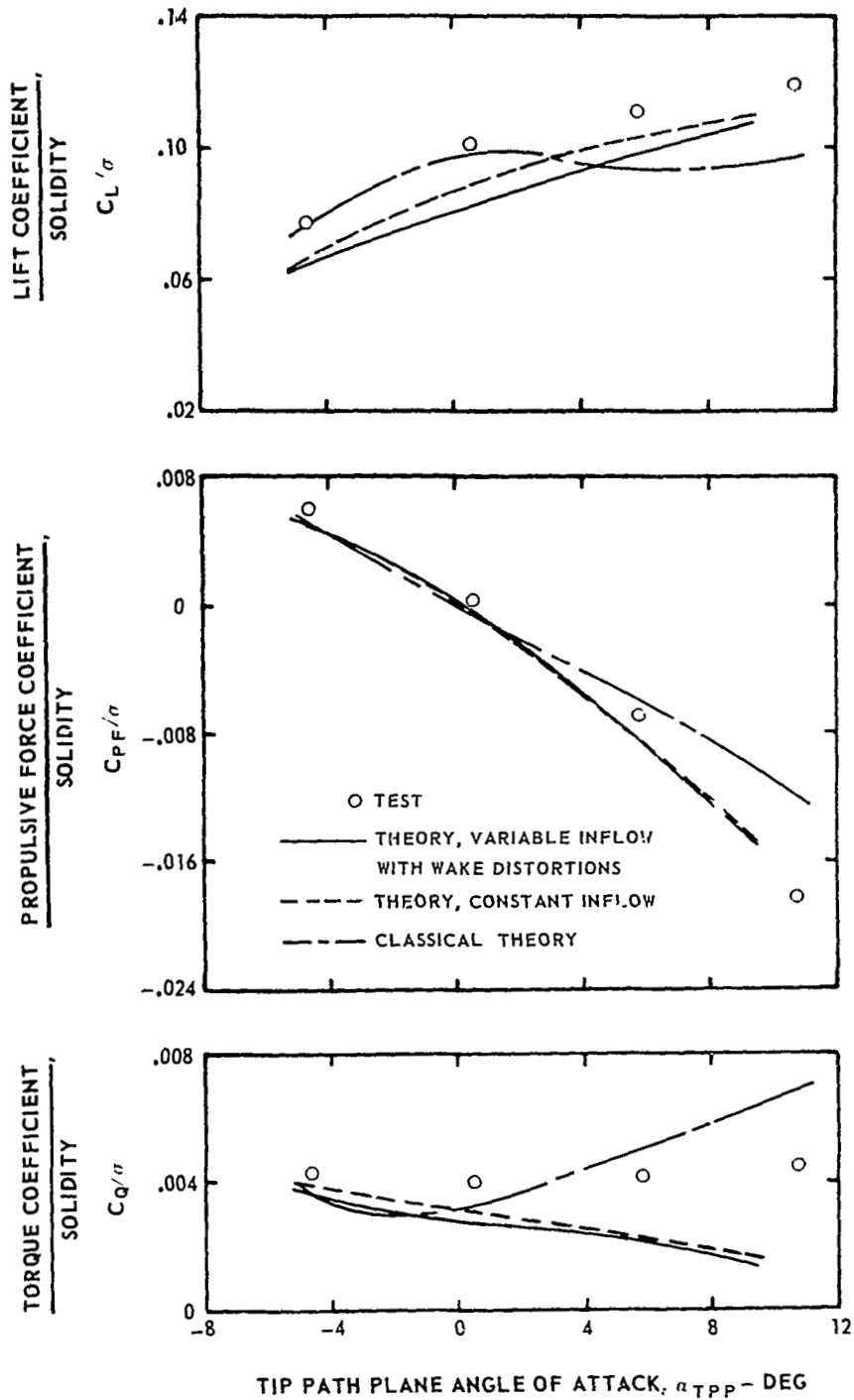
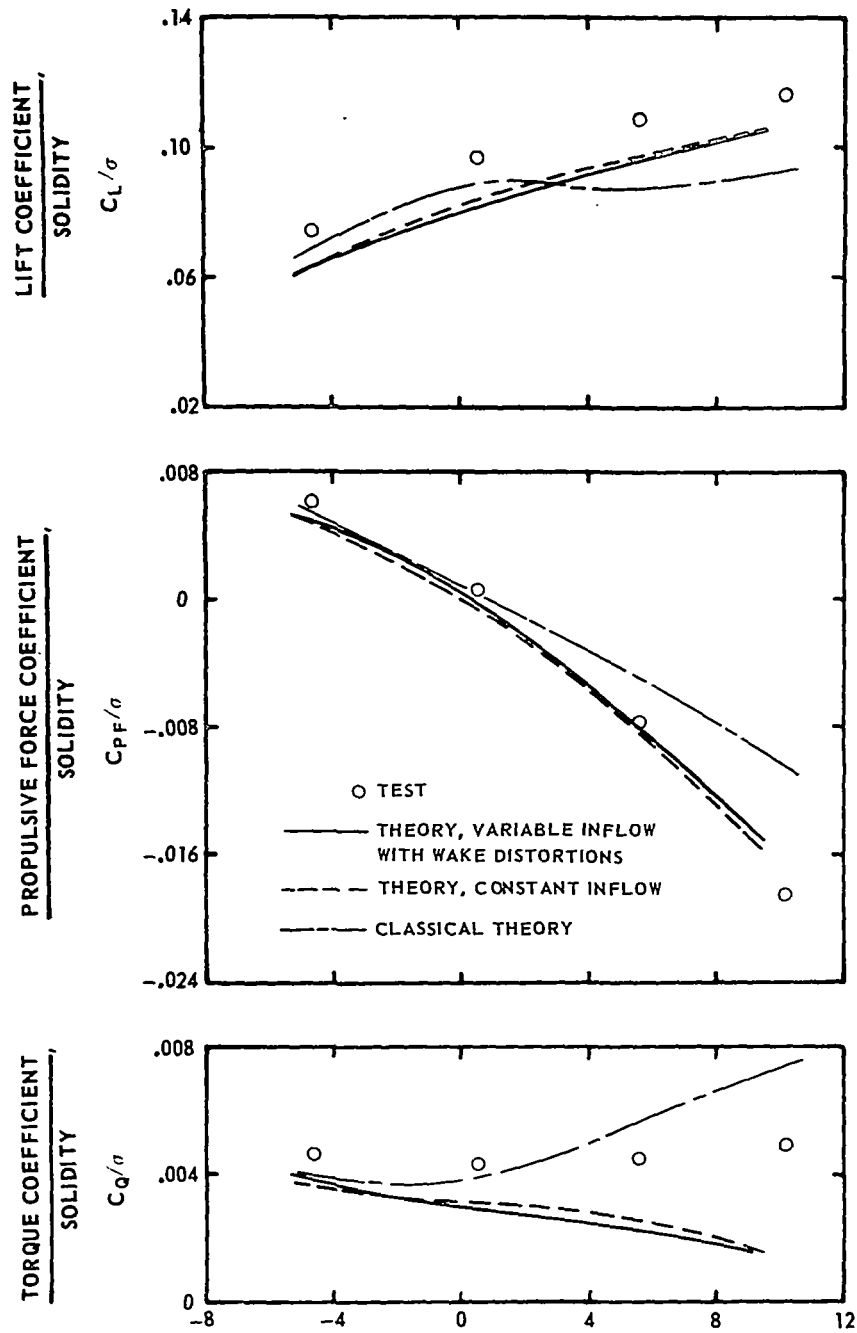(b) Twist = 0 deg, advance ratio = 0.3

Figure 18. – Continued.
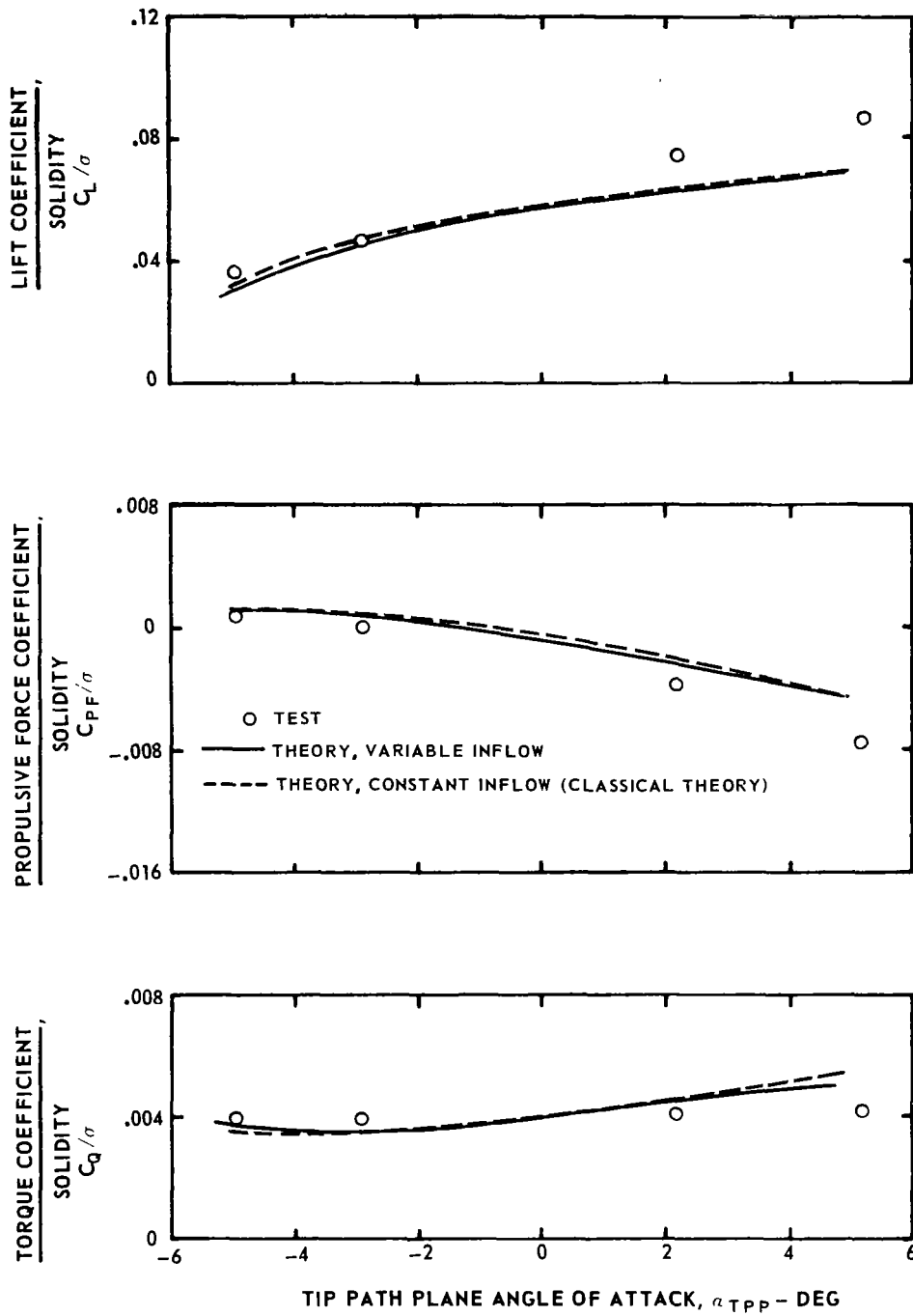
(c) Twist = 0 deg, advance ratio = 0.5

Figure 18. — Concluded.
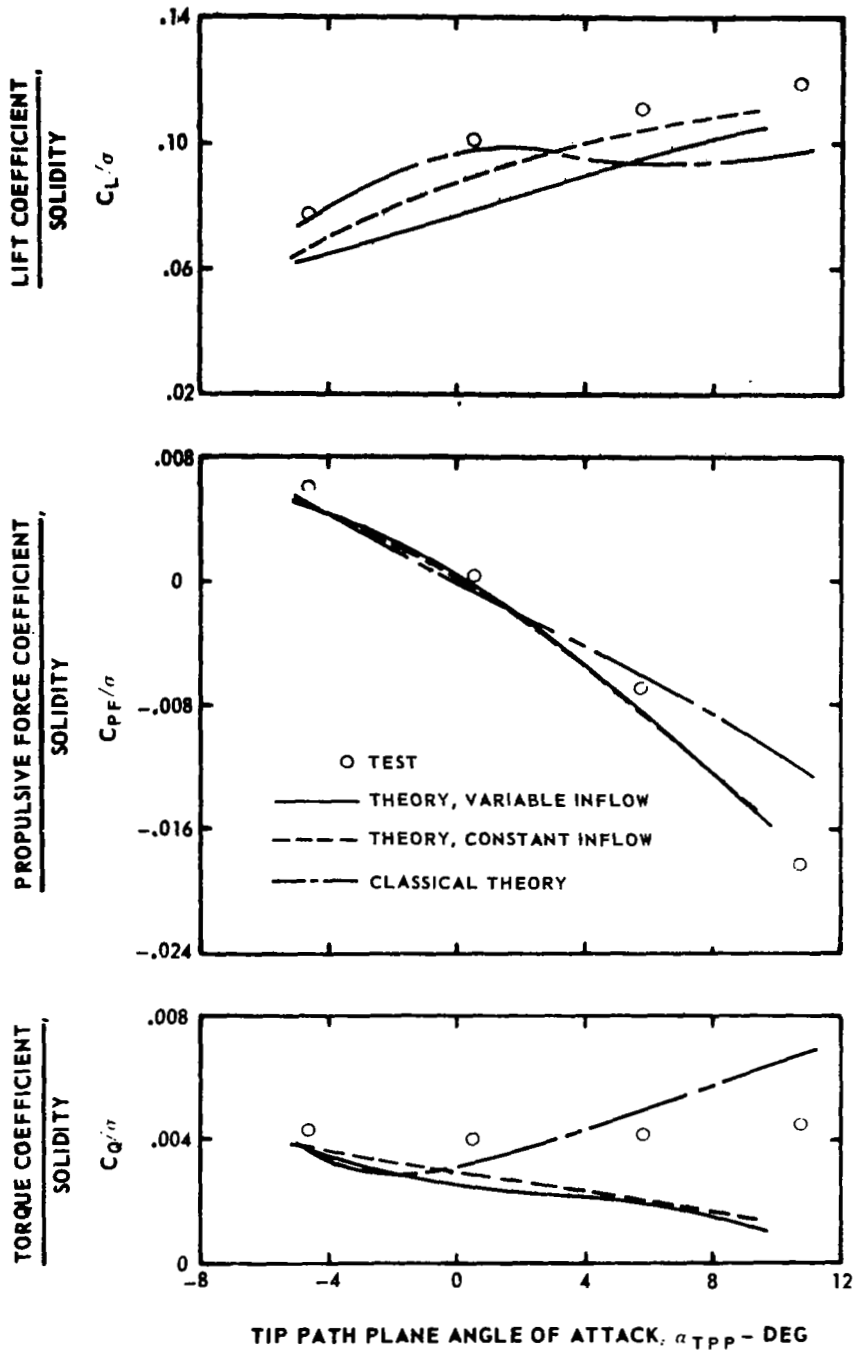
(a) Twist = −8 deg, advance ratio = 0.3

Figure 19. — Effect of variable inflow without wake distortions on rotor performance with flexible blades and unsteady aerodynamics.

73
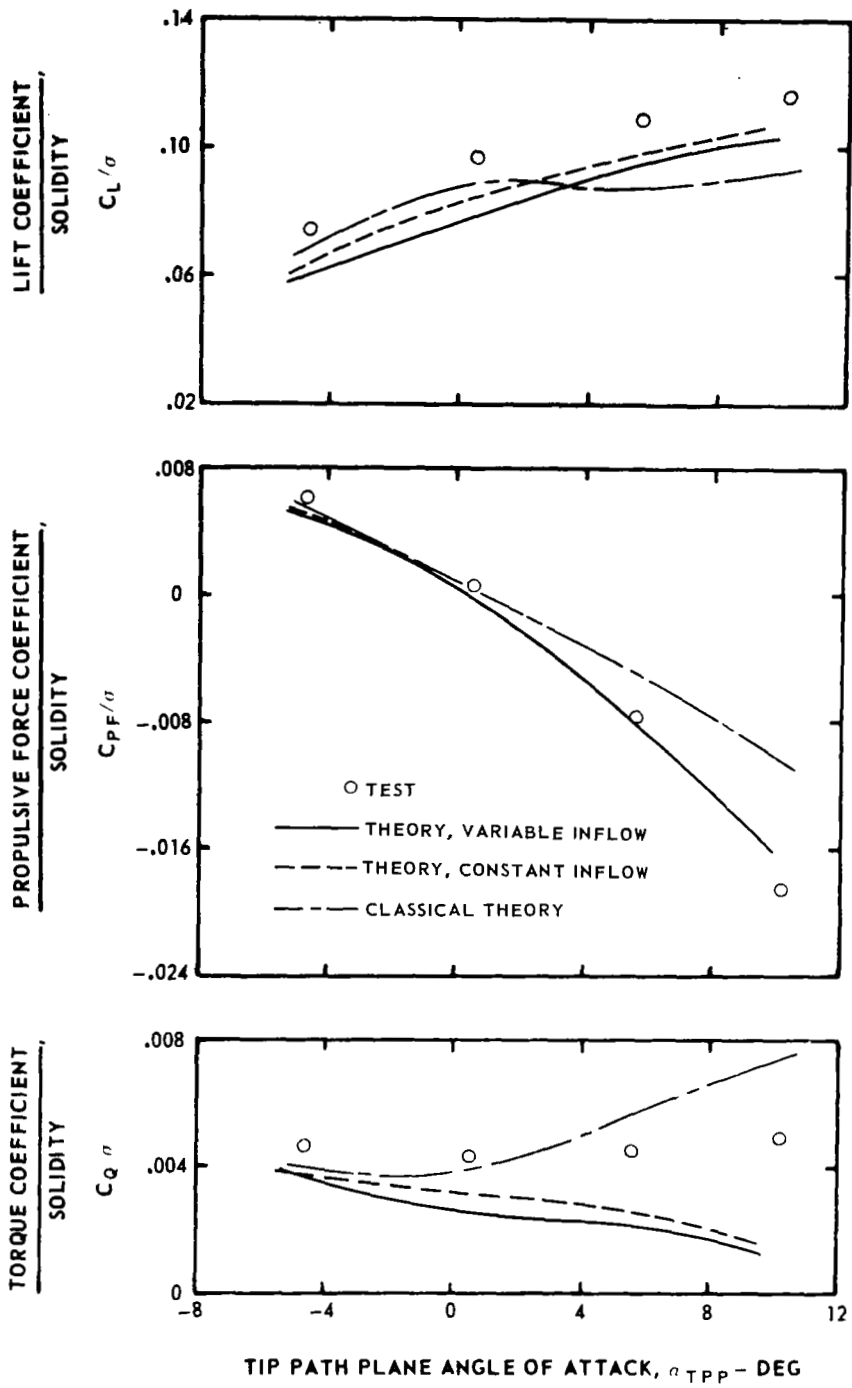
(b) Twist = 0 deg, advance ratio = 0.3

Figure 19. — Continued.

LIFT COEFFICIENT / SOLIDITY, C_L/σ

PROPULSIVE FORCE COEFFICIENT / SOLIDITY, C_{PF}/σ

○ TEST
——— THEORY, VARIABLE INFLOW
– – – THEORY, CONSTANT INFLOW
– · – CLASSICAL THEORY

TORQUE COEFFICIENT / SOLIDITY, C_Q/σ

TIP PATH PLANE ANGLE OF ATTACK, α_{TPP} – DEG
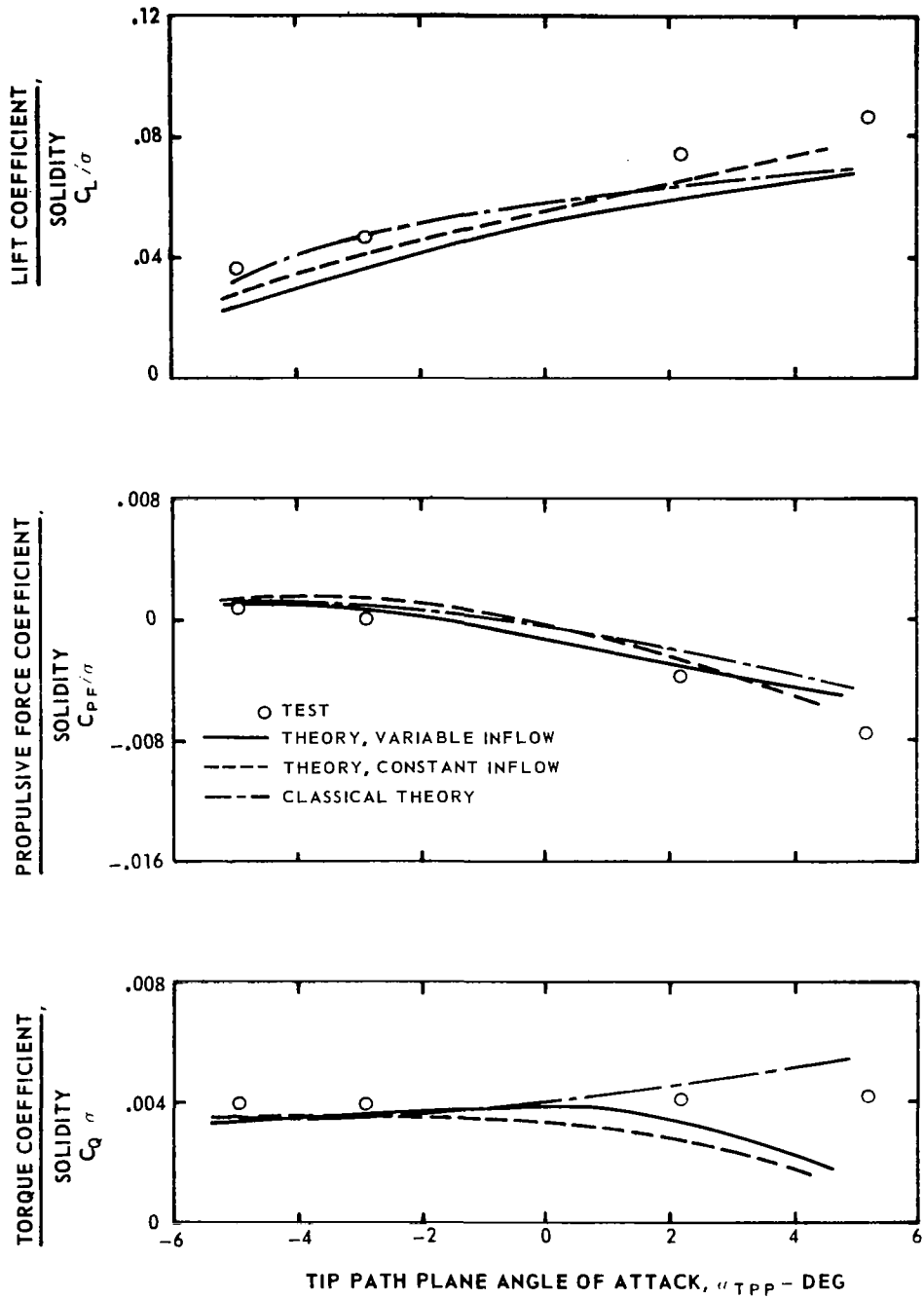
(c) Twist = 0 deg, advance ratio = 0.5

Figure 19. — Concluded.

75
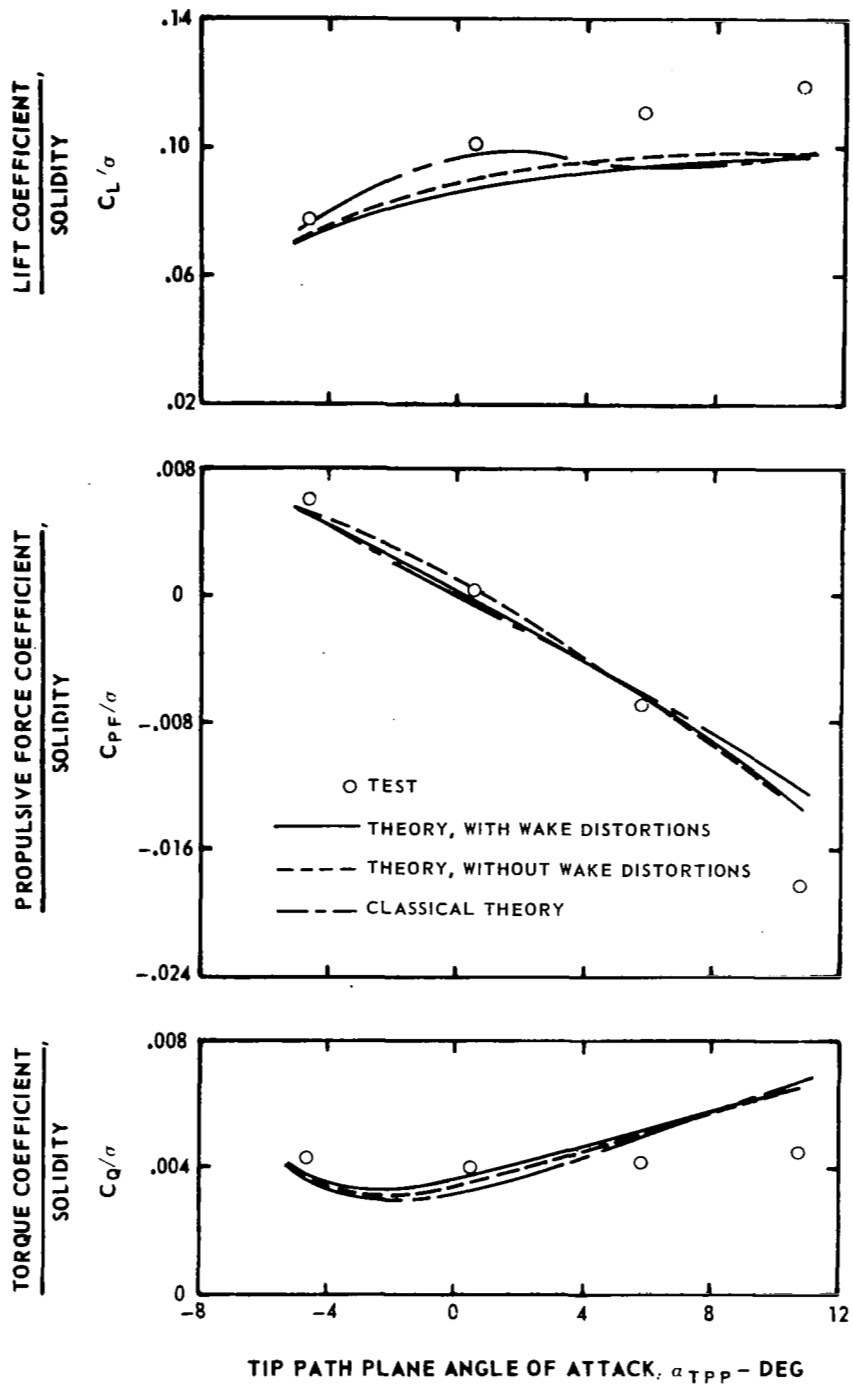
(a) Twist = −8 deg, advance ratio = 0.3

Figure 20. — Effect of wake distortions on rotor performance with rigid blades and steady aerodynamics.
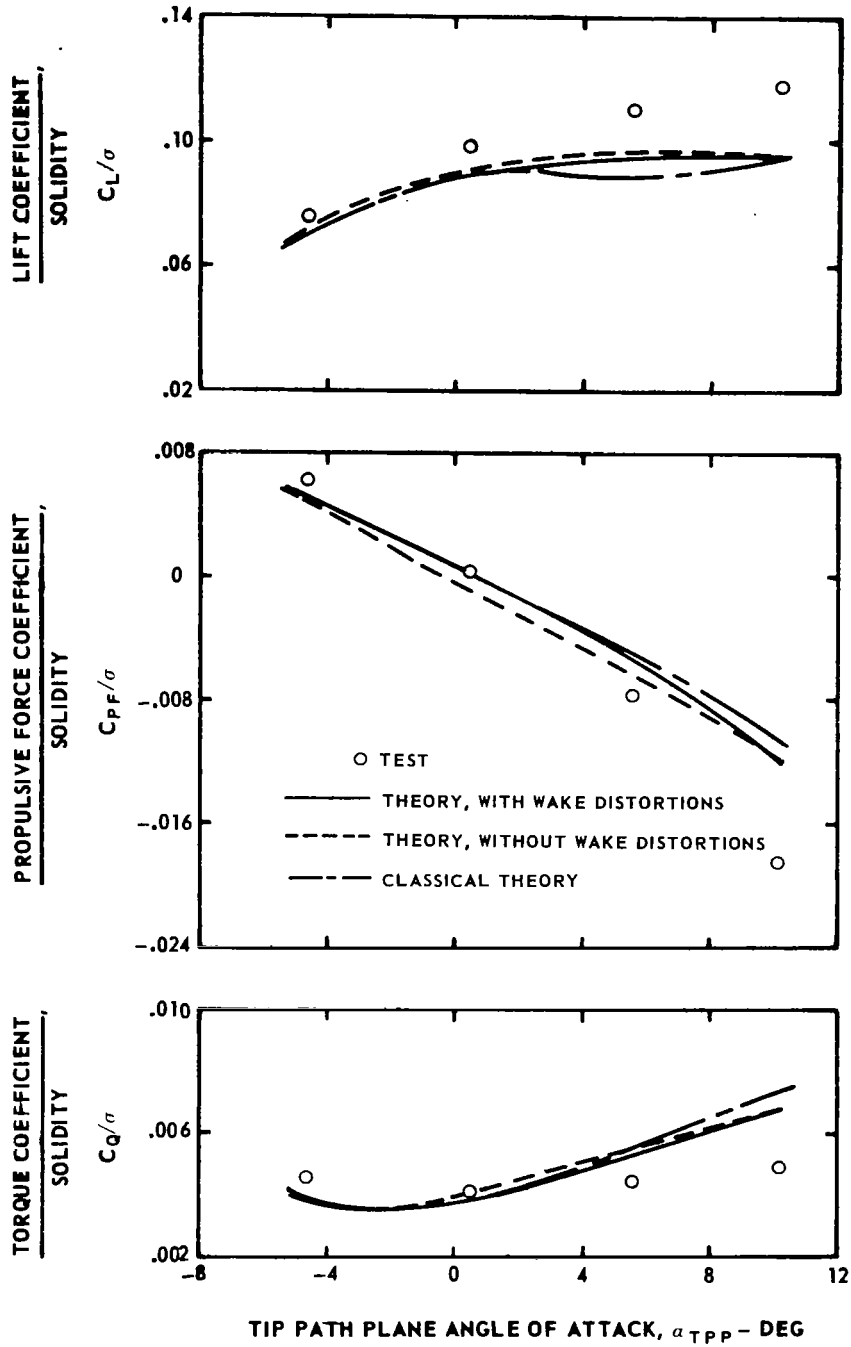
(b) Twist = 0 deg, advance ratio = 0.3

Figure 20. – Continued.
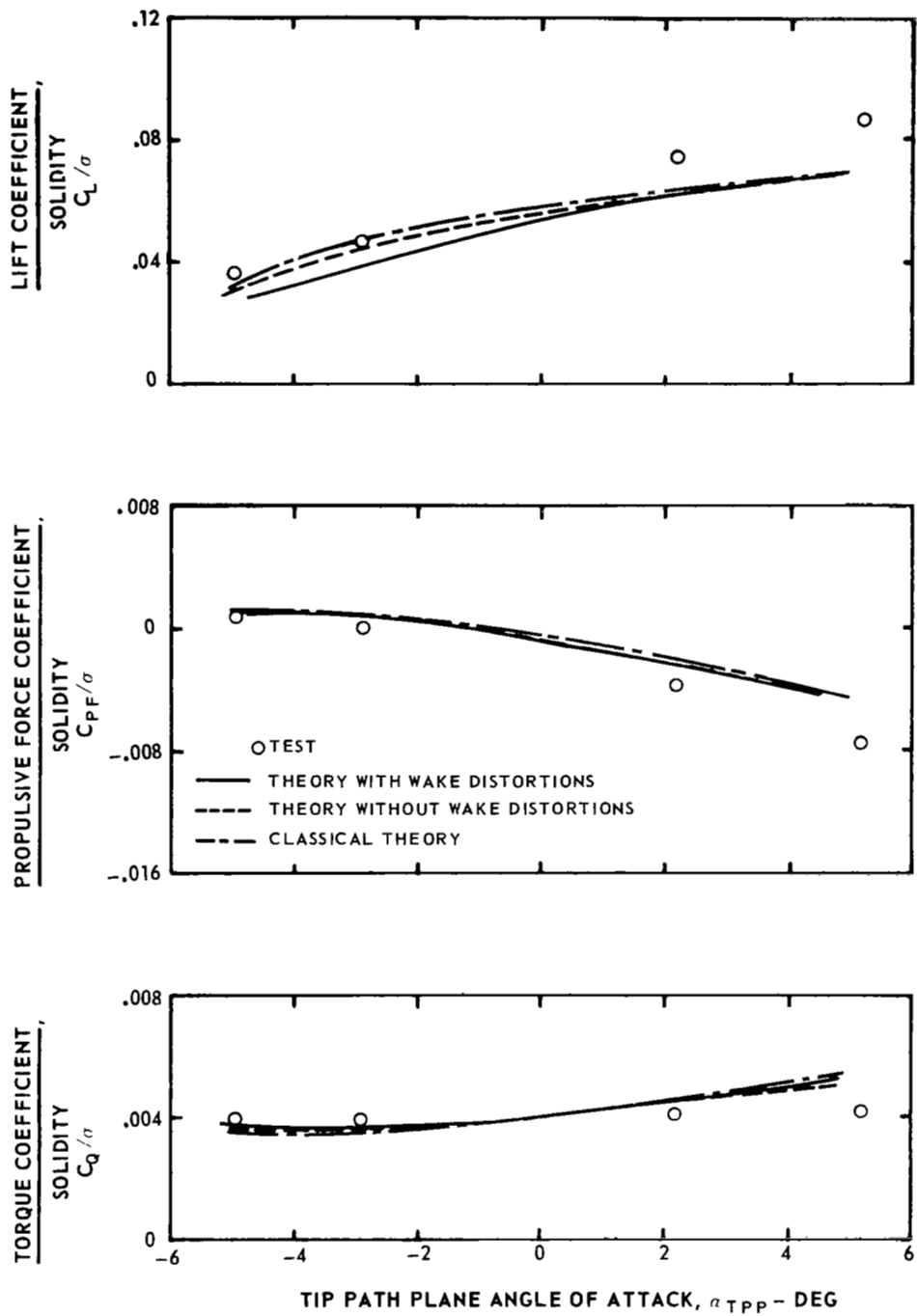
(c) Twist = 0 deg, advance ratio = 0.5

Figure 20. — Concluded.
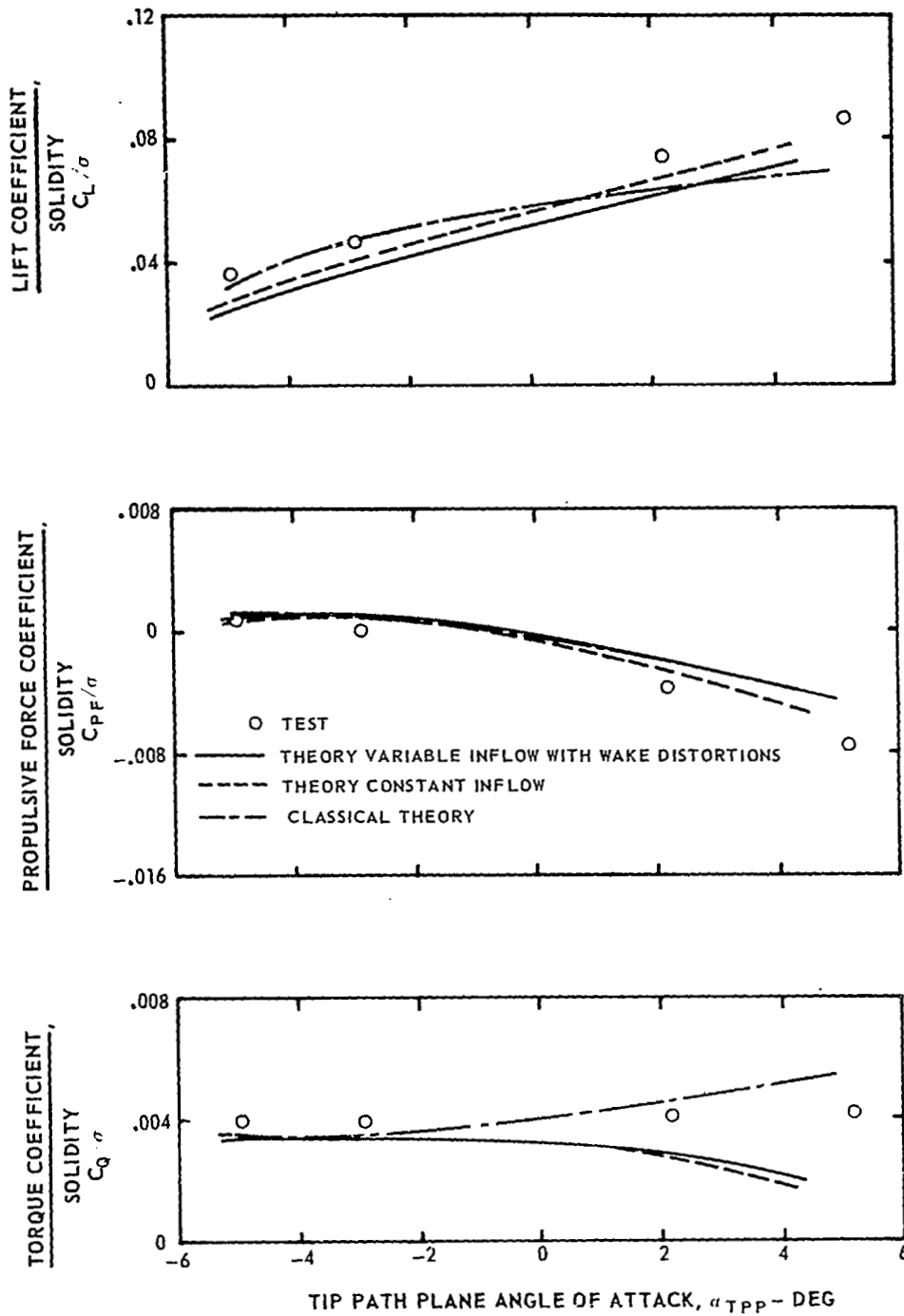
(a) Twist = −8 deg, advance ratio = 0.3

Figure 21. — Effect of wake distortions on rotor performance with flexible blades and unsteady aerodynamics.

79
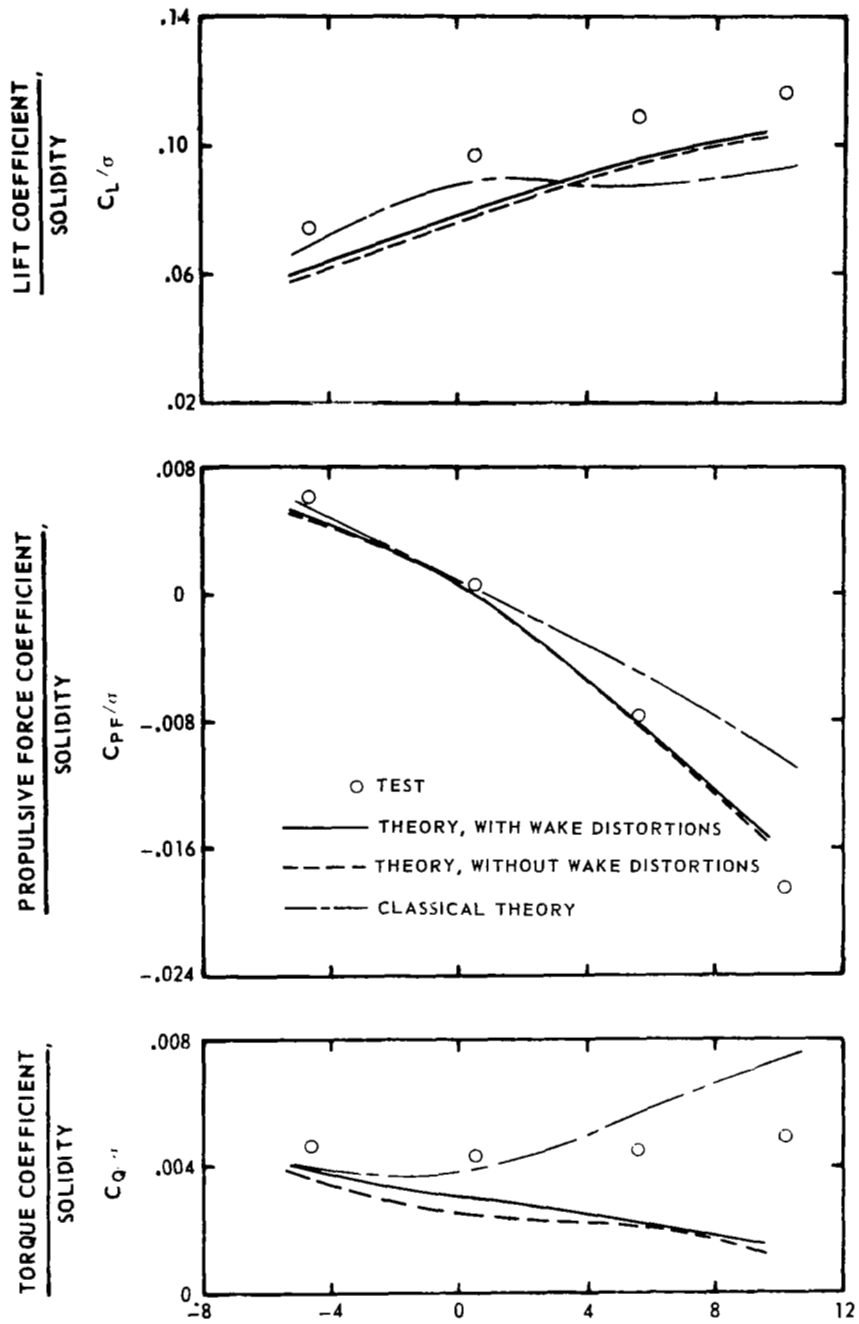
(b) Twist = 0 deg, advance ratio = 0.3

Figure 21.— Continued.

(c) Twist = 0 deg, advance ratio = 0.5

Figure 21. — Concluded.
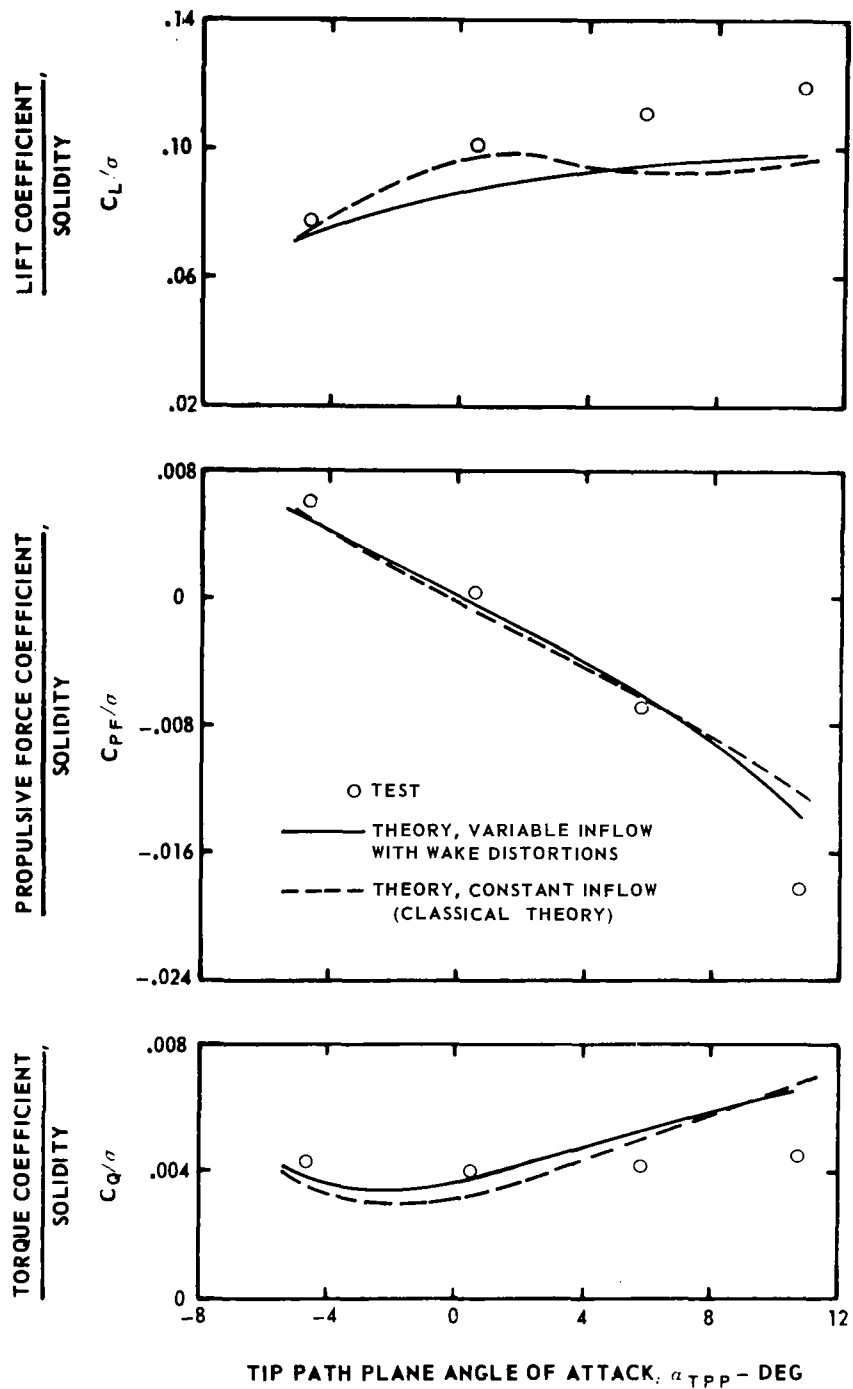
(a) Twist = -8 deg, advance ratio = 0.3

Figure 22. — Effect of variable inflow with wake distortions on rotor performance with rigid blades and steady aerodynamics.

(b) Twist = 0 deg, advance ratio = 0.3

Figure 22. — Continued.

(c) Twist = 0 deg, advance ratio = 0.5

Figure 22. – Concluded.

(a) Twist = −8 deg, advance ratio = 0.3

Figure 23. — Effect of variable inflow with wake distortions on rotor performance with flexible blades and steady aerodynamics.

85

LIFT COEFFICIENT / SOLIDITY

C_L / σ

PROPULSIVE FORCE COEFFICIENT / SOLIDITY

C_{PF} / σ

O TEST

——— THEORY, VARIABLE INFLOW WITH WAKE DISTORTIONS

– – – THEORY, CONSTANT INFLOW

–·–·– CLASSICAL THEORY

TORQUE COEFFICIENT / SOLIDITY

C_Q / σ

TIP PATH PLANE ANGLE OF ATTACK, α_{TPP} – DEG

(b) Twist = 0 deg, advance ratio = 0.3

Figure 23. – Continued.

86
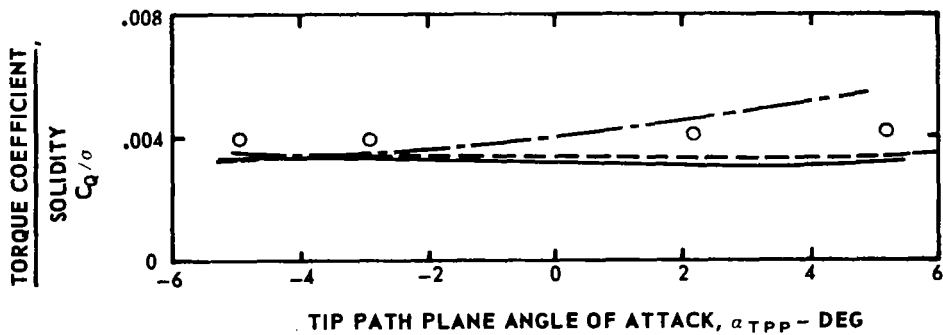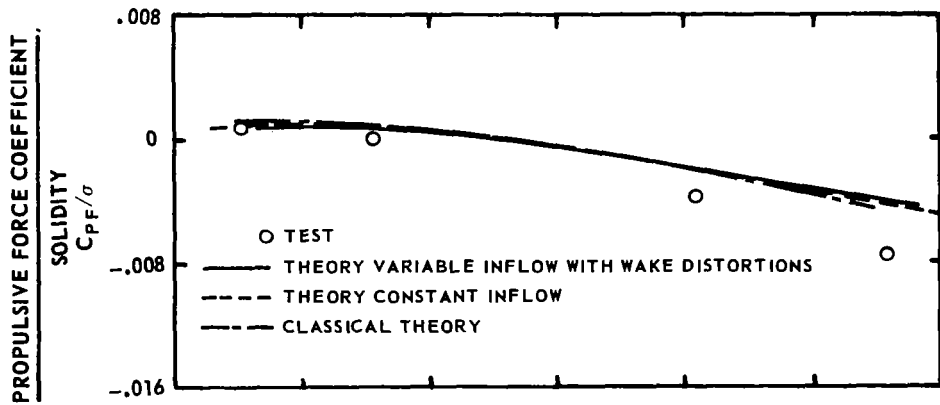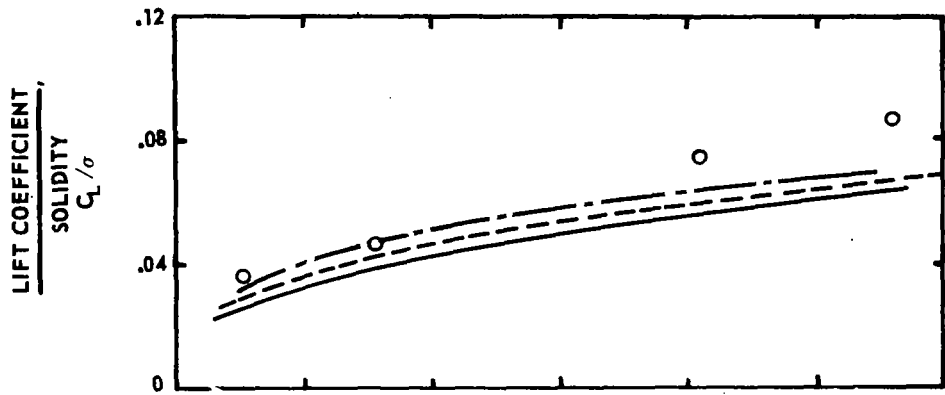
(c) Twist = 0 deg, advance ratio = 0.5

Figure 23. – Concluded.

(a) Twist = −8 deg, advance ratio = 0.3

Figure 24. — Effect of variable inflow with wake distortions on rotor performance with rigid blades and unsteady aerodynamics.

TIP PATH PLANE ANGLE OF ATTACK, α_{TPP} – DEG

(b) Twist = 0 deg, advance ratio = 0.3

Figure 24. – Continued.

89

(c) Twist = 0 deg, advance ratio = 0.5

Figure 24. — Concluded.

(a) Twist = −8 deg, advance ratio = 0.3

Figure 25. — Effect of variable inflow with wake distortions on rotor performance with flexible blades and unsteady aerodynamics.

91

TIP PATH PLANE ANGLE OF ATTACK, a_{TPP} – DEG

(b) Twist = 0 deg, advance ratio = 0.3

Figure 25. – Continued.

92

(c) Twist = 0 deg, advance ratio = 0.5

Figure 25. — Concluded.
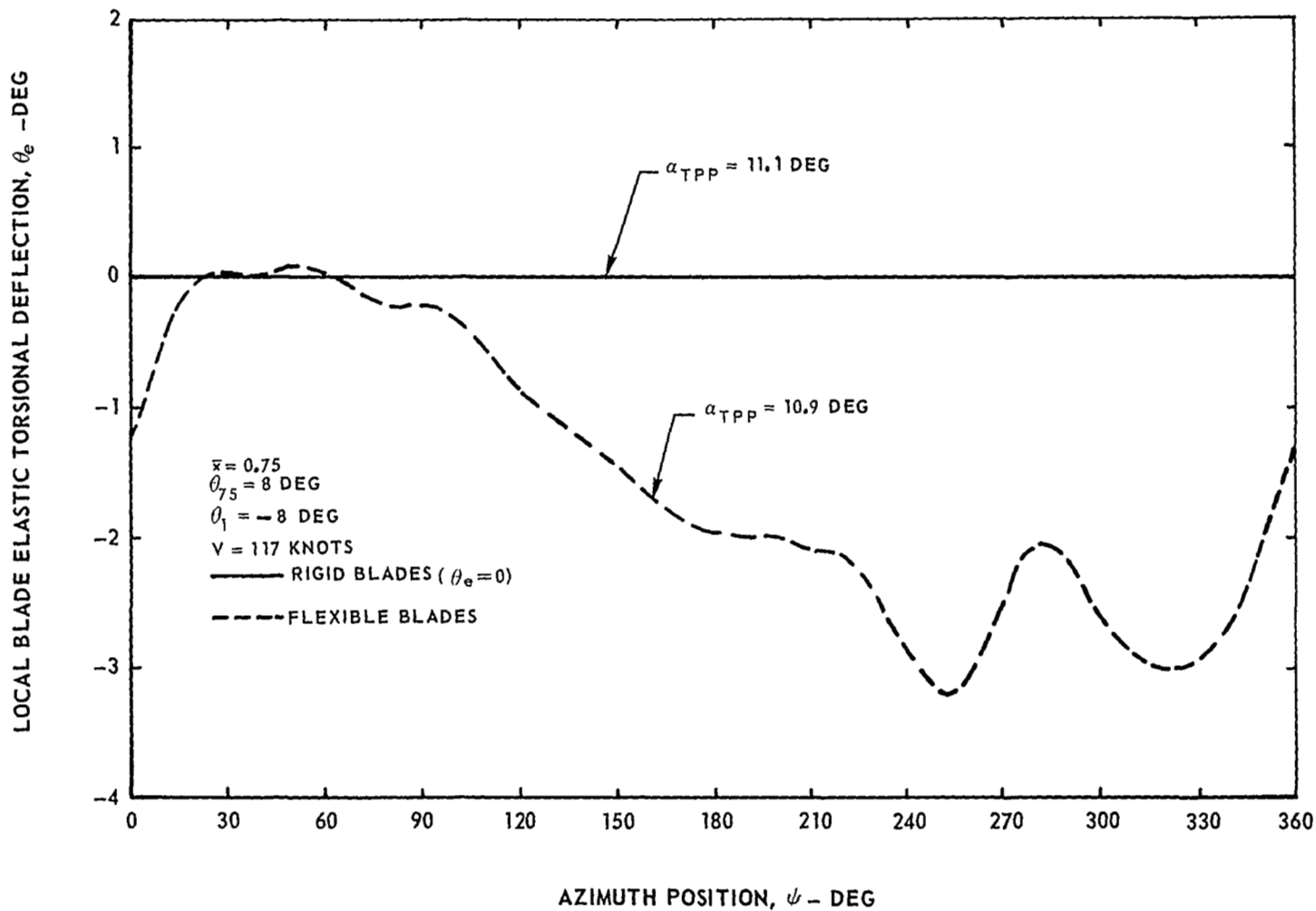
Figure 26.—Effect of blade flexibility on the blade elastic torsional deflection with steady aerodynamics and constant inflow at 0.3 advance ratio and α_S = 10.7 deg.
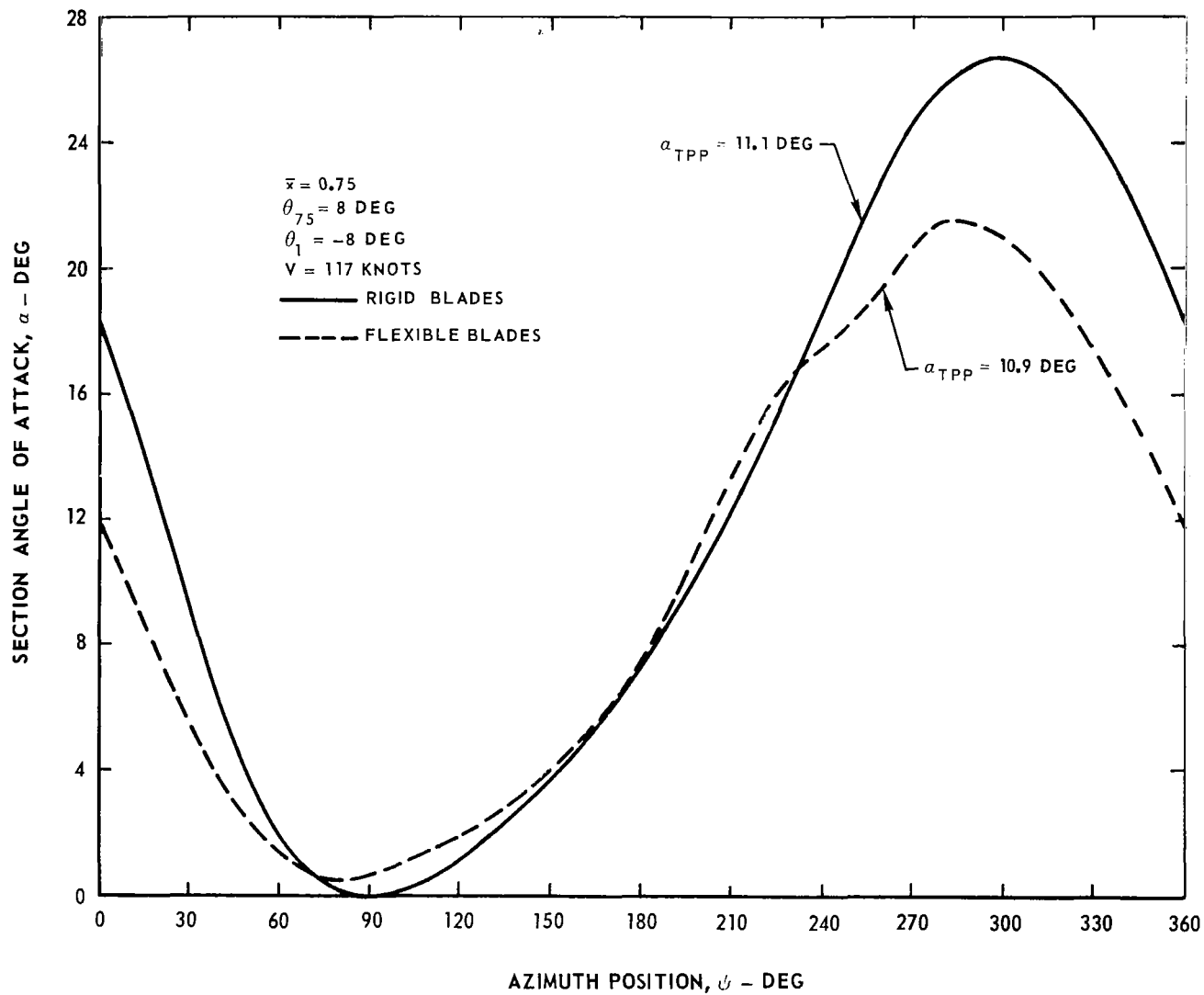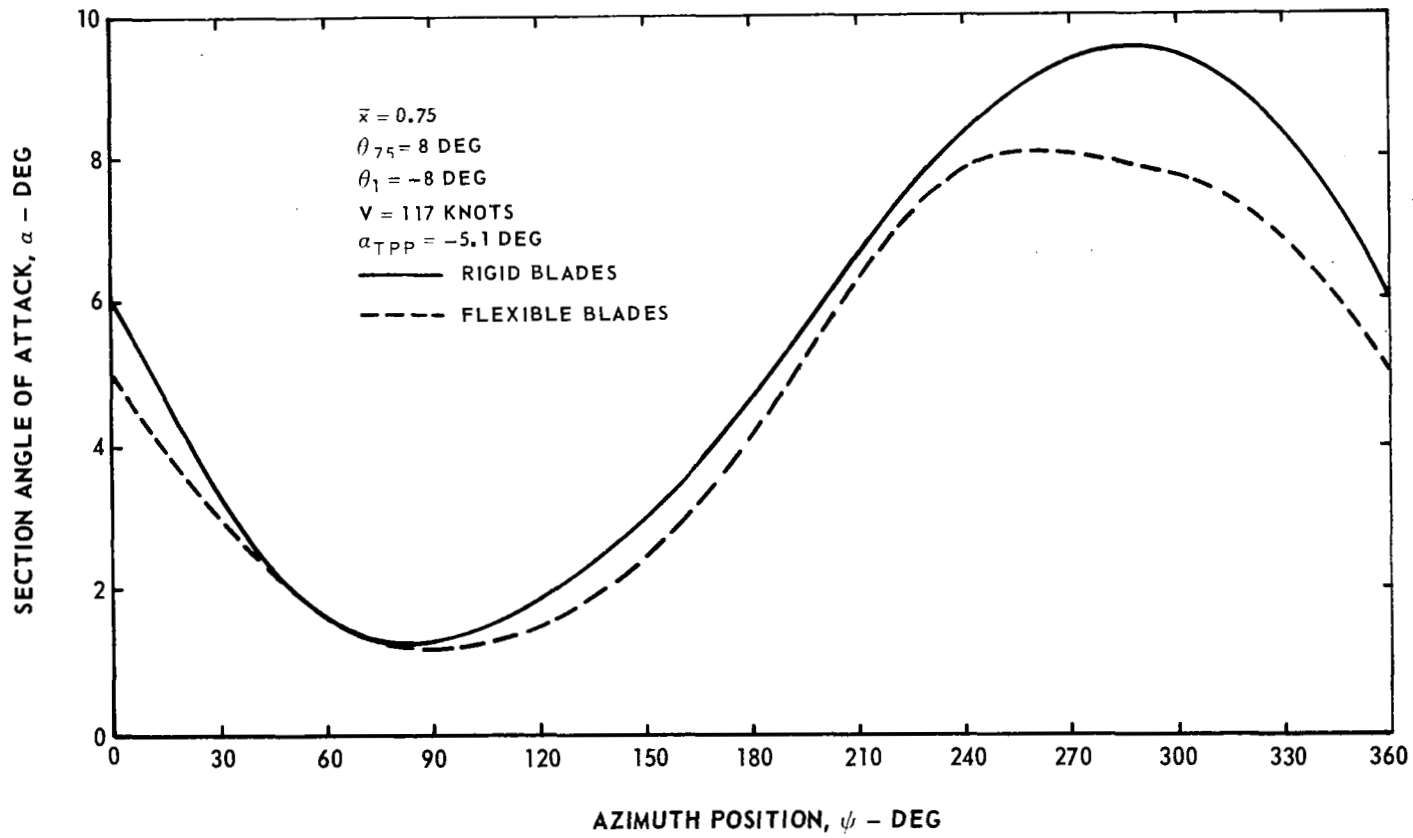
Figure 27.—Effect of blade flexibility on the section angle of attack with steady aerodynamics and constant inflow at 0.3 advance ratio and $\alpha_S = 10.7$ deg.
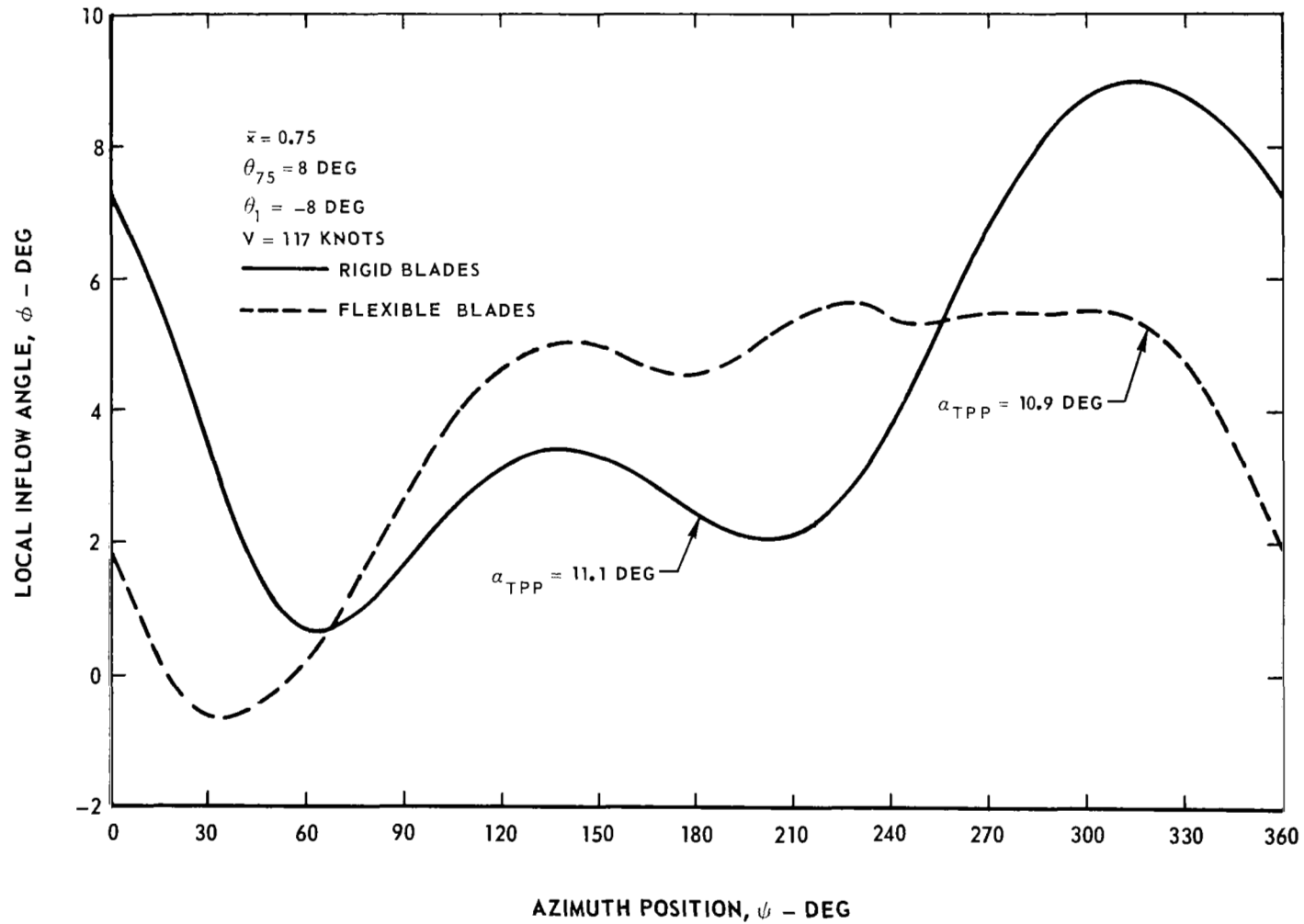
Figure 28.–Effect of flexibility on the local inflow angle with steady aerodynamics and constant inflow at 0.3 advance ratio and $\alpha_S = 10.7$ deg.
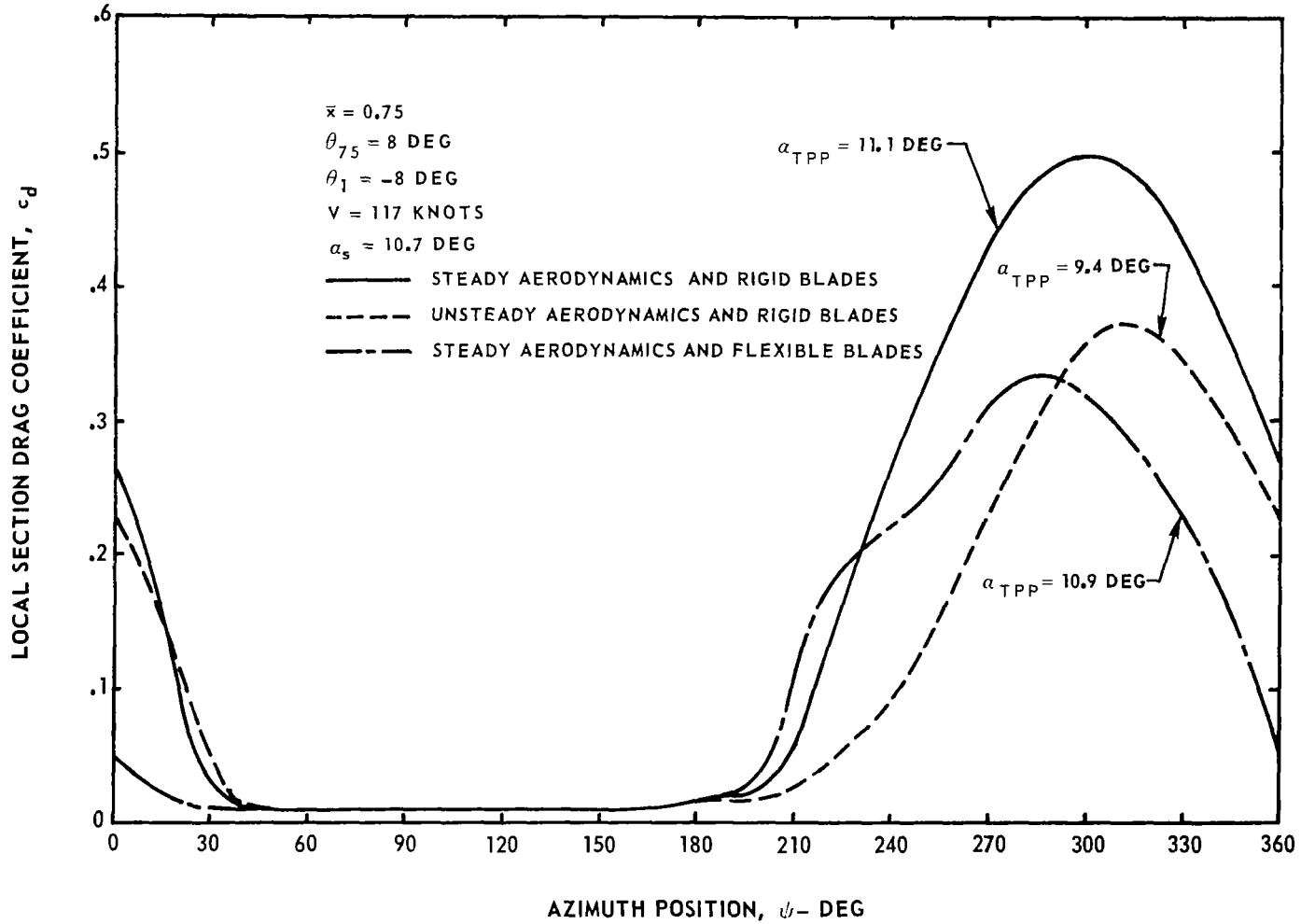
Figure 29.—Effect of blade flexibility and unsteady aerodynamics on blade section drag coefficient with constant inflow at 0.3 advance ratio.

The chart axes and legend read:

Y-axis: LOCAL SECTION DRAG COEFFICIENT, c_d

X-axis: AZIMUTH POSITION, ψ– DEG

Parameters:
$\bar{x} = 0.75$
$\theta_{75} = 8$ DEG
$\theta_1 = -8$ DEG
$V = 117$ KNOTS
$\alpha_s = 10.7$ DEG

Legend:
——— STEADY AERODYNAMICS AND RIGID BLADES
– – – UNSTEADY AERODYNAMICS AND RIGID BLADES
–·–·– STEADY AERODYNAMICS AND FLEXIBLE BLADES

$\alpha_{TPP} = 11.1$ DEG
$\alpha_{TPP} = 9.4$ DEG
$\alpha_{TPP} = 10.9$ DEG
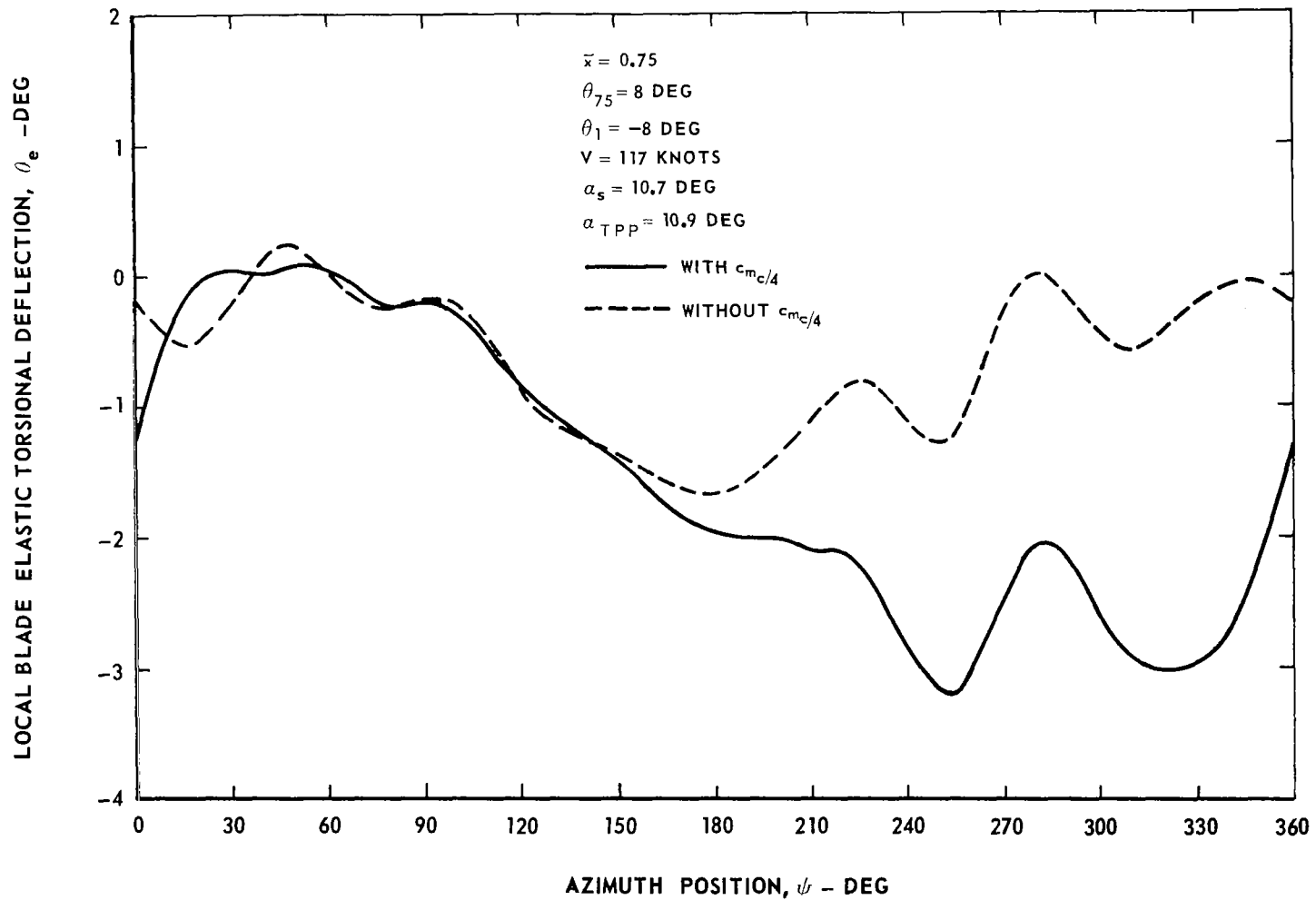
Figure 30. —Effect of aerodynamic pitching moment on the blade elastic torsional deflection with steady aerodynamics and constant inflow at 0.3 advance ratio.

LOCAL BLADE ELASTIC TORSIONAL DEFLECTION, θ_e – DEG

AZIMUTH POSITION, ψ – DEG

$\bar{x} = 0.75$
$\theta_{75} = 8$ DEG
$\theta_1 = -8$ DEG
V = 117 KNOTS
$\alpha_{TPP} = -5.1$ DEG
——— RIGID BLADES ($\theta_e = 0$)
– – – – FLEXIBLE BLADES
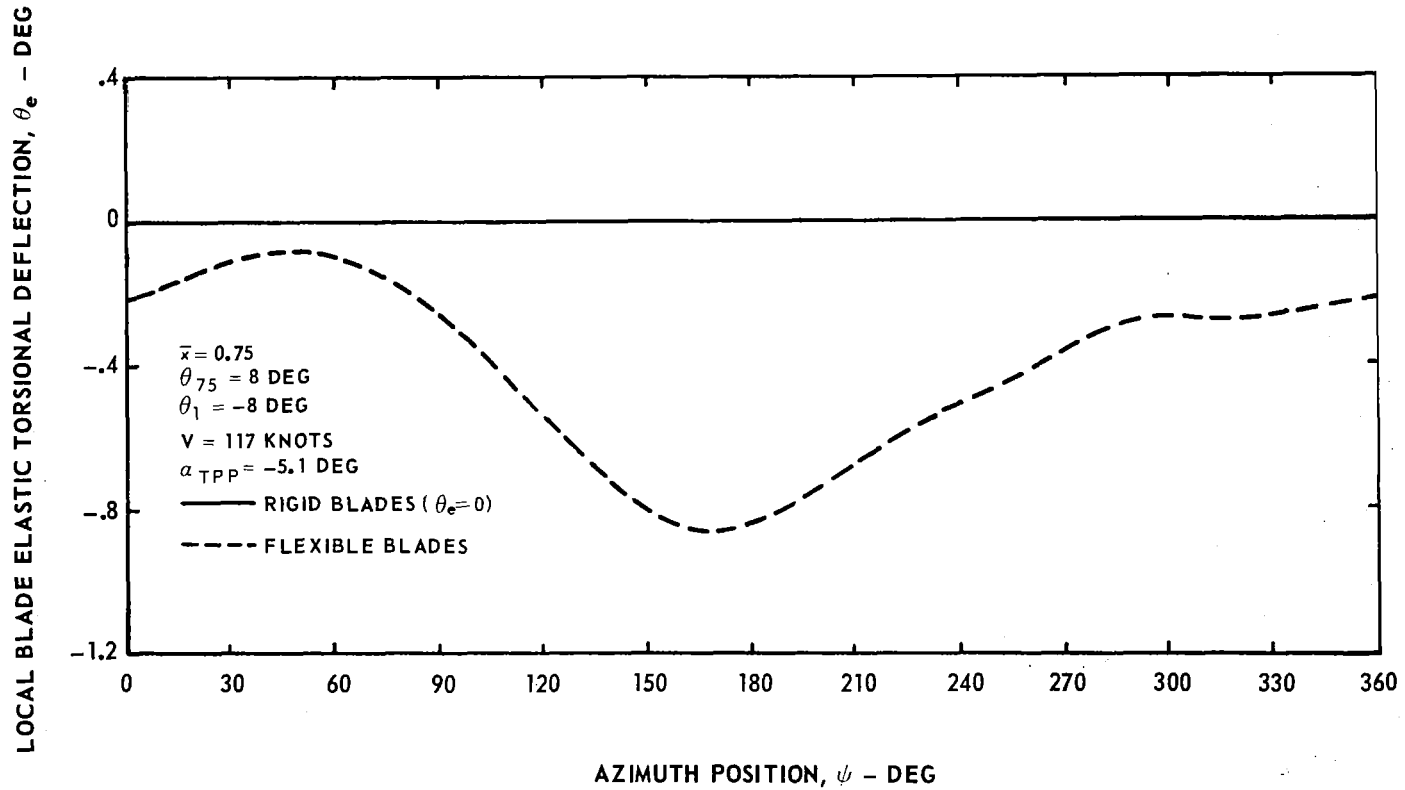
Figure 31. – Effect of blade flexibility on the blade elastic torsional deflection with steady aerodynamics, constant inflow and 0.3 advance ratio and $\alpha_S = -4.6$ deg.

Figure 32. — Effect of blade flexibility on the blade section angle of attack with steady aerodynamics, constant inflow and 0.3 advance ratio and $\alpha_S = -4.6$ deg.

CHORDWISE LOCATION OF BLADE CENTER OF GRAVITY
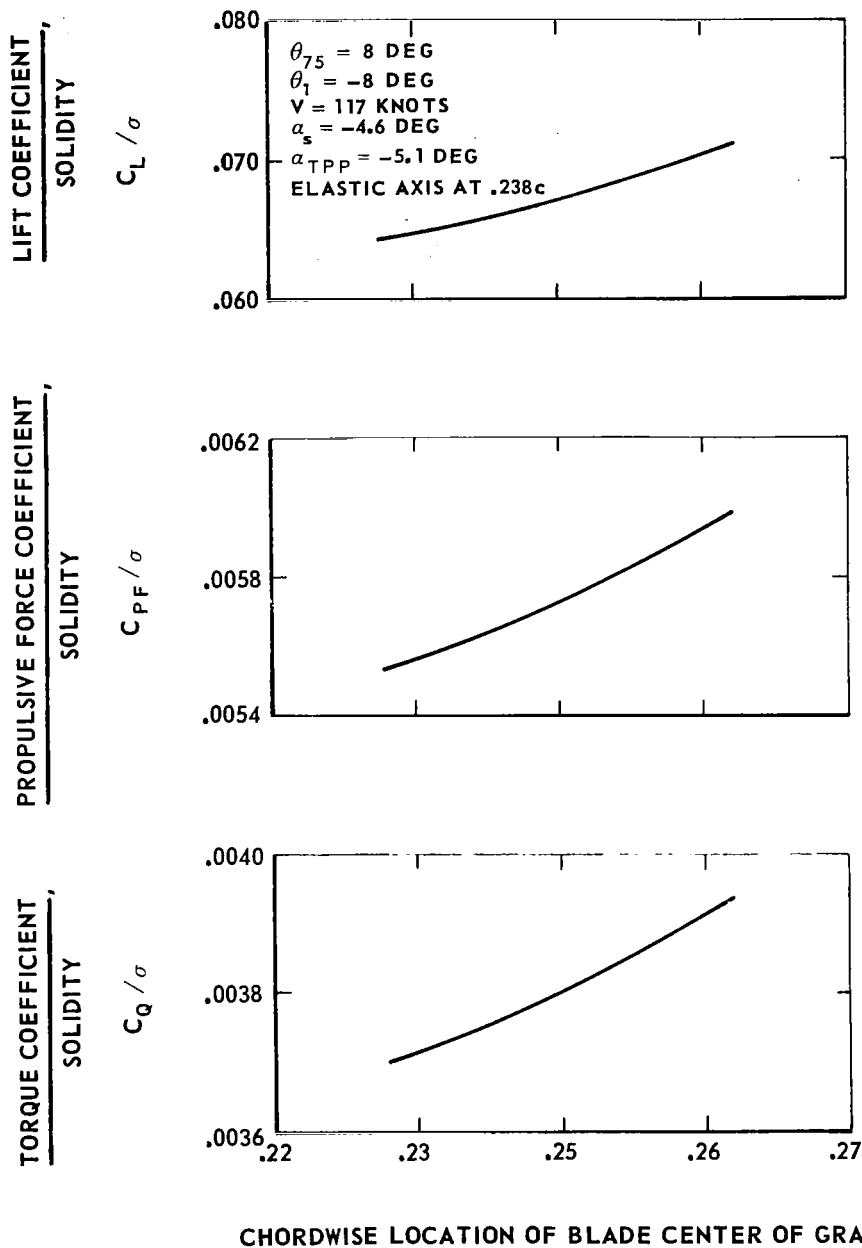
Figure 33.– Sensitivity of rotor lift propulsive force and torque to blade center of gravity location with steady aerodynamics and constant inflow.
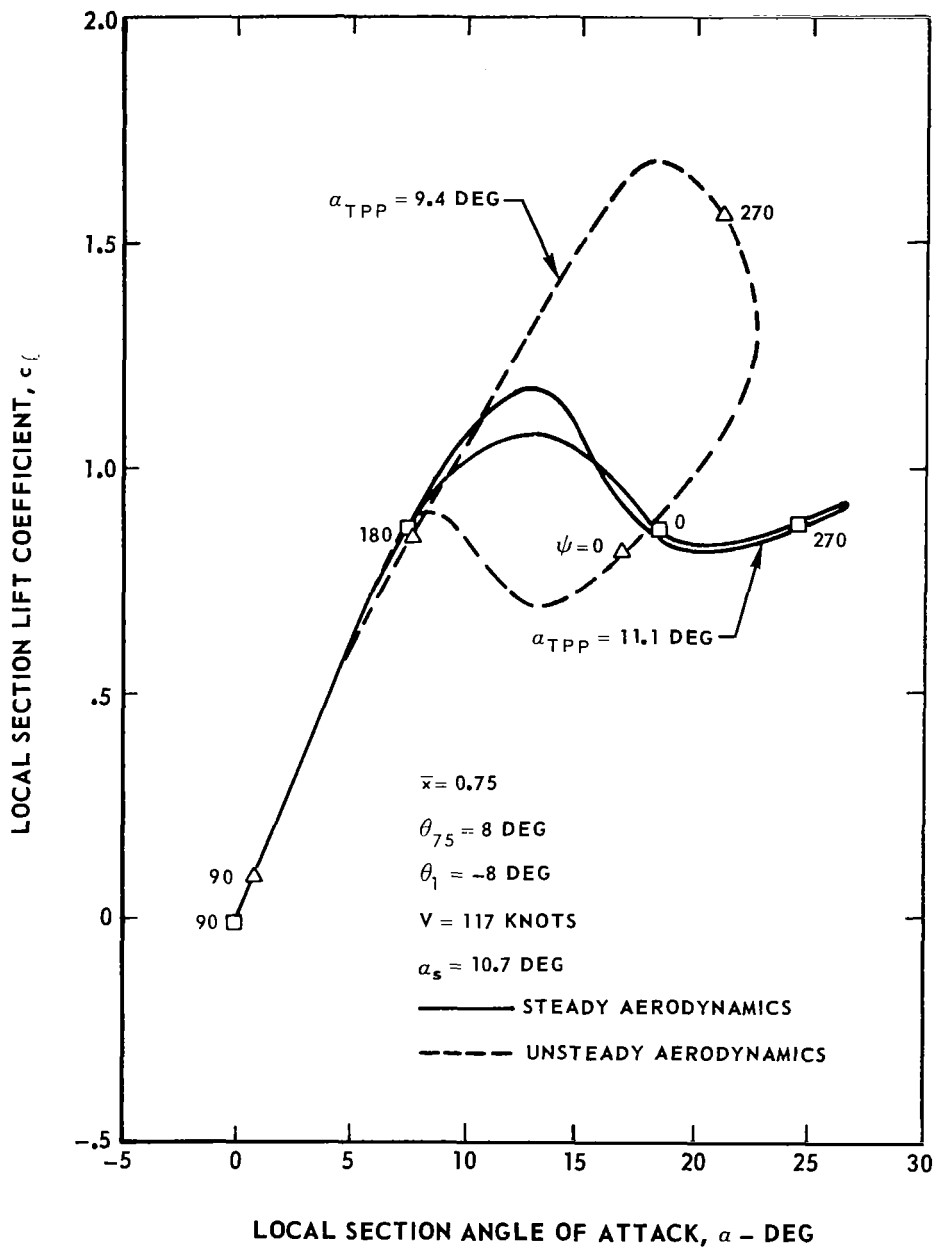
Figure 34.—Effect of unsteady aerodynamics on the blade section lift and angle of attack with rigid blades and constant inflow at 0.3 advance ratio.
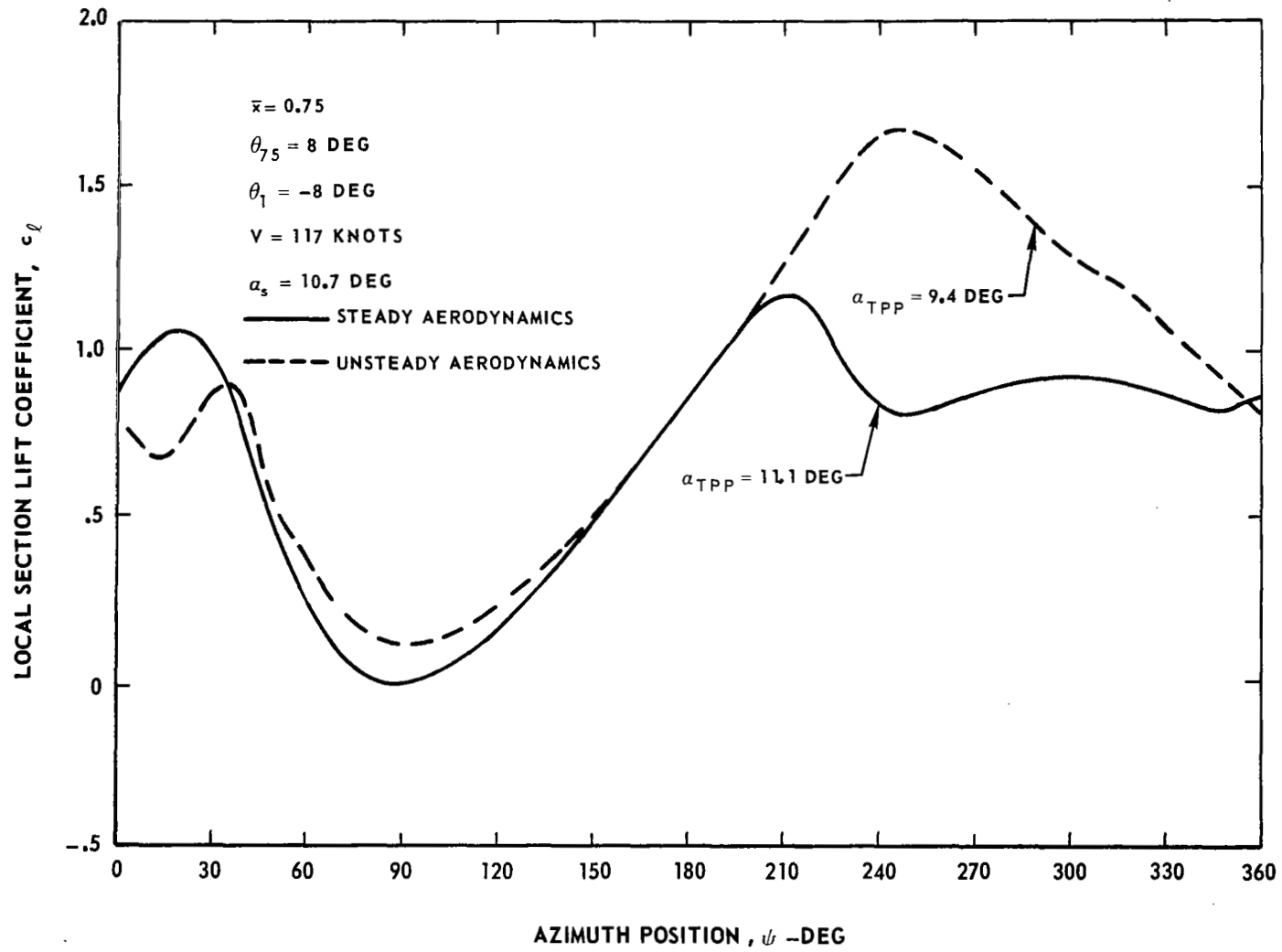
Figure 35.—Effect of unsteady aerodynamics on the blade section lift coefficient with rigid blades and constant inflow at 0.3 advance ratio.
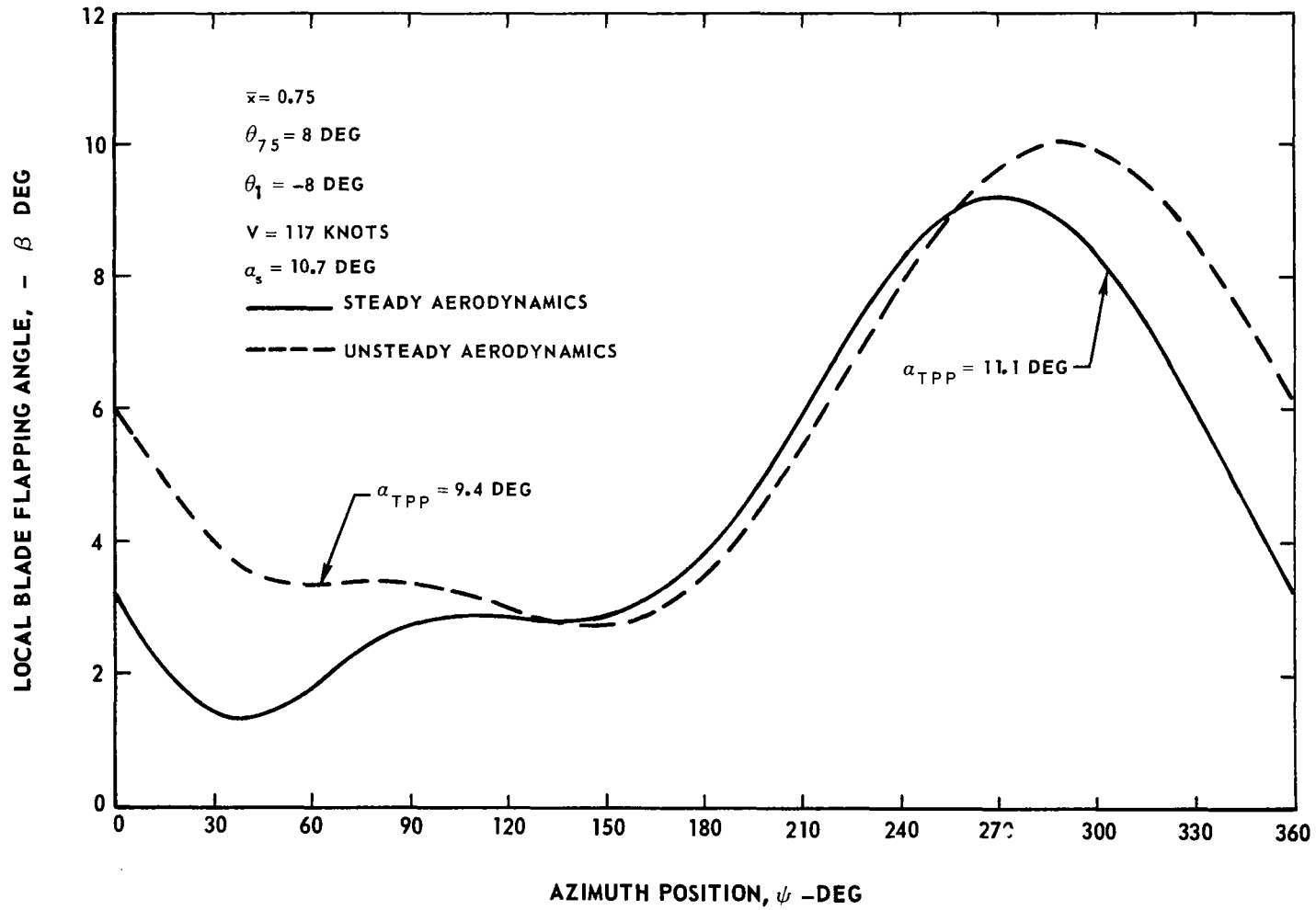
Figure 36.-Effect of unsteady aerodynamics on the blade flapping angle with rigid blades and constant inflow at 0.3 advance ratio.
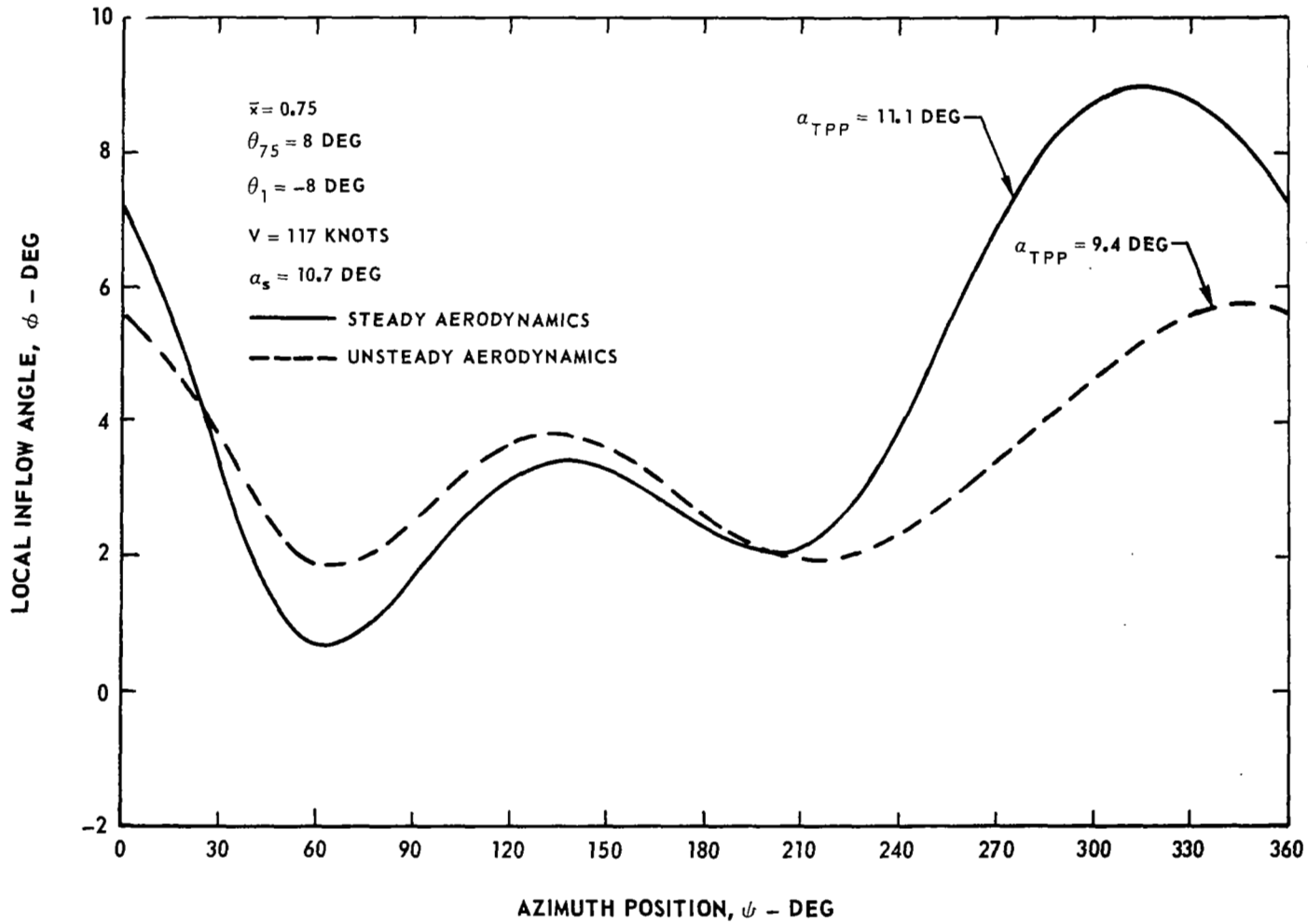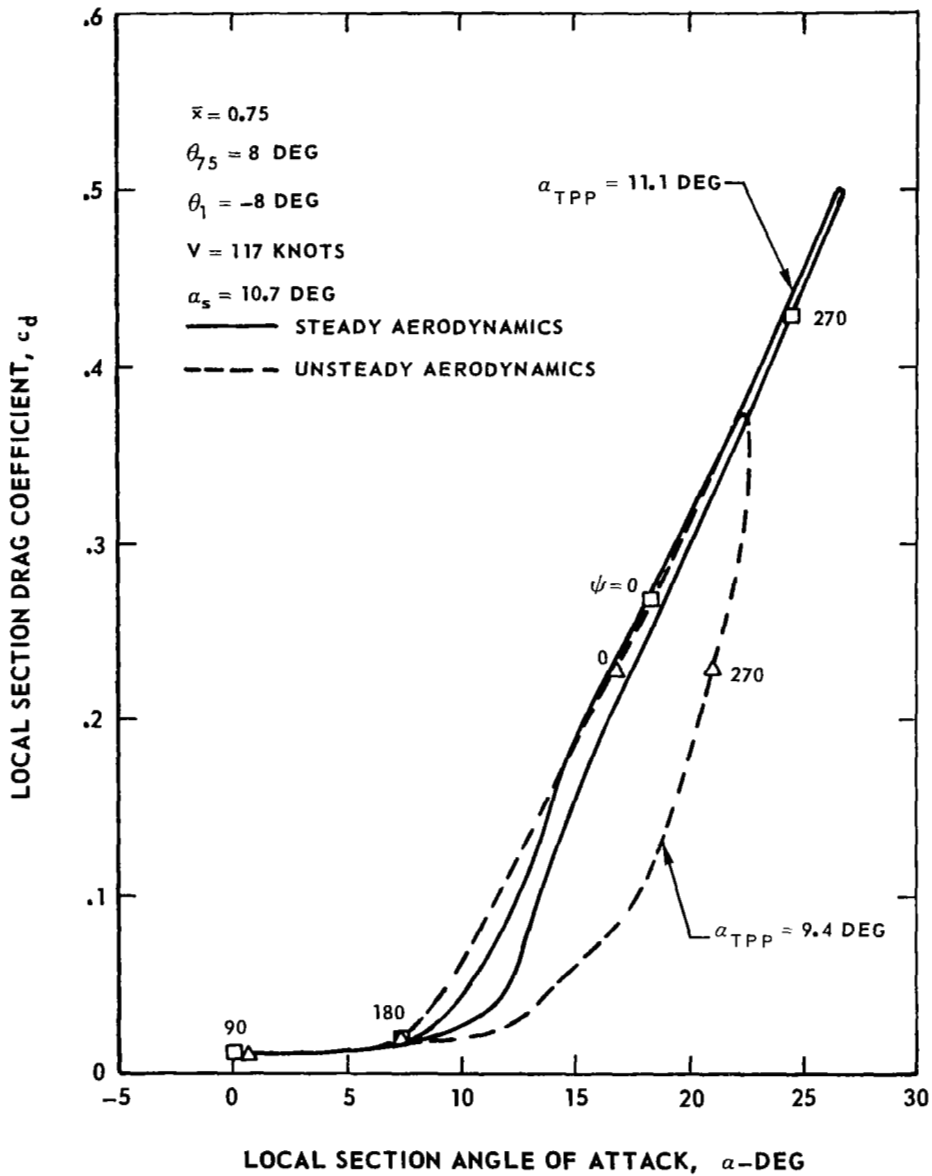
Figure 37.–Effect of unsteady aerodynamics on the local inflow angle with rigid blades and constant inflow at 0.3 advance ratio.
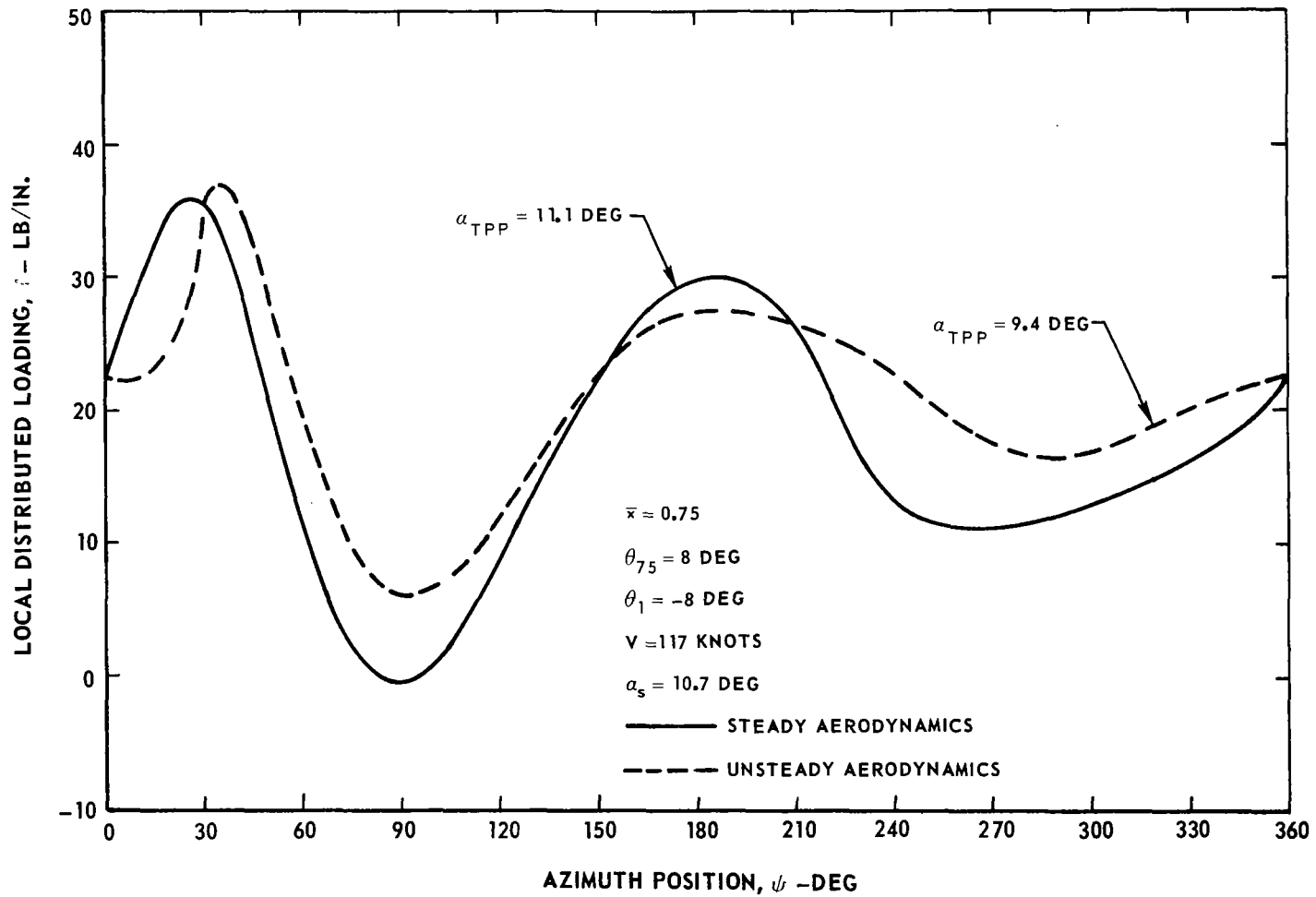
Figure 38.—Effect of unsteady aerodynamics on the blade loading distribution with rigid blades and constant inflow at 0.3 advance ratio.

Figure 39.–Effect of unsteady aerodynamics on the section drag coefficient with constant inflow and rigid blades at 0.3 advance ratio.
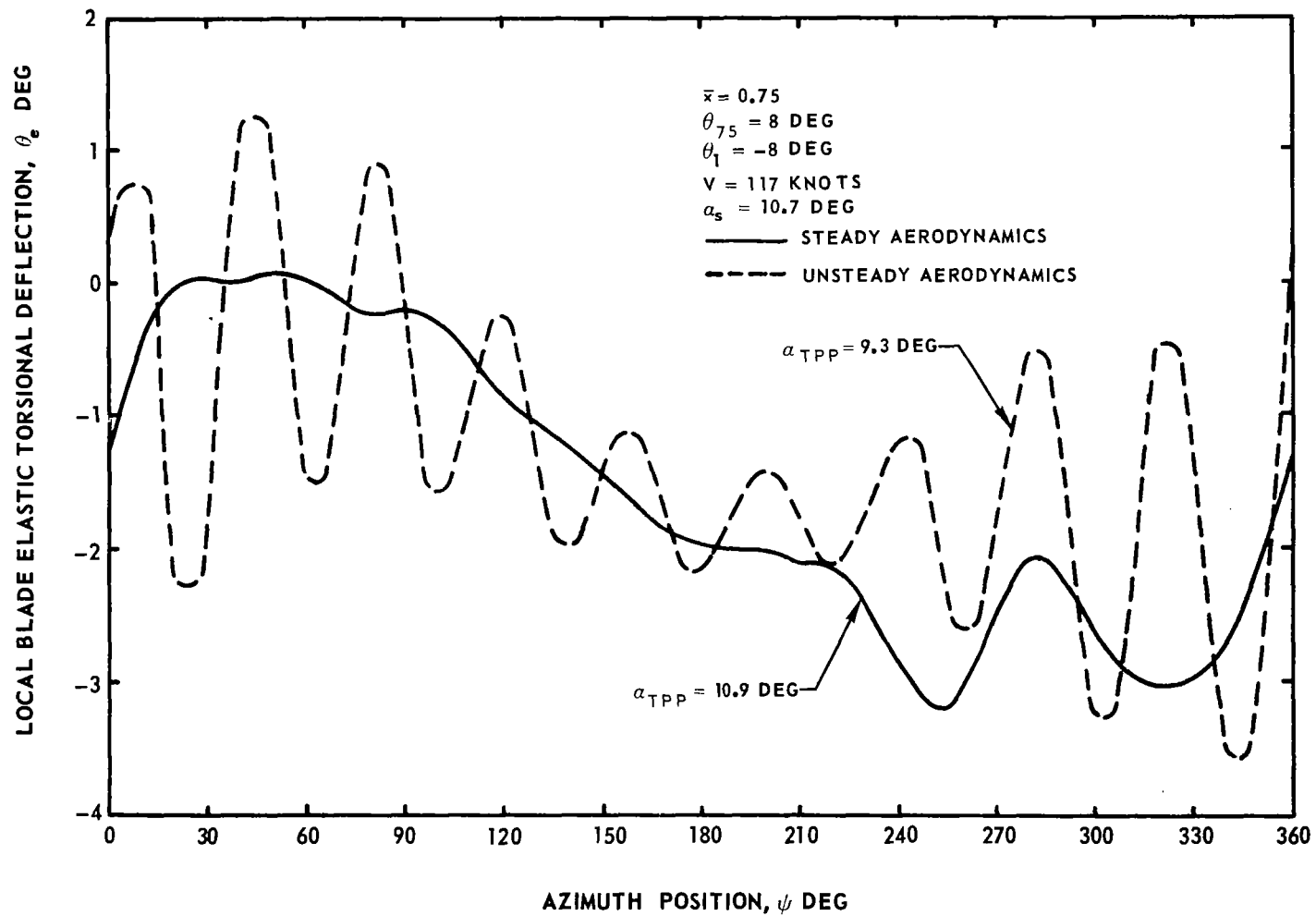
Figure 40.—Effect of unsteady aerodynamics on the blade elastic torsional deflection with constant inflow at 0.3 advance ratio.

POSITIVE UPFLOW NORMAL TO TIP PATH PLANE IN FT/SEC

$\theta_{75} = 8$ DEG
$\theta_1 = -8$ DEG
$V = 117$ KNOTS
$\alpha_{TPP} = -5.1$ DEG

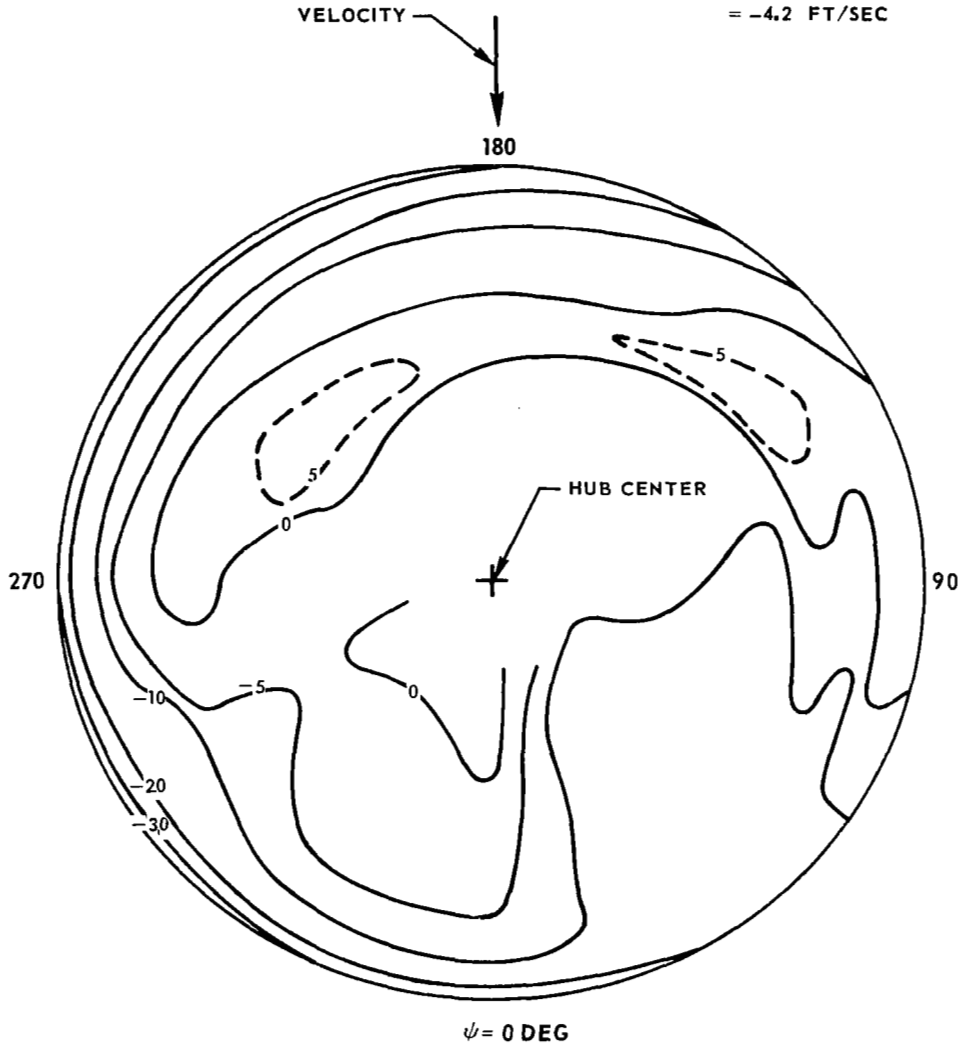NOTE: INDUCED VELOCITY FOR
CONSTANT INFLOW CONDITION
$= -4.2$ FT/SEC

VELOCITY

180

270

HUB CENTER

90

$\psi = 0$ DEG

Figure 41.—Induced velocity distribution based on distorted wake,
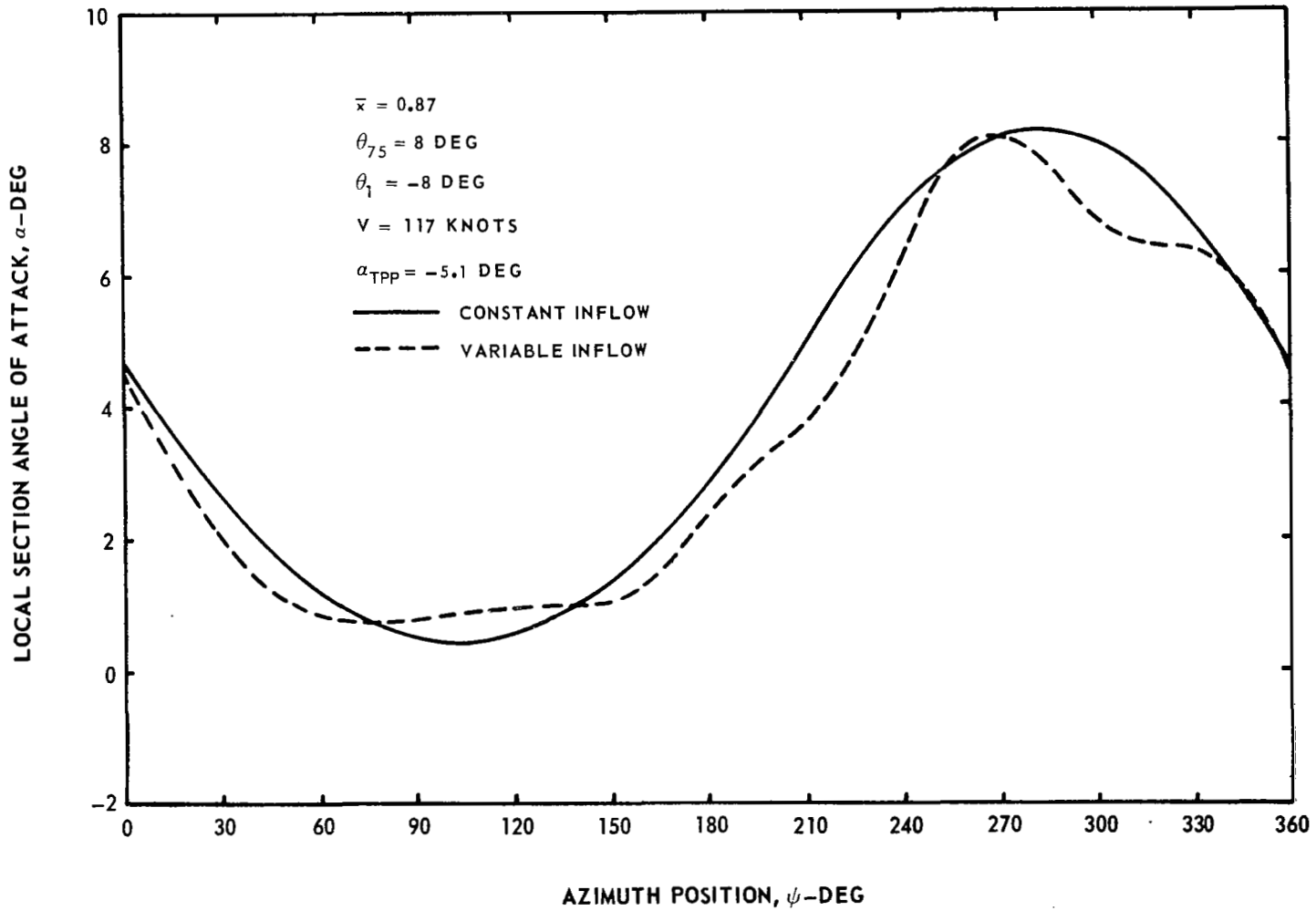blade flexibility and unsteady aerodynamics.

109

Figure 42.–Effect of variable inflow on the blade section angle of attack with wake distortions, flexible blades and steady aerodynamics.

VIEW PARALLEL TO THE TIP PATH PLANE

$\theta_{75} = 8$ DEG

$\theta_1 = -8$ DEG

V = 117 KNOTS

$\alpha_{TPP} = -5.1$ DEG

WAKE LATERAL COORDINATE/ROTOR RADIUS, y/R

CLASSICAL WAKE

ANALYTICAL DISTORTED WAKE

VELOCITY

HUB CENTER

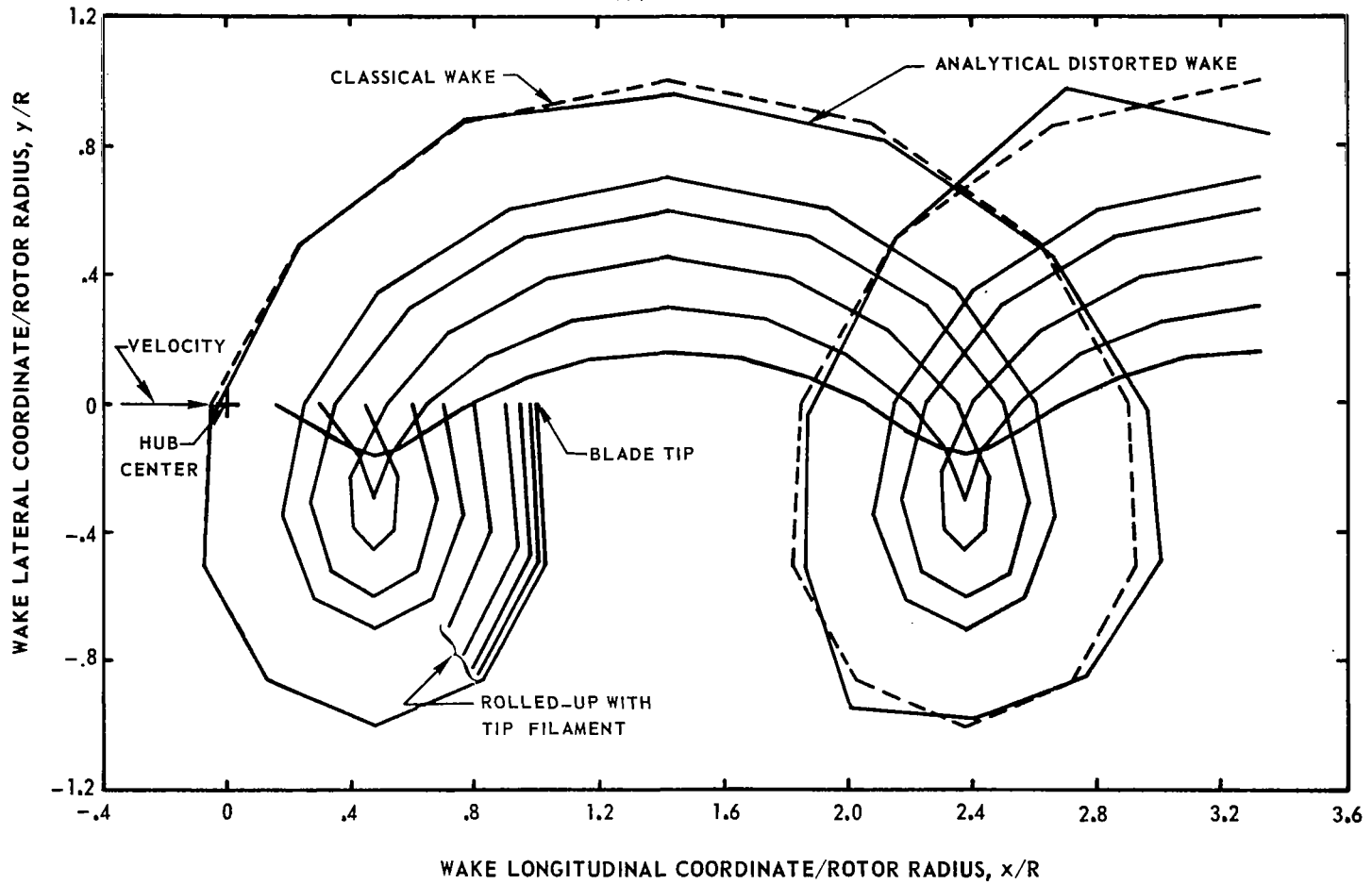BLADE TIP

ROLLED-UP WITH TIP FILAMENT

WAKE LONGITUDINAL COORDINATE/ROTOR RADIUS, x/R

Figure 43.—Top view of the trailing wake filaments of one blade.

$\theta_{75} = 8$ DEG
$\theta_1 = -8$ DEG
V = 117 KNOTS
$a_{TPP} = -5.1$ DEG

CLASSICAL WAKE

TIP PATH PLANE

BLADE TIP

HUB CENTER

ANALYTICAL DISTORTED WAKE

TIP PATH PLANE

BLADE TIP

HUB CENTER

WAKE AXIAL COORDINATE/ROTOR RADIUS, z/R
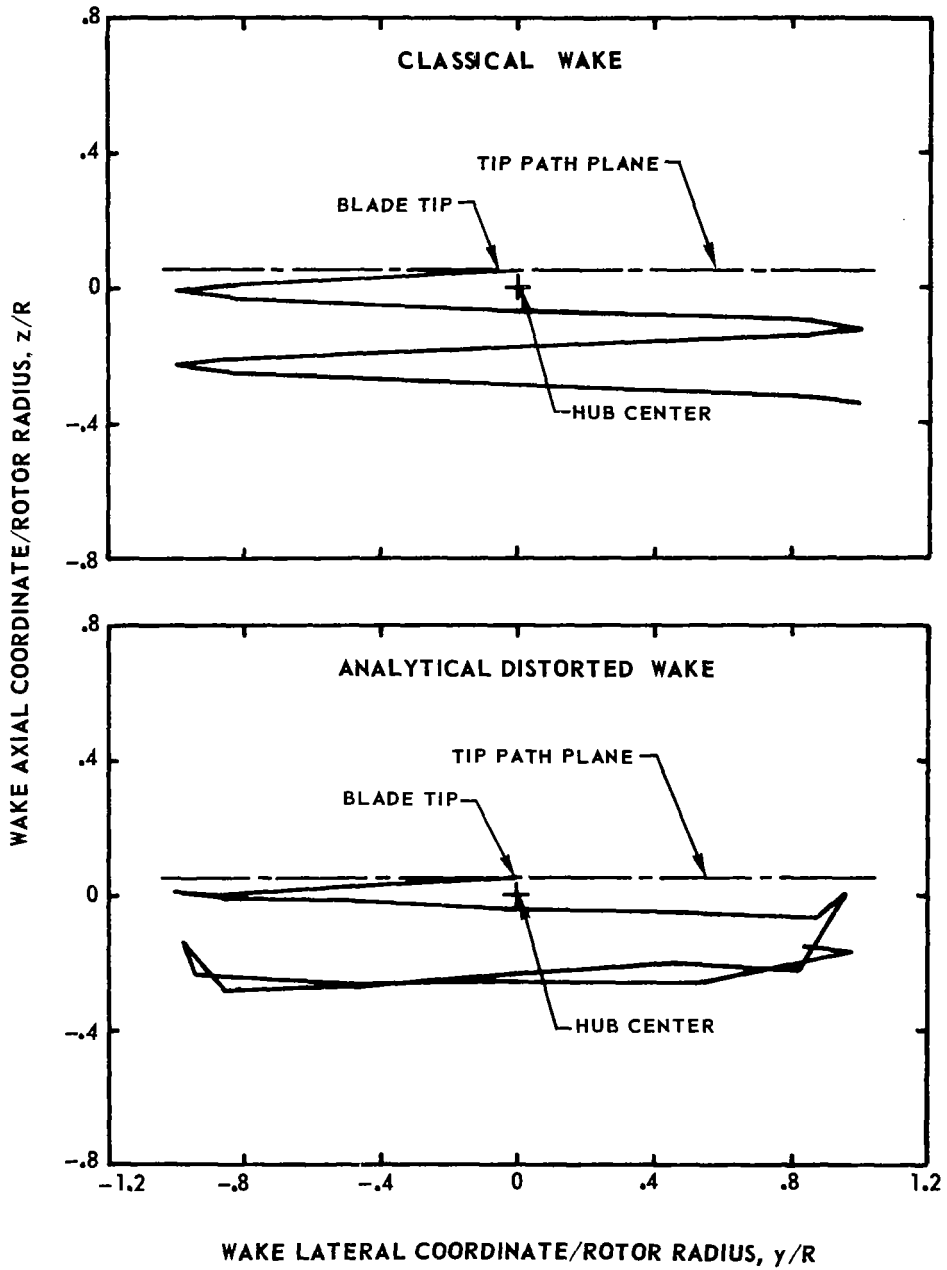
WAKE LATERAL COORDINATE/ROTOR RADIUS, y/R

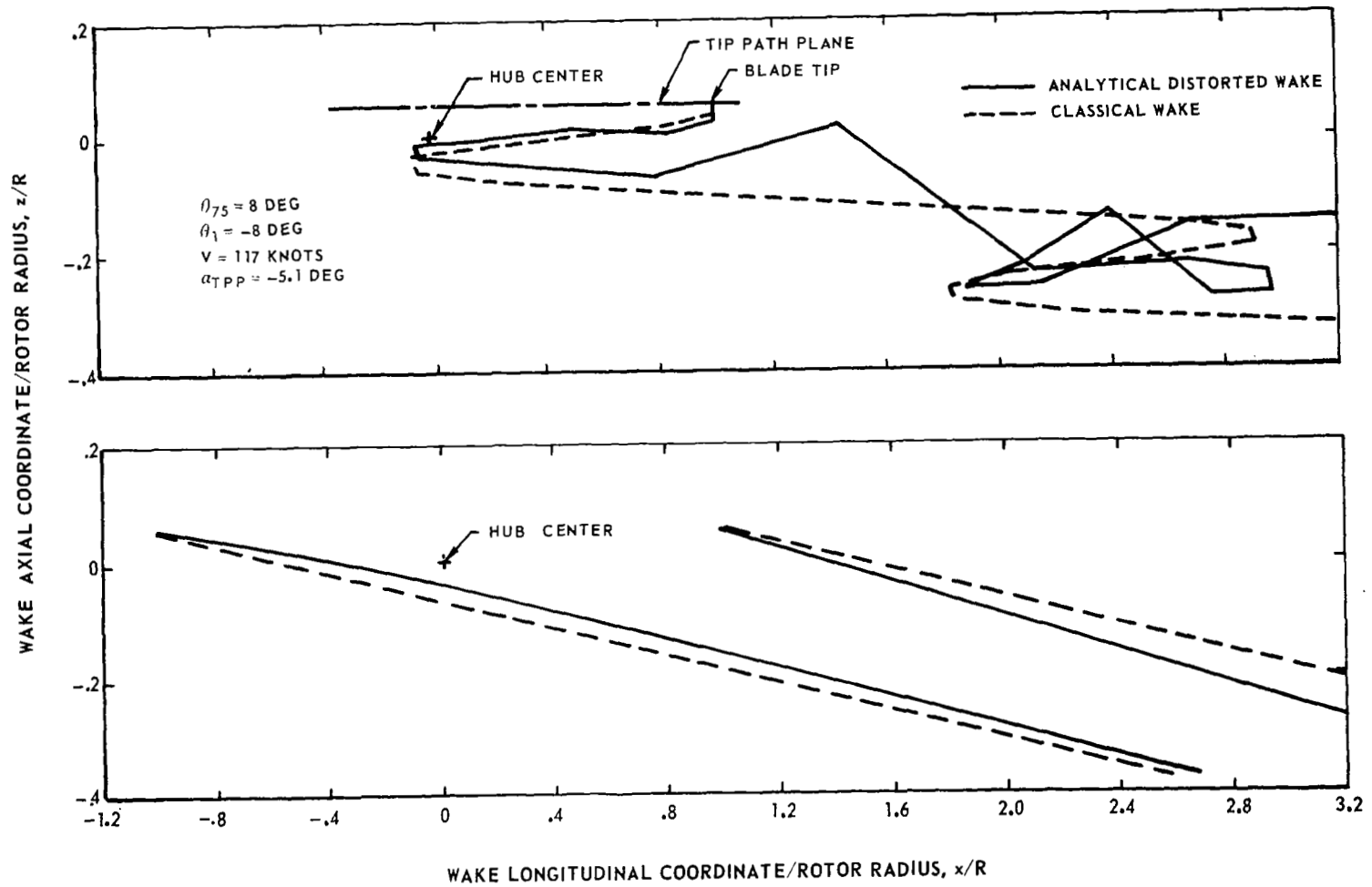Figure 44.→Rear view of the tip filament of one blade.

Figure 45.—Side view of the trailing wake filaments of one blade and comparison of wake boundaries in the longitudinal plane of symmetry.
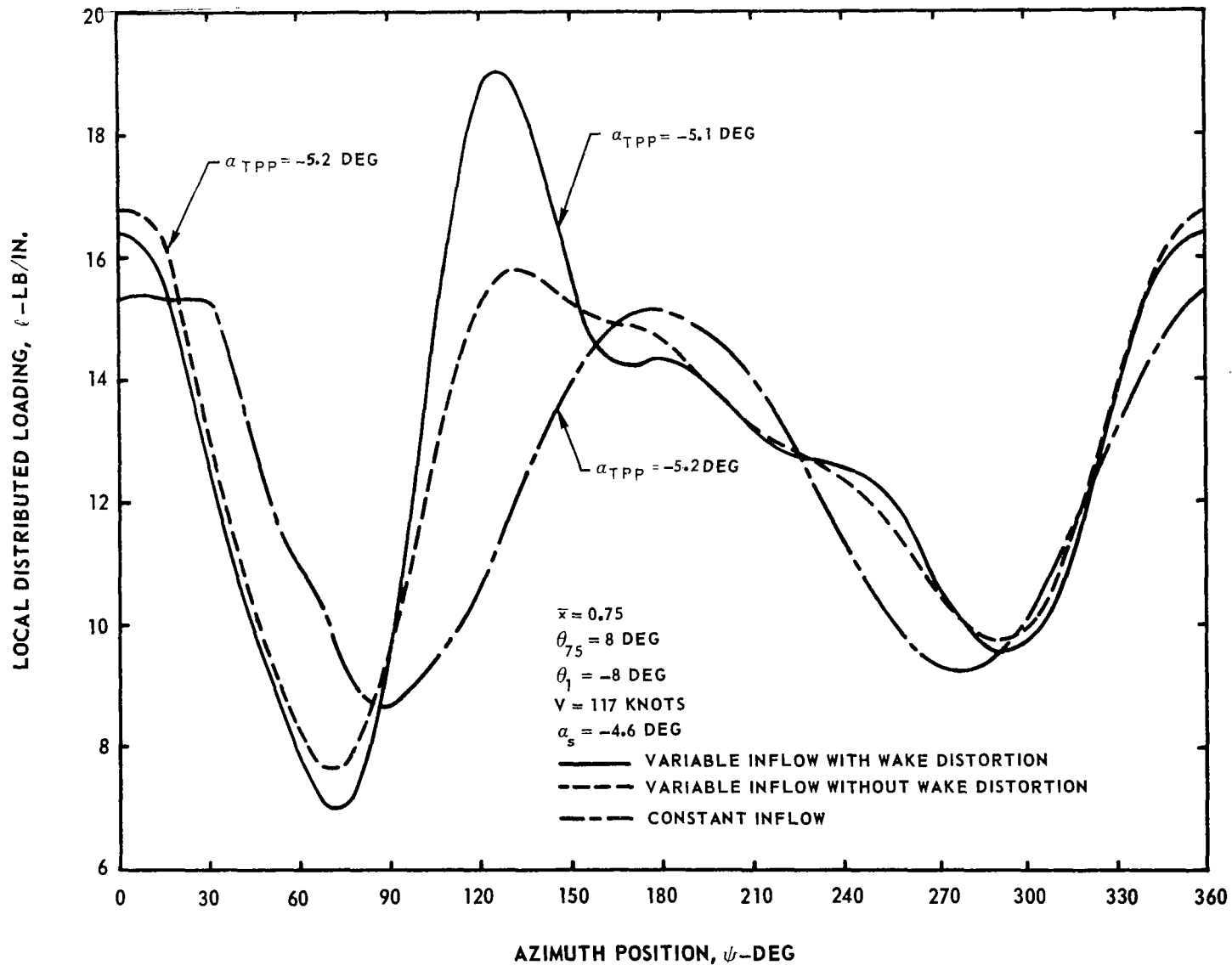
Figure 46.—Effect of variable inflow on the blade distributed loading with flexible blades and unsteady aerodynamics.